Computational Study of Lithium-Ion Mobility in Stoichiometric Solid-State Systems

Alex Mulliner

Lincoln College, University of Oxford



A dissertation submitted to the University of Oxford for the degree of Doctor of Philosophy in Inorganic Chemistry

Trinity Term 2015

Computational Study of Lithium-Ion Mobility in Stoichiometric Solid-State Systems

Alex Mulliner, Lincoln College

A dissertation submitted to the University of Oxford for the degree of Doctor of Philosophy in Inorganic Chemistry

Trinity Term 2015

Abstract

Lithium-ion mobility in solid-state systems is an important field with significance for a range of technological interests, especially in the field of energy materials. The binary lithium compounds Li_2O and Li_3N have been studied using modern computational techniques to elucidate their diffusion properties. The macroscopic diffusion coefficients have been calculated and the underlying microscopic diffusion processes elucidated using molecular-dynamics-based techniques. In both systems studied the diffusion has been modelled over a wider temperature range than previously attempted. The agreement between the calculated diffusion coefficients and the best available experimental data surpasses previous computational studies. The level of agreement achieved is due to the use of force-field non-equilibrium molecular dynamics (FF-NEMD). This method, which has only recently been applied to solid-state diffusion, allows rates of diffusion that are typically too low to be studied with equilibrium molecular dynamics to be modelled. NEMD uses a fictitious external field to increase the frequency of the rare diffusion events in a predictable manner without changing the nature of the diffusion mechanisms. In the case of Li_2O the transition from the non-superionic to the superionic regime has been modelled. The dominant mechanism in each regime has been determined: in the non-superionic regime a concerted mechanism dominates and in the superionic regime an interstitial-mediated mechanism dominates. For Li_3N the anisotropic nature of the lithium diffusion coefficient has been modelled. The diffusion mechanisms dominant for different directions have also been elucidated. The rapid diffusion in the (001) plane of the hexagonal structure has been explained by the presence of vacancies on the in-plane Li sites, both in this thesis and in previous works. Previous studies have explained this by the presence of contaminants leading to non-stoichiometric Li_3N. However, in this thesis the under occupation of these sites has been explained by the formation of Li_2 dumbbells, or site sharing, largely about the interlayer Li sites, but also about the in-plane Li sites. The existence of these dumbbells explains the experimental diffusion coefficients of stoichiometric Li_3N.

Acknowledgments

This doctoral thesis could not have happened without the help of the following people and organizations. To these I am very grateful.

My supervisors Bill David (Rutherford Appleton Laboratory and University of Oxford) and Peter Battle(University of Oxford) have provided endless guidance and support at all stages of this thesis. I would also like to thank Keith Refson (Rutherford Appleton Laboratory and Royal Holloway) and Philippe Aeberhard (University of Oxford) for their help and advice.

The calculations performed in this thesis would not have been possible without access to high-performance computing resources. These were provided by the UK Car-Parrinello Consortium (EPSRC Grants EP/F036809/1 and EP/K013750/1) and the e-science facility of the Science and Technology Facilities Council (STFC). I would like to thank the STFC for providing the funding for my DPhil scholarship.

Finally I would like to thank my friends, family and Ana for all their love and support.

Contents

Abstract i

Acknowledgments ii

1 Introduction To Diffusion In Ionic Solids 1

1.1 Diffusion in Solids . . . 2

1.2 Superionic Behaviour . . . 6

1.3 Scope and aim of this work . . . 8

2 The Diffusion Coefficient; Definition and Determination 11

2.1 Fick's Law . . . 11

2.2 Random-Walk Diffusion . . . 14

2.3 The Green-Kubo Formalism . . . 20

2.4 The Arrhenius Model . . . 22

2.5 The Nernst-Einstein Relation . . . 23

2.6 The Determination of Diffusion Coefficients: Experimental and Computational Methods 26

2.7 Density Functional Theory . . . 28

2.7.1 The Hohenberg-Kohn Theorems . . . 29

2.7.2 The Kohn-Sham Approach . . . 32

2.7.3 Exchange-correlation Functionals . . . 35

2.7.4 Bloch's Theorem . . . 36

2.7.5 Basis Sets . . . 37

2.7.6 Pseudopotentials . . . 37

2.7.7 Mulliken Population Analysis . . . 38

2.8 Force-Field . . . 38

2.9 Statistical Mechanics . . . 40

2.10 Molecular Dynamics . . . 41

2.10.1 Equations of Motion . . . 42

2.10.2 Gaussian Isokinetic Thermostat 45
2.10.3 Drift in Conserved Quantities 46
2.11 Limitations of Molecular Dynamics 46
2.12 Non-Equilibrium Molecular Dynamics 47
2.12.1 Linear Response Theory 50
2.12.2 Synthetic NEMD Algorithm for Self-diffusion in Solids 52
2.12.3 Calculating Self-diffusion Coefficients from NEMD Simulations 55

3 Li_2O **57**

3.1 Fluorite Structure 57
3.2 Superionic Diffusion in Li_2O 59
3.3 Computational Details 62
3.3.1 Density Functional Theory 67
3.4 Equilibrium Molecular Dynamics 68
3.5 Non-equilibrium Molecular Dynamics 69
3.5.1 FF-NEMD Simulation at 1273 K 70
3.5.2 Comparison of Computational Methods at 1273 K 72
3.5.3 Temperature Dependence of Self-diffusion Coefficient 73
3.6 Conclusion 92

4 Li_3N **94**

4.1 Crystal Structure 94
4.2 Bonding in Li_3N 95
4.3 Superionic Behaviour 96
4.4 Computational Details 98
4.5 Results and Discussion 102
4.5.1 Temperature Dependence of the Lithium Diffusion Coefficient 102
4.5.2 Vertical Dumbbell Around the Li(2) Site 104
4.5.3 Horizontal Dumbbell Around the Li(1) Site 108
4.5.4 Mechanisms of Diffusion Along [001] 113
4.5.5 Energy Profiles of Diffusion 119
4.5.6 Macroscopic Diffusion 122

4.6 Conclusion 130

5 Conclusion and Outlook **133**

5.1 Future Work 135

References **137**

Appendix I **152**

CHAPTER 1

Introduction To Diffusion In Ionic Solids

Diffusion is the movement of matter over time due to the thermal motion of the individual particles forming the system. In gas phases, diffusion proceeds at rates of approximately $1\,\mathrm{cm^2\,s^{-1}}$ and in liquids at approximately $100\,\mu\mathrm{m^2\,s^{-1}}$. In the solid-state the typical rates of diffusion are extremely slow, e.g. approximately $10^{-14}\,\mathrm{m^2\,s^{-1}}$ for Na in NaCl at 600 K (Laskar, 1990), but they can range over several orders of magnitude. At high temperatures, close to the melting point, rates of diffusion are typically of the order of $10^{-6}\,\mathrm{m^2\,s^{-1}}$. The rate of diffusion is thus significantly temperature dependent. This thesis is concerned with diffusion in ionic solids and the issues associated with studying such a relatively slow process. Solid-state ionic diffusion is a fundamental scientific process, which is paramount to a range of technological systems. Despite the importance of ionic diffusion in solid systems, our current understanding is limited. Before the scope and aims of this thesis are defined, a broad discussion of diffusion and ionic mobility, the systems to be studied and the methods to be utilized will be presented.

The first quantitative studies of diffusion were performed by Thomas Graham and were concerned with the intermixing of gases (Graham, 1829, 1833). Later he extended his work to the diffusion of salt in water (Graham, 1850), showing the rate of diffusion to be many times slower in liquids than in gases. Graham's work on gases was understood using the kinetic theory of gases, which linked the thermal motion of individual particles to the diffusion. His work on diffusion of salt in water was the basis for Fick's laws, which will be described below. William Chandler Roberts-Austen was the first to extend Graham's understanding of diffusion in gases to solid-state diffusion (Roberts-Austen, 1896). Work by Jakov Il'ich Frenkel gave rise to the idea of disorder in solid crystals (Frenkel, 1926). He suggested atoms in the solid state moved from regular lattice sites to interstitial sites, thus creating a vacancy on a regular lattice site. This is now known as a Frenkel defect. The field of disorder in the solid state was furthered by Wagner and Schottky (1930) and has been closely related to the study of solid-state diffusion. Research into solid-state diffusion advanced in the 1930's when

it become possible to perform radioactive-tracer measurements of diffusion coefficients. This greatly improved the precision of measured diffusion coefficients and increased the temperature range over which they could be measured in solids.

1.1 Diffusion in Solids

The diffusion of mobile ions in solids is dominated by movement of atoms between regular lattice sites, whereas in liquids and gaseous systems the ions can move in any direction for a range of distances. In most solid, crystalline structures, diffusion typically occurs only in the presence of Frenkel defects. If vacancies exist on the regular lattice sites then the diffusion is usually dominated by the movement of vacancies i.e. vacancy diffusion. In this situation diffusion is often discussed not in terms of the movement of the mobile ions, but by the movement of the vacancies. Solid-state diffusion occurs in all types of solids, but this thesis focuses on diffusion in ionic crystals. However, the majority of what is discussed is applicable to diffusion in most systems. Diffusion of ions accounts for the electrical conductivity of ionic solids; given there are no free electrons, the electric current is carried by the ions. There is a close relationship between the ionic conductivity and the self-diffusion. This means the study of diffusion in ionic solids is often of significant importance to their technological applications.

Specific to solid-state diffusion in ionic solids is the necessity for overall charge neutrality. This links the number of cation vacancies to the number of anion vacancies and vice versa, unless there is a charge compensation mechanism such as in the case of La-doped $BaTiO_3$ (Morrison et al., 2001). Ionic solids can be roughly separated into two classes: fast-ion conductors and classical-ion conductors (Kumar and Yashonath, 2006). In classical-ion conductors, e.g. NaCl or CsCl, the diffusion is dominated by the presence and movement of vacancies. Superionic conductors, e.g. AgI, typically have a relatively more open structure that allows for the rapid movement of small ions. Fast-ion conductors can be considered separate from classical-ion conductors due to their exceptionally high ionic conductivities (Hull, 2004). At temperatures above absolute zero vacancies will be present. A lattice vacancy, also known as a Schottky defect, occurs when an atom or ion is missing from the regular lattice in the bulk and located on the surface. In ionic crystals Schottky defects involve the transfer of an equal number of anions and cations from the bulk to the surface in order to maintain electrostatic neutrality in the region of the vacancy. The Frenkel defect is another defect common in solid crystalline structures where an ion is displaced from its regular lattice site to

an interstitial creating a vacancy on the regular lattice. These intrinsic defects typically dominate the diffusion only at high temperatures due to their high formation energies. Extrinsic defects, typically associated with aliovalent impurities or dopants, dominate the diffusion at lower temperatures. The presence of an aliovalent ion on one sublattice requires a modification of the stoichiometry on the other sublattice, thus creating disorder and promoting diffusion. In the presence of vacancies, the diffusion is dominated by the exchange of the vacancy and an adjacent atom. Diffusion is measured by the diffusion coefficient as introduced by Fick. For ionic solids the diffusion coefficient is related to the frequency of the hopping of atoms, as well as geometric and kinetic considerations.

In a crystalline solid where atoms are located on lattice sites the diffusion pathways are limited by the structure, particularly the local environment of the mobile species. In a gas the diffusion consists of a distribution of hop lengths and directions. In liquids and amorphous solids the diffusion can be classified as somewhere between the random nature of gases and the ordered nature of crystalline solids. The hopping in solids can either consist of a series of random hops or the hops can be correlated. The correlation of random hops often occurs where there are defect-mediated processes or the direction of an individual hop is affected by the direction of the previous hop. There are three basic mechanisms of diffusion; interchange by rotation of two or more atoms in concert, movement via an interstitial site, and displacement of a vacancy on the lattice. Often the latter two mechanisms operate together in a system where the regular mobile ion sites are fully occupied. The diffusion mechanisms therefore play a crucial role in the ionic conductivity of solid-state batteries and other such devices. Diffusion in a pure crystal can involve multiple types of diffusion and accompanying mechanisms. Direct interstitial mechanisms involve an atom diffusing throughout the crystal via interstitial sites of the lattice. This is typically observed for very small atoms diffusing through a host consisting of much larger atoms. The small atom diffusing through does not alter the host lattice to a significant degree due to the size difference and the pathways through the solid. This mechanism is important for the diffusion of dopants. Rotation by multiple atoms is a collective mechanism and typically involves the atoms moving around a ring. This does not require the presence of lattice defects or vacancies, but the associated activation energy varies greatly depending on the structure because of the often-large distortions from equilibrium positions required to accommodate the movements. The vacancy mechanism involves the diffusion of a lattice vacancy throughout the crystal. It is the dominant source of diffusion in solids (Mehrer, 2007; Borg and Dienes, 2012). An extension of the vacancy mechanism is the divacancy mechanism, where a

binding energy exists between neighbouring vacancies. The formation of a divacancy becomes more probable as temperature increases, and in fcc metals divacancies are more mobile than monovacancies (Mehrer, 1978; Peterson, 1978). Different diffusion mechanisms may dominate in different temperature ranges due to the different activation energies associated with each mechanism, hence leading to a temperature-dependent diffusion coefficient.

Diffusion does not only occur in the bulk, but also along the surface and grain boundaries. The rates of diffusion have been shown to be much lower in the bulk than on the surface or along grain boundaries (Gjostein, 1973; Martin and Perraillon, 1975; Peterson, 1980, 1983). The boundaries can be sources or sinks for mobile species, creating a net transport of atoms and possibly a concentration gradient. In Fig. 1.1 the diffusivity as a function of temperature of silver atoms in pure, solid silver is shown. The diffusivity is measured by the diffusion coefficient, which is a measure of the number of the mobile species passing through an area in a given time. The theoretical formulation of the diffusion coefficient will be covered in Chapter 2. The diffusion coefficients in Fig. 1.1 are represented on an Arrhenius plot. The temperature dependence of the diffusion coefficient is typically described by the Arrhenius equation:

$$D = D_0 \exp\left(\frac{-E_a}{k_B T}\right), \tag{1.1}$$

where D_0 is a pre-exponential frequency factor, E_a is the activation energy, and k_B is the Boltzmann constant. Often the Arrhenius equation is written as:

$$\ln D = \ln D_0 - \frac{E_a}{k_b T}. \tag{1.2}$$

The pre-exponential frequency factor is usually of the order of molecular or lattice vibrations. In the case of silver, the Arrhenius plot shows the rate of diffusion along the surface to be approximately five orders of magnitude faster than in the bulk, despite being measured at lower temperatures. The grain boundary diffusivity is roughly half way between the surface and the bulk rates.

In the solid state, where mobile ions diffuse through a regular lattice, the ions move by a series of individual atomic-jump processes. Typically the individual mobile ion moves from one regular lattice site to a nearest-neighbour regular lattice site. The path this ion follows involves moving past the intervening atoms on the regular lattice. The movement from one energy minimum to another requires enough energy to overcome the height of the energy barrier, or as it is usually

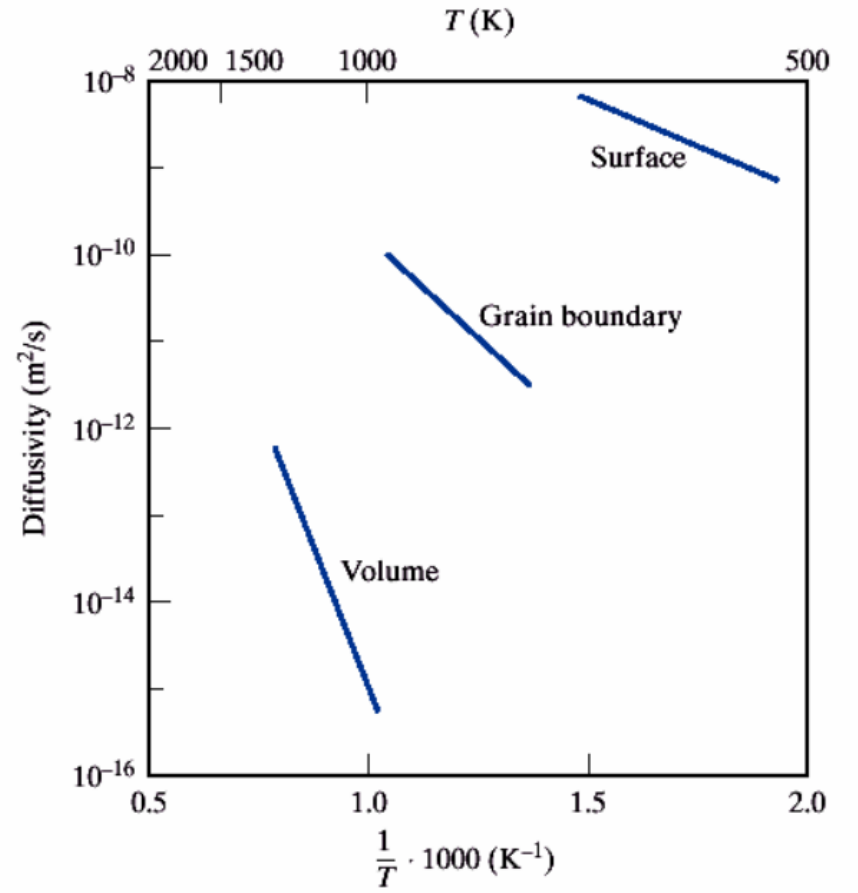


Figure 1.1: Self-diffusion coefficients of Ag for different local micro structures (Brophy et al., 1964).

known the activation energy. Typically in ionic solids the ions oscillate about their equilibrium positions on the regular lattice sites due to the presence of thermal energy. However, the thermal energy is usually much smaller than the activation energy, therefore such ion hops are infrequent. The frequency of such events is much lower than the frequency of lattice vibrations of ionic solids, which are approximately in the range $10^{12} - 10^{13}\,\mathrm{s}^{-1}$.

1.2 Superionic Behaviour

Superionic conductors are solid-state materials that allow the macroscopic diffusion of mobile ions at a similar rate as in liquids, usually at high temperatures close to the melting point. Typically, this involves the movement of the mobile ion species through a relatively static framework. Typical conductivities for ionic solids e.g. NaCl are of the order $\sigma \approx 10^{-8}\,\Omega^{-1}\,\mathrm{cm}^{-1}$ at 200 °C whereas for superionic conductors, e.g. β-Al_2O_3, $\sigma \approx 1\,\Omega^{-1}\,\mathrm{cm}^{-1}$. Superionic conductors are often referred to as fast-ion conductors or solid electrolytes. Initial observations of superionic conductivity were made by Michael Faraday, who observed Ag_2S and hot PbF_2 conducting electricity (Faraday, 1939). Later electrical conductivity was observed in AgI by Tubandt and Lorenz (1914). At temperatures above 147 °C the ionic conductivity was analogous to the conductivity of liquid electrolytes. Throughout the twentieth century the number of known superionic conductors increased. Notable developments include the observation of Na^+ ion conductivity in sodium β-alumina (Yu Yao and Kummer, 1967; Kummer, 1972) and O^{2-} ion conduction in stabilized zirconias (Kingery et al., 1959; Simpson and Carter, 1966). Yttrium-stabilized zirconia and PbF_2 are just two of the many materials that adopt the fluorite structure and exhibit superionic conductivity. The fluorite structure will be discussed in greater detail in Section 3.1. Most solid-state superionic conductors have a relatively open structure, where the mobile ions can readily move between nearest-neighbour sites. Also common among superionic conductors is the relatively small size and low charge of the mobile ion. There are many models to explain the microscopic processes underlying the macroscopic superionic conductivity, but except in a few cases there is still uncertainty, especially regarding many-particles effects such as correlated movement and interactions with the surrounding lattice (Yugami and Ishigame, 1993). Solid-state superionic conductors are still being studied with improvements being made. One key area of interest is lowering the temperature range in which the materials exhibit high enough conductivities to be of use in technological applications (Kamaya et al., 2011; Wachsman and Lee, 2011). Solid-state superionic conductors have many technological uses and have been considered for a lot more. Superionic

materials with high Li^+ conductivities are used in Li-ion batteries in both cathode and electrolyte materials (Tarascon and Armand, 2001). Polymer electrolytes, which consist of mixing polymers and ionic salts, have shown high ionic conductivities over reasonable temperature ranges and have been of great technological interest since their discovery (Fenton et al., 1973). Polyethylene oxide and polypropylene oxide salt complexes started the technological interest in polymer electrolytes (Armand et al., 1979) and have subsequently been implemented in Li-ion batteries (Wright, 2002). Oxide-conducting yttria-stabilized zirconia has been implemented in solid-oxide fuel cells and can be used in oxygen sensors (Steele, 1992). In most batteries the electrolyte is liquid or aqueous, but if it is replaced with a solid-electrolyte then two major problems can be avoided: consumption of the liquid electrolyte during the charging and corrosion of the electrodes by the electrolyte (Julien, 1990). This in addition to the safety improvements introduced by not having a liquid electrolyte.

There are three classifications of superionic materials as proposed by Boyce and Huberman (1979). The solids are classified by the nature of the transition from non-superionic to superionic regions.

1. **Type I** superionic conductors have a well defined first-order phase transition. AgI is a prototypical type I superionic conductor where the ionic conductivity increases by four orders of magnitude through the transition from the beta to the alpha phase at 420 K.

2. **Type II** superionic conductors show a gradual and continuous change in the conductivity with no accompanying first-order phase transition. The concentration of conducting defects increases with temperature, and typically the conductivity has an exponential relationship with temperature. This is often accompanied by a change in the specific heat. Compounds, for example PbF_2, CaF_2 and $SrCl_2$, that adopt the fluorite structure are typical of type II superionic conductors. Unlike type I superionic conductors, type II materials show no sudden change in the degree of disorder on the immobile sublattice.

3. **Type III** superionic conductors show an exponential growth in the conductivity with no clear phase transition and no anomaly in the specific heat. Unlike type I and II, type II conductors have at least on constituent ion highly delocalized over the available sites. Unlike type II superionic conductors that rely on a defect-mediated mechanism the mechanism typically present in type III is interstitial mediated (Kumar and Yashonath, 2006). Na-β-Al_2O_3 is typical of type III. The difference between type III and type II conductors is illustrated in Fig. 1.2 on a

logarithmic scale only the conductivity of the former has a linear variation with $^1/_T$.

For a material to exhibit superionic conductivity it must have an easy pathway for mobile ions between lattice sites. Usually this means smaller ions moving through a relatively static sublattice. Movement of larger cations is possible but only in the presence of highly polarisable anions. The pathway between adjacent lattice sites must be continuous in order to allow for macroscopic movement of cations. Otherwise there may be a very high hopping frequency, but no discernible macroscopic movement. The energy of the pathways must be comparable to the thermal energy of the temperature range in which the system is a solid. This can be a problem when measuring diffusion with an indirect method, see Chapter 2. Finally, to maximise the rate of movement there must be more sites for the mobile ions than there are mobile ions. Alternatively there must be vacancies present on the regular lattice of the mobile species. The movement, or hop, of a mobile ion from one site to another involves the activation energy of the hop itself, which will affect the temperature dependence of ionic conductivity, but also the energy difference between the two sites. If the two sites are structurally inequivalent, the movement from the regular lattice to an interstitial for example, then they will most likely be energetically inequivalent. This is why in face-centred cubic structures, where mobile ions move typically between structurally inequivalent tetrahedral and octahedral sites, the conductivities are low compared to those of body-centred cubic structures, where mobile ions move between structurally equivalent tetrahedral sites (Boyce and Huberman, 1979).

The mobile cation in the compounds to be considered in this thesis is Li^+.

1.3 Scope and aim of this work

In this thesis modern computational methods are used to study the diffusion properties of Li_2O and Li_3N. These superionic compounds were chosen as they are prototypical lithium-ion solid-state conductors. They are simple in regard to structure and composition and they have been studied extensively with an array of experimental methods, which allows direct comparison to the computational results.

In Chapter 2 the methods used in this thesis are explained in detail and the fundamental theories behind these methods are explained.

In Chapter 3 the temperature dependence of the lithium diffusion in Li_2O is modeled with an

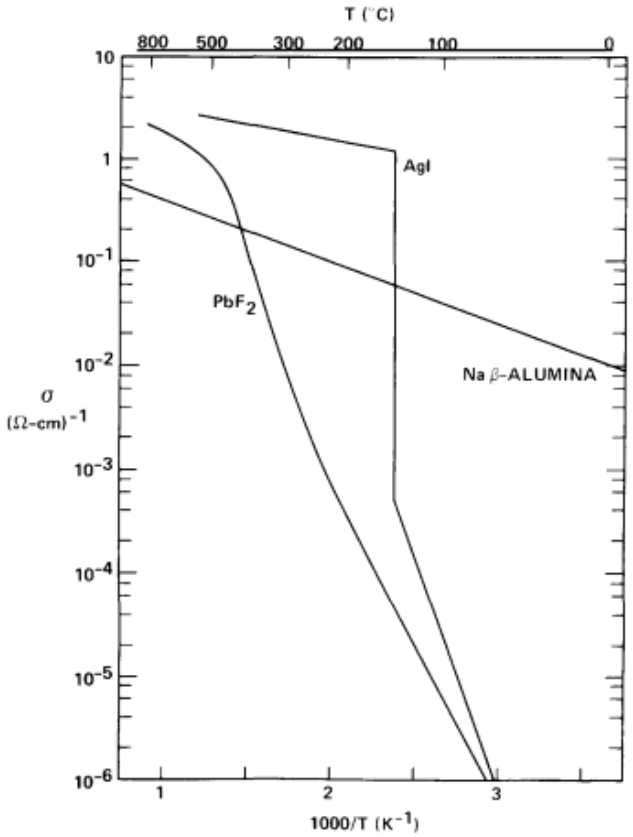


Figure 1.2: Conductivities of AgI (Type I), PbF_2 (Type II), and Na-β-Al_2O_3 (Type III) showing the three types of behaviour observed on going from the low temperature ionic-insulating to the high temperature superionic state (Boyce and Huberman, 1979).

unprecedented level of accuracy and precision. The origin of the diffusion is elucidated through the different diffusion pathways observed. The non-superionic regime is studied with efficacy for the first time.

Chapter 4 describes a similar study of Li_3N. The concerted nature of the diffusion events both in the (001) plane of the hexagonal structure and perpendicular to the plane has been elucidated.

Finally chapter 5 summarizes the results of these studies and suggests further studies that could be carried out in the future.

CHAPTER 2

The Diffusion Coefficient; Definition and Determination

As discussed in Chapter 1, diffusion occurs in gases, liquids and solids, but is typically much faster in gases and liquids than in solids. Diffusion is measured as the change in concentration at a given distance from a release point after a given time. The measure of diffusion is the diffusion coefficient, which can be obtained from experimental and computational methods. In the case of solids, diffusion rates analogous to those observed in gases and liquids may occur at high temperatures. Solid-state diffusion can occur within the lattice or along surfaces, grain boundaries, or dislocations. In the latter three cases the diffusion is usually referred to as short-circuit diffusion. Diffusion thus refers to the net transport of atoms, ions or molecules, usually under a driving force. This driving force typically takes the form of a concentration gradient where a net movement occurs from a region of high concentration to a region of low concentration. This thesis is concerned with diffusion in crystalline solid-state systems in the absence of a concentration gradient, i.e. self-diffusion. In these cases diffusion occurs as a result of thermal motion. The two main theories on which the science of diffusion is based are Fick's laws and Einstein's interpretation. Fick's laws provide a continuum theory derived from the diffusion of salt in water whereas Einstein's theory was derived from Brownian motion and described the erratic motion as a random walk.

2.1 Fick's Law

The equations describing diffusion are Fick's laws of diffusion. They were derived by Adolf Fick in 1855 to describe the diffusion in a salt-water system (Fick, 1855, 1995) - the later reference is a modern translation of his seminal work. This was the first introduction of the diffusion coefficient which was related to the linear concentration gradient. Prior to Fick's description of diffusion, an

analogous description of heat flow as a property of temperature gradient was suggested by Josef Fourier in 1807 (Fourier, 1807).

The flux of ions diffusing in one dimension and under steady-state conditions is described by Fick's first law:

$$J(x) = -D\frac{\partial C}{\partial x}, \tag{2.1}$$

where D is the diffusion coefficient, C is the concentration or number density, x is the position, and $J(x)$ is the particle flux. The flux is the number of particles going though a given area in a given time period. In the SI system it is measured in units of $\mathrm{m}^2\,\mathrm{s}^{-1}$. In order to consider diffusion in three dimensions this can readily be extended to:

$$\mathbf{J}(x, y, z) = -D\nabla C, \tag{2.2}$$

where $\mathbf{J}(x, y, z)$ is the vector of diffusion flux. The form of Fick's first law can change as Eqn. 2.2 is for a isotropic system. For anisotropic systems the diffusion coefficient depends on direction:

$$\mathbf{J} = -\mathbf{D}\nabla C, \tag{2.3}$$

where $\mathbf{D}$ is the second-rank tensor for diffusivity (Nye, 1957). This second-rank tensor is symmetric and therefore can be transformed to three principal axes:

$$\mathbf{D} = \begin{pmatrix} D_1 & 0 & 0 \\ 0 & D_2 & 0 \\ 0 & 0 & D_3 \end{pmatrix}, \tag{2.4}$$

where D_i are the individual principal diffusion coefficients for $i = 1, 2, 3$. There can be no more than three principal diffusion coefficients, but there can be fewer. The other six, or more, matrix elements define the relative orientations of the principal axes. If x_i are the principal axes and J_i are the components of diffusion flux:

$$J_i = -D_i\frac{\partial C}{\partial x_i}. \tag{2.5}$$

For cubic crystals the principal diffusion coefficients are:

$$D_1 = D_2 = D_3. \tag{2.6}$$

For tetragonal, trigonal, and hexagonal crystal systems, using the convention that the third axis is the unique axis, the principal diffusion coefficients are:

$$D_1 = D_2 \neq D_3. \tag{2.7}$$

And finally for triclinic, monoclinic and orthorhombic crystal systems:

$$D_1 \neq D_2 \neq D_3. \tag{2.8}$$

In the majority of solid-state diffusion processes the number of mobile ions is conserved, as typically there are no chemical reactions removing or adding mobile ions. Consider a point P in a Cartesian coordinate system at location (x, y, z) and a box of dimension $(\triangle x, \triangle y, \triangle z)$ with $\alpha = \beta = \gamma = 90°$ which diffusing ions move through. The flux $\mathbf{J}$ is comprised of the three orthogonal fluxes J_x, J_y, J_z. If the sum of these three fluxes is not zero then there is a net change in the number of diffusing ions in the volume. The rate of change in the number of diffusing ions in this volume, $\frac{\partial C}{\partial t}\triangle x \triangle y \triangle z$, can be described for a single direction as the difference in fluxes between opposite faces of the box multiplied by their area. For three dimensions it follows that:

$$\frac{\partial C}{\partial t}\triangle x \triangle y \triangle z = \left[J_x(P) - J_x(P + \triangle x)\right] \triangle y \triangle z + \left[J_y(P) - J_y(P + \triangle y)\right] \triangle x \triangle z + \left[J_z(P) - J_z(P + \triangle z)\right] \triangle x \triangle y. \tag{2.9}$$

The individual flux components can be replaced with the a Taylor expansion. Using the expansion up to the linear term Eqn. 2.9 becomes:

$$\frac{\partial C}{\partial t}\triangle x \triangle y \triangle z \approx -\left[\frac{\partial J_x}{\partial x} + \frac{\partial J_y}{\partial y} + \frac{\partial J_z}{\partial z}\right] \triangle x \triangle y \triangle z. \tag{2.10}$$

Eqn. 2.10 becomes exact as the volume tends to zero and can then be rewritten using the vector divergence operator, ∇, to give the continuity equation:

$$\frac{\partial C}{\partial t} = -\nabla \cdot \mathbf{J}. \tag{2.11}$$

Combining Fick's first law (Eqn. 2.2) with the continuity equation (Eqn. 2.11) we arrive at the diffusion equation or Fick's second law:

$$\frac{\partial C}{\partial t} = \nabla \cdot (D \nabla C). \tag{2.12}$$

For chemically homogeneous systems Fick's second law reduces to:

$$\frac{\partial C}{\partial t} = D \triangle C, \tag{2.13}$$

where $\triangle$ is the Laplacian operator and the result is often referred to as the linear diffusion equation.

2.2 Random-Walk Diffusion

Random diffusion on a microscopic level is the movement of atoms, ions, or molecules due to Brownian motion unless there is a driving force present. Random-walk diffusion is the simplest model for diffusion, but can provide a deep understanding as it is based on the underlying driving forces of diffusion whereas Fick's laws are descriptions of the measured diffusion phenomena. In solids the random walk involves a series of random hops between regular lattice sites due to thermal energy. Macroscopic diffusion is the net result of many individual ion hops. The distances of the individual jumps are defined by the lattice parameters and the structure. These individual hops can be characterized by physical quantities such as distances, energy barriers and frequencies. The rate of diffusion is determined by a number of factors, especially the thermal energy, but also the activation energy, E_a, of the individual hop pathways and the attempt frequency, which is comparable to the Debye frequency, and will be discussed in more detail in Section 2.4. The random-walk model provides a way to connect the physical parameters defining an individual hop to the diffusion coefficient and macroscopic diffusion. With no concentration gradient or external forces the net displacement for any number of particles will be zero, but measurable diffusion does occur along identifiable pathways. Consider the unidirectional hopping of an ion in a simple cubic crystal, where there is a low concentration of mobile ions, to a nearest-neighbour, vacant site. The hop length is defined as λ,

with a concentration gradient along the x axis, and a hopping rate of Γ with dimension t^{-1}. If there are two planes, labelled 1 and 2, orthogonal to the x direction and separated by a distance λ, then the number of interstitials in the two planes is n_i per area. If there is no driving force then the hopping rate will be equal forward and backwards along x. Therefore the flux J can be written as:

$$J_x = \Gamma(n_1 - n_2). \tag{2.14}$$

The concentrations for each plane can be defined as:

$$C_i = \frac{n_i}{\lambda}. \tag{2.15}$$

If the concentration along x changes slowly with distance, as is usually the case in diffusion, then using a Taylor expansion the difference in concentrations becomes:

$$C_1 - C_2 = -\lambda \frac{\partial C}{\partial x}. \tag{2.16}$$

Using the definition in Eqn. 2.15 and difference in Eqn. 2.16, the flux along x (Eqn. 2.14) is:

$$J_x = -\lambda^2 \Gamma \frac{\partial C}{\partial x}. \tag{2.17}$$

Comparing the above equation to Fick's first law (Eqn. 2.1) an expression for the diffusion coefficient can be written:

$$D = \Gamma \lambda^2. \tag{2.18}$$

This result shows the diffusion coefficient is equal to the jump rate multiplied by the square of the distance of the jump. This is a general result and the jump rate is determined not only by kinetic factors, but also geometric considerations of the crystal being investigated.

Extending the random walk to three-dimensions then the total displacement, $\mathbf{R}$, is the path of the particle comprised by a series of individual hops, $\mathbf{r}_i$. For N hops this is:

$$\mathbf{R} = \sum_{i=1}^{N} \mathbf{r}_i. \tag{2.19}$$

The total squared-displacement can be separated into its Cartesian components:

$$R^2(x,y,z) = X^2 + Y^2 + Z^2. \tag{2.20}$$

If the diffusion is measured from time t_0 to time t then the displacements along the x direction can be described by a normalized distribution function $W(X, \triangle t)$ where $\triangle t = t - t_0$. The distribution function gives the probability of a particles having travelled a distance X along the x axis after a time period of $\triangle t$. If a steady-state is assumed then the distribution function is independent of origin or direction, and merely a function of the distance and time. The concentration, C, after a given time $t + \triangle t$ at distance X is:

$$C(x, t + \triangle t) = \sum_X C(x - X, t)W(X, \triangle t). \tag{2.21}$$

The concentrations can be expanded about $X = 0$ and $\triangle t = 0$ to give:

$$C(x,t) + \triangle t \frac{\partial C}{\partial \triangle t} + \cdots = \sum_X \left[C(x,t) - X\frac{\partial C}{\partial x} + \frac{X^2}{2}\frac{\partial^2 C}{\partial x^2} + \cdots \right] W(X, \triangle t). \tag{2.22}$$

The higher-order terms on the left-hand side are negligible for small vales of $\triangle t$. If $\triangle t$ is small then the distribution function will be located near to $X = 0$ and therefore higher order terms on the right-hand side are also negligible. As the distribution function is normalized:

$$\sum_X W(X, \triangle t) = 1, \tag{2.23}$$

it follows that

$$\sum_X W^n(X, \triangle t) = \langle X^n \rangle . \tag{2.24}$$

For the case of $n = 2$ the term$\langle X^2 \rangle$ is usually referred to as the mean-squared displacement. Combing Eqn. 2.22 and Eqn. 2.24:

$$\frac{\partial C}{\partial t} = -\frac{\langle X \rangle}{\triangle t}\frac{\partial C}{\partial x} + \frac{\langle X^2 \rangle}{2\triangle t}\frac{\partial^2 C}{\partial x^2}. \tag{2.25}$$

For many particles the term $\langle X \rangle$ should be zero unless there is an external force leading to a overall drift of the mobile ions. If we assume no external force then Eqn. 2.25 becomes:

$$\frac{\partial C}{\partial t} = \frac{\langle X^2 \rangle}{2\triangle t} \frac{\partial^2 C}{\partial x^2}. \tag{2.26}$$

When considering linear diffusion it can be shown (Mehrer, 2007) that Fick's second law can be written as:

$$\frac{\partial C}{\partial t} = D \frac{\partial^2 C}{\partial x^2}. \tag{2.27}$$

Comparing Eqn. 2.26 to Eqn. 2.27, an expression for the diffusion coefficient can be found:

$$D_x = \frac{1}{2\triangle t} \langle X^2 \rangle . \tag{2.28}$$

Equivalent expressions can be derived for the y and z directions for cubic systems. The total displacement is related by:

$$\langle X^2 \rangle \equiv \langle Y^2 \rangle \equiv \langle Z^2 \rangle = \frac{1}{3} \langle \mathbf{R}^2 \rangle . \tag{2.29}$$

The general form of Eqn. 2.28 is:

$$D = \frac{1}{2d\triangle t} \langle \mathbf{R}^2 \rangle , \tag{2.30}$$

where d is the dimensionality. This is the Einstein-Sutherland relation. The Einstein-Smoluchowski relation can be derived from this if an uncorrelated random walk is considered on a three-dimensional lattice where hopping only occurs between nearest neighbours separated by the length a. After N hops the mean squared displacement is:

$$\langle R^2 \rangle = \sum_{i=1}^{N} \langle \mathbf{r}_i^2 \rangle , \tag{2.31}$$

$$\langle R^2 \rangle = \langle N \rangle a^2. \tag{2.32}$$

If the mobile ion can move to any nearest neighbour site then the number of possible sites is the same as the coordination number Z. The jump rate, Γ, can be defined as:

$$\Gamma = \frac{\langle N \rangle}{Zt}, \tag{2.33}$$

the average number of jumps per time per possible pathway. Substituting Eqn. 2.33 and 2.32 into Eqn. 2.30 the diffusion coefficient can be written as:

$$D = \frac{1}{6} a^2 Z \Gamma. \tag{2.34}$$

The jump rate and coordination number can be used to define the mean residence time of a mobile ion on a given site:

$$\bar{\tau} = \frac{1}{Z\Gamma}. \tag{2.35}$$

Using this definition the diffusion coefficient becomes:

$$D = \frac{a^2}{6\bar{\tau}}. \tag{2.36}$$

The Einstein-Smoluchowski relation is used to relate indirect measurements of diffusion-related processes to the diffusion coefficients. With this formulation the diffusion coefficient is proportional to the jump rate, coordination number, and the distance of the jump. Random-walk diffusion involves a series of independent jumps; there is no memory between jumps. Considering the diffusion of a vacancy throughout a crystal, if the vacancy exchanges positions with a labelled atom on an adjacent site the vacancy and the labelled atom have moved in opposite directions. For macroscopic diffusion to occur this vacancy must continue to diffuse through the system. However, after the initial exchange of the labelled atom and the vacancy they are still adjacent and there is a possibility that the exchange is reversed, leading to no net movement. The diffusion of both the vacancy and the labelled atom is less than would be expected from a series of uncorrelated hops, as described by random-walk diffusion. This is important when considering radioisotope tracer diffusion experimental methods. In these experiments a stable isotope of the diffusing species of interest is used as a label. This isotope is then deposited on the surface or implanted into the solid and an isothermal diffusion anneal is performed at a given temperature for a specific time. Then the concentration of the isotopes is measured as a function of distance from deposition. The concentration of the isotope at a given depth is related to the diffusion coefficient. The correlation factor, f, was introduced (Bardeen and

Herring, 1951, 1952) to account for the difference between random-walk diffusion and diffusion of a tracer:

$$f = \frac{\left\langle \mathbf{R}^2_{tracer} \right\rangle}{\langle \mathbf{R}^2_{random} \rangle}, \tag{2.37}$$

$$f = \frac{D^*}{D_{random}}. \tag{2.38}$$

The correlation factor is dependent on both the type of lattice and the diffusion mechanisms present. For a direct interstitial diffusion $f = 1$ where the hopping is uncorrelated and where the diffusion is equally probable in all directions.This is valid when the number of interstitial atoms is much less than the number of vacant sites. This is not typically the case for ionic solids.. The correlation factor can be written as:

$$f = \lim_{N\to\infty} \frac{\left\langle \mathbf{R}^2_{tracer} \right\rangle}{\langle \mathbf{R}^2_{random} \rangle}, \tag{2.39}$$

where N is the number of hops. The is can be expanded into two terms:

$$f = 1 + 2 \lim_{N\to\infty} \frac{\sum_{i=1}^{N-1} \sum_{j=i+1}^{N} \langle \mathbf{r}_i \cdot \mathbf{r}_j \rangle}{\sum_{i=1}^{N} \langle \mathbf{r}_i^2 \rangle}. \tag{2.40}$$

The first term represents the uncorrelated diffusion and the second term is for the correlation of hops. For a random walk the second term is zero. This can be re-written as:

$$f = 1 + \lim_{N\to\infty} \frac{2}{N} \sum_{i=1}^{N-1} \sum_{j=1}^{N-i} \langle \cos\theta_{i,i+j} \rangle, \tag{2.41}$$

where $\theta_{i,i+j}$ is the angle between the vectors of the ith and $i+j$th hop. In the case of diffusion of a tracer atom through a lattice, if the tracer exchanges positions with a vacancy then the chance a the next hop being the reverse is higher than proceeding to a new site and the $\langle \cos\theta_{i,i+j} \rangle$ is necessarily non-zero and negative. The correlation factor is determined by the structure and the nature of the hopping event. A crude approximation for the correlation factor is:

$$f \approx 1 - \frac{2}{Z}, \tag{2.42}$$

where Z is the number of possible sites for an atom to jump to. The more possible sites, the lower the chance that the atom jumps back to where it started and the diffusion approaches a random walk. The agreement between this approximation and the exact values is usually within 10 %, but the agreement is greater for systems with smaller values of Z. The agreement between this rule of thumb and measured values is best for diffusion dominated by vacancy diffusion. For diffusion using divacancy or interstitial mechanisms the agreement is reduced.

2.3 The Green-Kubo Formalism

The Green-Kubo formalism is an alternative formulation for the self-diffusion coefficient. The Einstein-Sutherland relation and the Green-Kubo formalism are equivalent in theory with the Einstein-Sutherland relation centring around the mean-squared displacement and the Green-Kubo formalism centring on the velocity autocorrelation function (VACF). When used to measure transport coefficients in an equilibrium-molecular-dynamics simulation the Green-Kubo formalism relates the spontaneous fluctuations occurring at equilibrium to the dissipative transport coefficients. Consider the following:

$$\mathbf{r}_i(t) - \mathbf{r}_i(0) = \int_0^t \mathrm{d}s\, \mathbf{v}_i(s), \tag{2.43}$$

where $\mathbf{r}_i = x_i\hat{\mathbf{i}} + y_i\hat{\mathbf{j}} + z_i\hat{\mathbf{k}}$ is the three dimensional position vector of atom i and $\mathbf{v}_i$ is the velocity of atom i. The average squared displacement is defined microscopically for N atoms:

$$\left\langle r^2(t) \right\rangle = \frac{1}{N} \sum_{i=1}^{N} \left| \mathbf{r}_i(t) - \mathbf{r}_i(0) \right|^2 . \tag{2.44}$$

Using Eqn. 2.43 the average squared displacement becomes:

$$\left\langle r^2(t) \right\rangle = \left\langle \left(\int_0^t \mathrm{d}s\, \mathbf{v}(s) \right) \cdot \left(\int_0^t \mathrm{d}s'\, \mathbf{v}(s') \right) \right\rangle . \tag{2.45}$$

This product of integrals can be shown to be:

$$\int_0^t \mathrm{d}s \int_0^t \mathrm{d}s'\, \left\langle \mathbf{v}(s) \cdot \mathbf{v}(s') \right\rangle = \int_0^t \mathrm{d}s \int_0^s \mathrm{d}s'\, \left\langle \mathbf{v}(s) \cdot \mathbf{v}(s') \right\rangle + \int_0^t \mathrm{d}s \int_s^t \mathrm{d}s'\, \left\langle \mathbf{v}(s) \cdot \mathbf{v}(s') \right\rangle . \tag{2.46}$$

The integrands are the velocity autocorrelation functions and are equilibrium properties. This means the time-reversal, $f(u) = f(-u)$, and time-translational, $f(u) = f(t+u)$, symmetry properties can be used, hence:

$$u = t - s \rightarrow s = t - u,\ \mathrm{d}s = -\mathrm{d}u$$

$$u' = t - s' \rightarrow s' = t - u',\ \mathrm{d}s' = -\mathrm{d}u'$$

Using these substitutions the product of integrals (Eqn. 2.46) becomes:

$$\int_0^t \mathrm{d}s \int_0^t \mathrm{d}s'\ \langle \mathbf{v}(s)\cdot\mathbf{v}(s')\rangle = \int_t^0 \mathrm{d}u \int_t^{t-u} \mathrm{d}u'\ \langle \mathbf{v}(t-u)\cdot\mathbf{v}(t-u')\rangle + \int_t^0 \mathrm{d}u \int_{t-u}^0 \mathrm{d}u'\ \langle \mathbf{v}(t-u)\cdot\mathbf{v}(t-u')\rangle\,. \tag{2.47}$$

Applying the time-translational symmetry of equilibrium properties to Eqn. 2.47 leads to:

$$\left\langle r^2(t)\right\rangle = 2\int_0^t \mathrm{d}u \int_0^u \mathrm{d}u'\ \langle \mathbf{v}(u)\cdot\mathbf{v}(u')\rangle\,. \tag{2.48}$$

After a further substitution of $\tau = u' - u,\ \mathrm{d}u' = \mathrm{d}\tau$, the average mean squared displacement becomes:

$$\left\langle r^2(t)\right\rangle = 2\int_0^t \mathrm{d}u \int_0^u \mathrm{d}\tau\ \langle \mathbf{v}(0)\cdot\mathbf{v}(\tau)\rangle\,. \tag{2.49}$$

Substituting Eqn. 2.49 into the Einstein-Sutherland relation, Eqn. 2.30, gives:

$$\frac{\mathrm{d}\left\langle r^2(t)\right\rangle}{\mathrm{d}t} = 2dD = 2\int_0^t \mathrm{d}\tau\ \langle \mathbf{v}(0)\cdot\mathbf{v}(\tau)\rangle\,. \tag{2.50}$$

The Green-Kubo relation for the self-diffusion coefficient is therefore:

$$D = \frac{1}{d}\int_0^\infty \mathrm{d}\tau\ \langle \mathbf{v}(0)\cdot\mathbf{v}(\tau)\rangle\,. \tag{2.51}$$

This result will be used in a discussion of linear-response theory in Section 2.12.

2.4 The Arrhenius Model

There are two main approaches to investigating diffusion in solids. The first is transition-state theory (TST), which involves calculating all the variables in an Arrhenius model of diffusion for a known or hypothetical pathway. The second approach is to use molecular dynamics (MD) to simulate the collective motion of atoms. The resulting trajectories can then be analysed to give both the microscopic pathways of diffusion and, using the Einstein-Sutherland equation, the macroscopic diffusion coefficients. The diffusion is thus an emergent property of MD whereas TST requires the input of pre-selected pathways. This limits TST to systems where the diffusion is rather simple or can be easily anticipated. Diffusion pathways involving the movement of many atoms, often concerted, are very difficult to model using TST. However, the significant drawback to MD is that the simulation timescales accessible are much smaller than the timescales of diffusion in solids. In reality, given current computational resources, this limits MD to studying diffusion in liquids or very high-temperature superionic solids.

As mentioned in Section 1.1 the diffusion coefficients vary with temperature and this can be usually be described with the Arrhenius equation:

$$D = D_0 \exp\left(\frac{-\triangle H}{k_B T}\right), \tag{2.52}$$

where k_B is the Boltzmann constant, T is the temperature, $\triangle H$ is the activation enthalpy of the diffusion process, and D_0 is a pre-exponential factor. Typically the temperature dependence of diffusion is represented by an Arrhenius plot of $\ln D$ against $1/T$, the gradient of which is the activation of energy and the y-axis intercept D_0. The pre-exponential frequency factor can usually be written as:

$$D_0 = f v_0 a^2 \exp\left(\frac{\triangle S}{k_B}\right), \tag{2.53}$$

where f is the correlation factor, v_0 is the attempt frequency, a is the lattice parameter, and $\triangle S$ is the diffusion entropy. The attempt frequency can usually be replaced with the Debye frequency. The correlation factors is as described in Section 2.2. Hence, the diffusion coefficient can be written as:

$$D = f v_0 a^2 \exp\left(-\frac{\triangle G}{k_B}\right), \tag{2.54}$$

where $\triangle G$, the Gibbs free energy of activation, is:

$$\triangle G = \triangle H - T\triangle S. \tag{2.55}$$

Eqn. 2.52 provides a simple relation for the temperature dependence of the diffusion coefficient, but often it is insufficient. Problems arise from multiple mechanisms, which will most likely have different activation energies and different pre-exponential factors. The multiplicity of mechanisms can arise from the presence of impurities, grain boundaries and other microstructure faults. In the presence of multiple diffusion pathways Eqn. 2.52 can be rewritten as:

$$D = \sum_i D_{0,i} \exp\left(\frac{-\triangle H_i}{k_B T}\right), \tag{2.56}$$

where the index i indicates the different diffusion pathways.

2.5 The Nernst-Einstein Relation

The Nernst-Einstein relation, as mentioned in Section 1.1, links the conductivity with the diffusion coefficient. The electrical conductivity in an ionic solid is usually associated with the motion of ions, rather than electrons. The motion of the ions experiencing an electric field is the ionic conductivity. The equation describing the total flux of ions consists of two parts, Fick's first law (Eqn. 2.1) for diffusion and a second term for the action of an applied electric field that serves as a driving force:

$$j = -D\frac{\partial C}{\partial x} + \bar{v}C, \tag{2.57}$$

where $\bar{v}$ is the drift velocity of the ions experiencing the driving force F. The second term, consisting of the drift velocity and the concentration, C, is a drift term and is proportional to the potential gradient. If a system has one mobile species with a diffusion flux equal but opposite to the flux due to the driving force, then the balancing of fluxes leads to a steady-state and then the total flux (Eqn. 2.57) becomes:

$$0 = -\tilde{D}\frac{\partial C}{\partial x} + \bar{v}C, \tag{2.58}$$

where $\tilde{D}$ is the chemical-composition diffusion coefficient. The solution of Eqn. 2.58 can be (Mehrer, 2007) shown to be:

$$C = C_0 \exp\left(-\frac{\bar{v}}{\tilde{D}}x\right), \tag{2.59}$$

where C_0 is the concentration at $x = 0$. The external force, F, can be written as the derivative of a potential, U:

$$F = -\frac{\partial U}{\partial x}. \tag{2.60}$$

Given the system is a steady-state and at thermodynamic equilibrium the distribution can be described by a Boltzmann distribution:

$$C = \alpha \exp\left(-\frac{U}{k_B T}\right), \tag{2.61}$$

with α being a pre-exponential constant. Differentiating Eqn. 2.61 with respect to time gives:

$$\frac{\partial C}{\partial x} = -\frac{C}{k_B T}\frac{\partial U}{\partial x}. \tag{2.62}$$

Substituting the force, Eqn. 2.60, into Eqn. 2.62 yields:

$$\frac{\partial C}{\partial x} = \frac{CF}{k_B T}. \tag{2.63}$$

Using this, Eqn. 2.58 can be rewritten as:

$$\tilde{D} = \frac{\bar{v}k_B T}{F}. \tag{2.64}$$

This is the general form of the Nernst-Einstein relation. It is often written in the form:

$$\tilde{D} = uk_B T, \tag{2.65}$$

where u is the mobility and is defined as the ratio of the drift velocity to the external force. The

Nersnt-Einstein relation is general with respect to the external force applied to the system. In the specific case of an electric field E the force is:

$$F = qE, \tag{2.66}$$

where q is the charge on the mobile ion. The flux, j, arising from the mobile ions in the electric field is:

$$j = \bar{v}C. \tag{2.67}$$

Using the Nernst-Einstein relation (Eqn. 2.64) to substitute for the drift velocity and the definition of the external force in Eqn. 2.66 the flux becomes:

$$j = \frac{qC\tilde{D}}{k_B T}E. \tag{2.68}$$

Ohm's law defines the electrical current density, $\mathbf{j}_e$, in terms of the dc conductivity, σ_{dc}, and the electric field, $\mathbf{E}$:

$$\mathbf{j}_e = \sigma_{dc}\mathbf{E}. \tag{2.69}$$

The one-dimensional electrical current density can also be defined by the parallel flux:

$$j_e = jq. \tag{2.70}$$

Using Ohm's law (Eqn. 2.69) the dc conductivity can be written as:

$$\sigma_{dc} = \frac{q^2 C\tilde{D}}{k_B T}. \tag{2.71}$$

This can be extended for a system of interacting particles (Murch, 2001) to:

$$\sigma_{dc} = \frac{q^2 C\tilde{D}}{k_B T}\left(\frac{\partial \ln N}{\partial \mu}\right), \tag{2.72}$$

where μ is the chemical potential and N is the site occupancy. If the composition is ideal and there are no site-blocking effects the term in brackets becomes unity and therefore the chemical-

composition diffusion coefficient equals the tracer diffusion coefficient, D^*:

$$\sigma_{dc} = \frac{q^2 C D^*}{k_B T}, \tag{2.73}$$

where:

$$D^* = \bar{D}\left(\frac{\partial \ln N}{\partial \mu}\right). \tag{2.74}$$

Where there are site blocking effects the tracer correlation factor, f, is introduced:

$$\sigma_{dc} = \frac{q^2 C D^*}{f k_B T}. \tag{2.75}$$

This holds for ionic crystals where there is a near-perfect lattice.

2.6 The Determination of Diffusion Coefficients: Experimental and Computational Methods

There is a very wide range of techniques for determining the diffusion coefficients of a given system, both experimental and computational. Often these different methods can lead to surprisingly different values of the diffusion coefficient. The available experimental methods can be divided into two groups: direct and indirect methods. Direct methods are based upon Fick's definition of diffusion (Eqn. 2.1). They consider long-range diffusion and are a measure of the macroscopic displacement of ions. The radio-tracer method is the most common technique for measuring the self-diffusion coefficient and is classified as a direct method. It requires suitable isotopes of the mobile ions to be available. Indirect methods do not measure diffusion as defined by Fick's law, but measure phenomena that are correlated to the diffusion of mobile ions. Indirect methods involve measuring quantities such as relaxation times, relaxation rates, and line-widths that can then be used to calculate the average residence times of diffusing ions. The average residence time can then be used to form a microscopic model of the diffusion for individual hops. The diffusion coefficient can then be determined from this microscopic model of diffusion using the Einstein-Smoluchowski relation:

$$D_E = \frac{a^2}{6\bar{\tau}}, \tag{2.76}$$

where D_E is the uncorrelated diffusion coefficient, a is the length of the ion hop, and $\bar{\tau}$ is the mean residence time. Limitations of NMR or impedance spectroscopy (IS) methods, where an external field of a certain frequency is applied, become apparent when the frequency of the applied field and that of the hopping events are too dissimilar. This limits methods to working in a specific range of values of the self-diffusion coefficients, Fig. 2.1. Usually NMR methods are indirect methods, but both static-field-gradient and pulse-field-gradient NMR allow direct diffusivity measurements without the need for a microscopic model. Indirect NMR methods are among the most popular for studying diffusion and cover a wide range of diffusivity values. IS measures the conductivity of ion-conducting materials, σ_{dc}, which can be converted to a diffusion coefficient, D_σ using the Nernst-Einstein equation:

$$\sigma_{dc} = \frac{(Ze)^2 \rho_c}{k_B T} D_\sigma, \tag{2.77}$$

where Z is the charge of the conducting ion and ρ_c the density of charged particles. Impedance spectroscopy can be applied to ion-conducting materials with negligible electronic conductivity, where the conduction is a result of hopping of ions.

Computational methods used to model the diffusion of solid state materials fall into two broad categories: transition-state theory based descriptions of known or hypothetical diffusion pathways and molecular dynamics (MD) yielding atom trajectories. MD simulates the trajectories of all the individual atoms in the system using the classical equations of motion. The interatomic forces must be known and are usually determined from a pairwise force-field method or an electronic-structure method such as density functional theory (DFT). The individual atom trajectories can be analysed to elucidate the specific diffusion pathways and the overall displacement of atoms can be used to determine the self-diffusion coefficients using the Einstein-Sutherland relation (Eqn. 2.30). Diffusion is an emergent property of MD simulations as with the input of only structure and interatomic interactions the atoms thermally diffuse throughout the structure. MD does not require any prior knowledge of diffusion pathways or mechanisms. *Ab initio* methods involve calculating all the variables of an Arrhenius model for a given diffusion pathway. This limits the scope of *ab initio* methods, especially when considering diffusion mechanisms that involve the collective movement of many particles, often in concert, whereas MD methods intrinsically takes account for mass particles effects. MD methods have the potential to give a greater insight into the microscopic diffusion

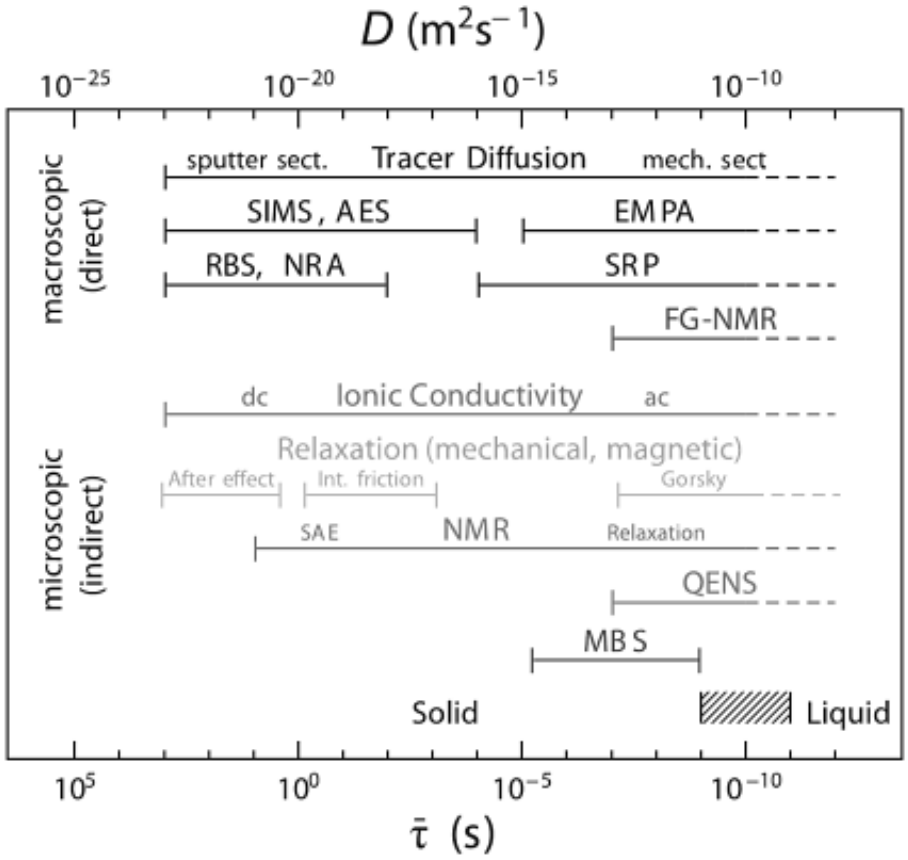


Figure 2.1: Typical ranges of the self-diffusion coefficient (D) and mean residence time ($\bar{\tau}$) accessible via different experimental techniques. The mean residence time is calculated from Eqn. 2.76 assuming a hop length of $\sim 2.5\,\text{Å}$. Taken from Mehrer (2007).

mechanisms operating and the macroscopic measurement of diffusion. In this way MD acts as bridge between direct and indirect experimental methods by giving both the total movement of atoms as would be measured in a radio-tracer method and also giving values for microscopic properties such as mean residence times and hopping rates as measured in NMR experiments.

2.7 Density Functional Theory

Density functional theory (DFT) is an *ab initio* method widely used for the modelling of solid-state materials. DFT is commonly used in a range of fields and studies; especially for solid-state structural studies. For *ab initio* methods the wavefunction is the central quantity and once known, or at least an acceptable approximation has been found, all properties of the system can be determined. However,

even an approximate wavefunction is computationally inaccessible for large systems. DFT relies on the fundamental tenet that any property can be described as a functional of the ground-state electron density. DFT uses the ground-state electron density as the central quantity. The all-electron wavefunction depends on $4N$ (where N is the number of atoms) degrees of freedom, three spatial and one spin, whereas the electron density only depends on three spatial degrees of freedom and not on the number of atoms present.

The implementation of DFT outlined above is not, however, the first attempt to use the electron density as the central quantity. In 1927 the Thomas-Fermi model was the first model to describe fully the energy of an atom in terms of electron density. The model has many drawbacks including treating nuclear-electron and electron-electron interactions in a classical manner and only the kinetic energy in terms of electron density. These limitations lead to a significant degree of inaccuracy. The Slater approximation of 1952 replaced the non-local exchange term of Hartree-Fock theory with a local expression depending only on the electron density. A brief summary of DFT is given below. More thorough descriptions can be found in many text books including Parr and Yang (1989), Martin (2008), Sholl and Steckel (2009) and Koch and Holthausen (2001).

2.7.1 The Hohenberg-Kohn Theorems

The theory behind DFT as we use it today relies on the Hohenberg-Kohn theorems and the Kohn-Sham approach. The 1964 landmark paper by Hohenberg and Kohn (1964) proved that when electron density is used as the central quantity, the subsequent model contains all the information to describe a system fully.

The first Hohenberg-Kohn theorem is the proof of existence:

'the external potential $V_{ext}(\mathbf{r})$ is (to within a constant) a unique functional of $\rho(\mathbf{r})$; since, in turn $V_{ext}(\mathbf{r})$ fixes $\hat{\mathrm{H}}$ we see that the full many particle ground state is a unique functional of $n(\mathbf{r})$'

The proof starts by considering two different external potentials $V_{ext}^{(1)}(\mathbf{r})$ and $V_{ext}^{(2)}(\mathbf{r})$ that differ by more than a constant, but give the same electron-density ground state $n(\mathbf{r})$. The different external potentials yield two different Hamiltonians, $\hat{H^{(1)}}$ and $\hat{H^{(2)}}$. Given the two different Hamiltonians, there are two different ground-state, all-electron wavefunctions, $\Psi^{(1)}$ and $\Psi^{(2)}$, respectively. If the two ground states are non-degenerate then:

$$E^{(1)} = \left\langle \Psi^{(1)} | \hat{H^{(1)}} | \Psi^{(1)} \right\rangle < \left\langle \Psi^{(2)} | \hat{H^{(1)}} | \Psi^{(2)} \right\rangle. \tag{2.78}$$

The final term in Eqn. 2.78 can be written as:

$$\left\langle \Psi^{(2)} | \hat{H^{(1)}} | \Psi^{(2)} \right\rangle = \left\langle \Psi^{(2)} | \hat{H^{(2)}} | \Psi^{(2)} \right\rangle + \left\langle \Psi^{(2)} | \hat{H^{(1)}} - \hat{H^{(2)}} | \Psi^{(2)} \right\rangle, \tag{2.79}$$

$$= E^{(2)} + \int d^3r \, [V_{ext}^{(1)}(\mathbf{r}) - V_{ext}^{(2)}(\mathbf{r})] n_0(\mathbf{r}). \tag{2.80}$$

Then Eqn. 2.78 can be written as:

$$E^{(1)} < E^{(2)} + \int d^3r \, [V_{ext}^{(1)}(\mathbf{r}) - V_{ext}^{(2)}(\mathbf{r})] n_0(\mathbf{r}). \tag{2.81}$$

If we were to start by considering $E^{(2)}$ instead of $E^{(1)}$ then it follows that:

$$E^{(2)} < E^{(1)} + \int d^3r \, [V_{ext}^{(2)}(\mathbf{r}) - V_{ext}^{(1)}(\mathbf{r})] n_0(\mathbf{r}). \tag{2.82}$$

If Eqn. 2.81 and Eqn. 2.82 are added, then the resulting inequality is:

$$E^{(1)} + E^{(2)} < E^{(1)} + E^{(2)}. \tag{2.83}$$

This is clearly contradictory, but establishes that two different external potentials cannot give rise to the same non-degenerate ground-state electron density. The electron density is unique to the external potential to within a constant. This result means that the ground-state electron density is all that is needed to describe fully all the properties of the system. When applied to electrons in atoms, molecules, and materials, the external potential is usually only defined by the Coulombic potential due to the position of the nuclei. This does not help solve anything, but proves that the electron density can be the sole central quantity for modelling such systems. The first Hohenberg-Kohn theorem assumes non-degenerate ground states, but it can be extended to include degenerate ground states using the alternative formulation by Levy (Levy, 1979, 1982).

The second Hohenberg-Kohn theorem is the variational principle. The variational principle states that for a given external potential the global minimum value of the energy functional is the exact ground-state energy of the system and that the electron density that minimizes the energy functional

is the ground-state electron density. Essentially the energy functional will deliver the lowest energy only if the input density is the ground-state density. From the first Hohenberg-Kohn theorem all properties are derived from the $n(\mathbf{r})$ of the system. The total energy, and its components, can be described as functionals of the electron density:

$$E[n] = T[n] + E_{int}[n] + \int d^3r\, V_{ext}(\mathbf{r})n(\mathbf{r}) + E_{II}, \tag{2.84}$$

where $T[n]$ is the kinetic energy, $E_{int}[n]$ is the interaction between the electrons, the term containing $V_{ext}(\mathbf{r})$ describes the interactions between the electron density and the nuclei, and E_{II} is the interaction energy between the nuclei. The first two terms are universal, meaning they are the same for all electron systems, as all internal, kinetic and potential energies are only dependent on the interacting electron system. They are not dependent on the external potential.

It follows from the first Hohenberg-Kohn theorem that:

$$E_0^{(1)} = E^{(1)}[n_0] = \frac{\left\langle \Psi_0^{(1)} | \hat{H^{(1)}} | \Psi_0^{(1)} \right\rangle}{\left\langle \Psi_0^{(1)} | \Psi_0^{(1)} \right\rangle}. \tag{2.85}$$

If the ground state wavefunction from another external potential is substituted into Eqn. 2.85, then the energy would not be the ground state energy:

$$E^{(2)} = E[n_0^{(2)}] = \frac{\left\langle \Psi_0^{(2)} | \hat{H^{(1)}} | \Psi_0^{(2)} \right\rangle}{\left\langle \Psi_0^{(2)} | \Psi_0^{(2)} \right\rangle} > \frac{\left\langle \Psi_0^{(1)} | \hat{H^{(1)}} | \Psi_0^{(1)} \right\rangle}{\left\langle \Psi_0^{(1)} | \Psi_0^{(1)} \right\rangle} = E[n_0^{(1)}]. \tag{2.86}$$

The ground-state electron density determines the external potential. The external potential determines the Hamiltonian, which determines the ground-state wavefunction. The inequality of Eqn. 2.86 follows from the variational principle. If the form of the functionals $T[n]$ and $E_{int}[n]$ are known, then minimizing the total energy with respect to the electron density allows the ground-state electron density and ground-state energy to be determined. This does not give any information regarding the excited states, and this is why DFT is generally a ground-state-only model. Unfortunately, as will become apparent later, the form of the functionals $T[n]$ and $E_{int}[n]$ is not known and therefore the variational principle is not applicable.

An alternative formulation proposed by Levy and Lieb is the constrained-search approach (Levy, 1979, 1982; Lieb, 2002). It searches over all allowed wavefunctions and the wavefunction having the

lowest energy is the ground-state wavefunction. The search is a two-step process: a search over all allowed wavefunctions to find the lowest energy is followed by a second search over all densities to give the ground-state electron density. This removes the condition of non-degenerate states for the Hohenberg-Kohn proof of existence. The main drawback of the constrained search method is the time needed to search over all possible wavefunctions. The constrained search method is only of theoretical value and does not help to solve the problem.

The Hohenberg-Kohn theorems and the Levy and Lieb formulations provide the theoretical proof that using the electron density, instead of the wavefunction, is valid as a way to describe the ground state of the system. The Hohenberg-Kohn theorems do not provide a solution to the problem of finding the ground state, but they do validate the idea of DFT and help in the search for a solution. In order to find a solution we need the approach developed by Kohn and Sham.

2.7.2 The Kohn-Sham Approach

The proliferation of density-functional theory is due to the Kohn-Sham approach (Kohn and Sham, 1965). Introduced in 1965 the Kohn-Sham approach starts by considering a hypothetical system in which the electrons do not interact. The electron density of the non-interacting system is by definition the same as the fully (non-hypothetical) interacting system. One of the main advantages of the Kohn-Sham approach is the ability to model a large fraction of the total energy very efficiently, which vastly improves the efficacy of computational calculations. Then the remaining, less-accessible components of the total energy are neatly placed in a functional. Although the form of the functional is unknown, even a crude approximation can yield very accurate calculations.

One assumption of the Kohn-Sham approach is that the ground-state electron density of the real system is equal to that of the non-interacting system. The electrons in the non-interacting system are described by independent-particle equations. These independent-particle Kohn-Sham equations can readily be solved numerically; the solutions are called the Kohn-Sham orbitals. When these are solved, the ground-state electron density and energy are known to within the accuracy of the approximations of the exchange-correlation functional.

The electron density, $n(\mathbf{r})$, expressed as the sum of the Kohn-Sham orbitals, $\psi_i(\mathbf{r})$, is:

$$n(\mathbf{r}) = \sum_{i=1}^{N} |\psi_i(\mathbf{r})|^2, \tag{2.87}$$

for an N electron system. The kinetic energy, T_{KS}, for the non-interacting system is described by:

$$T_{KS} = -\frac{1}{2}\sum_{i=1}^{N} \langle \psi_i | \nabla^2 | \psi_i \rangle . \tag{2.88}$$

The kinetic energy uses the Kohn-Sham orbitals (i.e. wavefunctions) as it can not be done accurately using the electron density. The Hartree energy, $E_{ee}[n]$, the energy arising, from the classical Coulombic interaction of the electron density with itself is:

$$E_{ee}[n] = \frac{1}{2}\int \mathrm{d}^3 r \mathrm{d}^3 r' \frac{n(\mathbf{r})n(\mathbf{r}')}{|\mathbf{r}-\mathbf{r}'|}. \tag{2.89}$$

Using these definitions the Hohenberg-Kohn expression (Eqn. 2.84) for the ground-state energy becomes:

$$E_{KS} = T_s[n] + \int \mathrm{d}\mathbf{r}\, V_{ext}(\mathbf{r})n(\mathbf{r}) + E_{ee}[n] + E_{II} + E_{XC}[n]. \tag{2.90}$$

The terms for electron-nuclei, electron-electron, and nuclei-nuclei Coulombic interactions are well defined and can be solved readily. The kinetic energy of the non-interacting system is a functional of the Kohn-Sham orbitals. The other contributions to the total energy, namely the difference in kinetic energy between the interacting and non-interacting systems and the non-Coulombic electron-electron interactions, are many-body effects. These many-body effects are grouped together to form the exchange-correlation functional $E_{XC}[n]$.

The non-interacting system is solved using the variational principle. Solving the Kohn-Sham non-interacting system requires minimization with respect to the Kohn-Sham orbitals or the external potential. Using the chain rule it can be shown to be:

$$\frac{\partial E_{KS}}{\partial \psi_i(\mathbf{r})} = \frac{\partial T_S}{\partial \psi_i(\mathbf{r})} + \left[\frac{\partial E_{ext}}{\partial n(\mathbf{r})} + \frac{\partial E_{ee}}{\partial n(\mathbf{r})} + \frac{\partial E_{XC}}{\partial n(\mathbf{r})}\right]\frac{\partial n(\mathbf{r})}{\partial \psi_i(\mathbf{r})} = 0. \tag{2.91}$$

Using the definitions from Eqn. 2.87 and 2.88, Eqn. 2.91 becomes:

$$\frac{\partial E_{KS}}{\partial \psi_i(\mathbf{r})} = -\frac{1}{2}\nabla^2\psi_i(\mathbf{r}) + \left[\frac{\partial E_{ext}}{\partial n(\mathbf{r})} + \frac{\partial E_{ee}}{\partial n(\mathbf{r})} + \frac{\partial E_{XC}}{\partial n(\mathbf{r})}\right]\psi_i(\mathbf{r}) = 0. \tag{2.92}$$

If the Lagrange multiplier method is used the resulting Hamiltonian for the non-interacting

system is:

$$H_{KS}(\mathbf{r}) = -\frac{1}{2}\nabla^2 + V_{KS}(\mathbf{r}), \tag{2.93}$$

where $V_{KS}(\mathbf{r})$ can be written as:

$$V_{KS}(\mathbf{r}) = V_{ext}(\mathbf{r}) + \frac{\partial E_{ee}}{\partial n(\mathbf{r})} + \frac{\partial E_{XC}}{\partial n(\mathbf{r})}, \tag{2.94}$$

which can then be written as:

$$V_{KS}(\mathbf{r}) = V_{ext}(\mathbf{r}) + V_{ee}(\mathbf{r}) + V_{XC}(\mathbf{r}). \tag{2.95}$$

The Eqns. 2.93 and 2.95 are the Kohn-Sham equations, which have the form of independent-particle equations. The eigenvalues, ε_i, of the Kohn-Sham equations are given by:

$$H_{KS}\psi_i(\mathbf{r}) = \varepsilon_i\psi_i(\mathbf{r}). \tag{2.96}$$

The equations presented neglect the spin of electrons, but can be easily extended to account for spin. The independent-particle equations with an effective potential must be solved self-consistently. The Kohn-Sham equations are independent of the approximations of $E_{XC}[n]$ and would yield the exact ground-state electron density, and the corresponding energy, if the exact form of the exchange-correlation functional were known. About 90% of the total energy of a system can be recovered from the Hartree energy, the non-interacting system kinetic energy, and nuclei-electron interactions. Only a small amount of the total energy is dependent on the exchange-correlation terms, so any reasonable approximation should yield a good total energy. Unfortunately, when it comes to chemistry, the total energy is rather meaningless; energy differences are the key parameters. The energy differences for different chemical environments are often small and due to subtle changes in correlation and exchange effects.

The interactions that dominate the kinetic energy and the Hartree energy are significant over a longer range than those parceled into the exchange-correlation functional. This makes the exchange-correlation functional rather local, and therefore approximations need only be local or semi-local in nature.

2.7.3 Exchange-correlation Functionals

$$E_{XC}[n] = T[n] - T_{KS}[n] + E_{ee}[n] - E_j[n]. \tag{2.97}$$

The exchange-correlation functional contains the relatively inaccessible contributions to the total energy. If the full analytical form of the exchange-correlation functional were known, DFT would produce the exact electron density and consequently the exact ground state of a many-body problem. However, even with very crude approximations of this functional, DFT can produce very good results. The $T[n] - T_{KS}[n]$ difference is the necessary correction to the total kinetic energy, required because the Kohn-Sham approach only calculates the kinetic energy of a non-interacting system. The $E_{ee}[n] - E_j[n]$ is the difference between the internal interaction energies of the real interacting system and the fictitious Kohn-Sham non-interacting system. Unfortunately, differences in the kinetic energy and internal interactions of a few electrons can often define the chemistry of a system, so small inaccuracies in the exchange-correlation functional can yield misleading results.

$$E_{XC}[n] = \int d\mathbf{r} n(\mathbf{r}) V_{XC}(\mathbf{r}; n). \tag{2.98}$$

By creating the fictitious non-interacting system then correcting for the difference, the functional can be approximated with a local or semi-local functional of the density. The first approximation for the exchange-correlation functional was the local density approximation (LDA) in which the system is modelled as an uniform homogenous gas; the exchange-correlation energy then only depends on the value of the electron density (Eqn. 2.98). Only the exchange energy and the correlation energy need be known. The exchange energy of a homogenous system is known analytically (Slater, 1951) and the correlation energy can be calculated, with great accuracy, using Monte Carlo methods (Ceperley and Alder, 1980). The resulting values have been fitted to different analytical forms by a variety of groups leading to a number of nearly identical LDA parameterisations. LDA can provide very good results for certain systems, but does tend to overestimate bond-strength values. LDA typically works best for solids that resemble the uniform gas and, unsurprisingly, worst for systems with very variable electron densities such as molecular and atomic systems.

The generalized-gradient approximation (GGA) is the first step beyond LDA and increases the accuracy of DFT calculations to the point where the modelling of chemical systems becomes viable. The GGA considers not only the density value at a point in space, but also the gradient of the

density (Herman et al., 1969). Kohn and Sham (1965) suggested using the gradient of the density to extend LDA, but this approach breaks the sum rule and leads to unsatisfactory results. The form of the GGA as commonly used, which obeys the sum rule, was introduced by Perdew and Wang (1992).

2.7.4 Bloch's Theorem

Instead of solving the electron density for a system with an infinite number of electrons one must look to reduce the size of the system somewhat. If a system consists of an infinite 3D array of periodic cells (unit cells), which is the case for crystalline solids and is a good approximation for liquids as well, then Bloch's theorem can be used to reduce the size of the calculation. A corollary of Bloch's theorem states that the wavefunction of a periodic system can be separated into two parts: one for the wavefunction of the periodic unit and a phase component:

$$\psi_{\mathbf{j},\mathbf{k}}(\mathbf{r}) = u_{\mathbf{j}}(\mathbf{r})e^{i\mathbf{k}\cdot\mathbf{r}}, \tag{2.99}$$

where $u_{\mathbf{j}}(\mathbf{r})$ has the same periodicity as the external potential (and lattice), so $u_{\mathbf{j}}(\mathbf{r}+\mathbf{l}) = u_{\mathbf{j}}(\mathbf{r})$ where $\mathbf{l}$ are the lattice vectors of the periodic unit. The exponential term, $e^{i\mathbf{k}\cdot\mathbf{r}}$, uses the vector $\mathbf{k}$ that is confined to the first Brillouin Zone. This allows the problem to be separated into the wavefunction of a single unit cell, $u_{\mathbf{j}}(\mathbf{r})$, and an infinite integral over $\mathbf{k}$ that can be replaced with a discrete approximation. With each electron occupying a specific $\mathbf{k}$ state an infinite number of electron leads to an infinite number of k-points. For each k-point only a finite number of the available energy levels will be occupied. This allows the problem of an infinite number of electrons to be replaced by a problem of a finite number of electrons at an infinite number of k-points. The infinite number of k-points can be easily replaced with a finite grid of k-points with a density that can be determined.

Bloch's theorem applies to any periodic system. However for molecular dynamics and defect calculations the size of the periodic unit must be chosen in order to account for the self-interactions i.e. in the case of diffusion, the mobile ions pushing and pulling themselves along. This cell - called a supercell - is typically significantly larger than the crystallographic unit cell.

2.7.5 Basis Sets

Using Bloch's theorem for a periodic system, the wavefunction at a given k-point can be expanded by a discrete plane-waves basis set. In theory this requires an infinite basis set, but the contributions from plane waves with small kinetic energies are much greater than the contribution from high kinetic energies. This allows for a cutoff energy to be used to limit the size of the plane-wave basis set.

There are other choices of basis sets that can be used instead of plane waves. In this thesis a dual-basis set is used to describe the electrons in the DFT calculations presented. The basis set must be complete and orthogonal. VandeVondele et al. (2005) introduced a dual-basis set combining atom-centred Gaussian functions and plane waves. This method allows for very efficient calculations. The plane wave expansion coefficients are given by the Fourier transform of the density expressed in the Gaussian basis set. When the total energy functional is evaluated the Gaussian representative is used to evaluate the kinetic energy and the interaction energy with the external potential and the plane wave representation is used to calculate the electron-electron interaction energy.

2.7.6 Pseudopotentials

The significant rise in the use of DFT for studying the solid state can largely be attributed to the successful application of pseudopotentials. Pseudopotentials provide a simple but accurate model for the core electrons. The use of pseudopotentials removes the need to model the core electrons using the computationally-expensive plane-wave basis set and allows the plane-wave basis set to be limited to the valence electrons, which are of chemical interest. If the tightly-bound core electrons were to be described using plane waves they would have to be of very high frequency. By using pseudopotentials the size of the plane-waves basis set can be reduced significantly. The highest frequency, or energy, plane wave required to model accurately the valence electrons depends on the choice of pseudopotential, and is usually referred to as the cut-off energy. Pseudopotentials are calculated typically for a single atom then, if formed correctly, are transferable to other environments such as molecules and condensed matter because the core electrons are typically not affected by the change in chemical environment. Replacing the core electrons with a pseudopotential assumes the core electrons are of high enough energy not to effect the chemical environment.

There are many choices for pseudopotentials and reviewing such a vast field is beyond the scope

of this thesis (Pickett, 1989; Singh and Nordstram, 2006). Ultrasoft pseudopotentials are used in this thesis, as they are the most efficient for plane-wave calculations. Their efficiency derives from separating the problem into two functions: a smooth function and an auxiliary function (Blöchl, 1990; Vanderbilt, 1990).

2.7.7 Mulliken Population Analysis

Population analysis is a mathematical method for partitioning the non-local electron density, or wave function, into partial charges on each individual atom. The population analysis gives the nature of the electronic charge distribution in terms of atom localized partial charges and orbital occupancies, as well as the nature and order of bonding or anti-bonding. The partial charge on an atom cannot be determined experimentally because it does not relate to a measurable physical property. More fundamentally, it is not an observable and could never be measured, even in principle. In the solid-state the nuclei are situated in a cloud of varying electron density and the partial charges are determined by the charge of the nuclei and the chance of finding an electron near to the nucleus. The magnitude of individual partial charges is not of significant meaning and is largely dependent on the basis set used (Davidson and Chakravorty, 1992), but the relative values can provide useful insight. The Mulliken population analysis (Mulliken, 1955) is the most ubiquitous population analysis used. An assumption of the Mulliken population analysis is that, where two orbitals overlap, the electron density is equally split between the two orbitals. This can lead to an underestimation of partial charges in ionic systems. The efficacy of a population analysis is measured by the spilling parameter (Segall et al., 1996a,b), which should be less than a few percent.

2.8 Force-Field

Ab initio methods can give a very accurate and precise model of a system, but at significant computational cost. In molecular-dynamic simulations, where the interatomic forces need to be calculated many times, the computational cost of *ab initio* methods can be prohibitive. This limits the size of the system that can be analysed using DFT or similar methods for determining the interatomic forces. These limitations often put the *ab initio* MD modelling of diffusion and related properties out of reach for many solid-state systems, especially at lower temperatures and for non-superionic conductivity. The use of classical methods can dramatically reduce the computational burden of such calculations; instead of pushing the best available supercomputers to their limits, classical

simulations using force fields can be performed on a laptop. However the use of classical methods is only possible when the interatomic forces calculated by *ab initio* methods can be reproduced to within an acceptable tolerance. The use of classical or empirical models has been used to study complex systems in proteins, molecular and solid systems with very good results (A. D. MacKerell et al., 1998; Islam et al., 2005; Ivanov-Shitz, 2007; Rotenberg et al., 2010; Marrocchelli et al., 2011; Panchmatia et al., 2011; Burbano et al., 2012). Force field models have been used with MD for a long time (Taylor et al., 1981) for studying diffusion in solids. Li_3N was studied using FF-MD in the 80s by Wolf et al. and despite the much more limited computational resources available at such time they managed to gain some insight into the diffusion and dynamical properties of Li_3N. Classical models have been used in a large number of studies into the dynamical properties of systems.

Given the systems studied in this thesis, pair-potentials are used to calculate the interatomic forces. This assumes the interaction energy, $V(\mathbf{r}^N)$, between N atoms is the sum of independent two-body interactions:

$$V(\mathbf{r}^N) = \sum_{i=1}^{N-1} \sum_{j=i+1}^{N} V(\mathbf{r}_{ij}) \tag{2.100}$$

where $\mathbf{r}_{ij}$ is the vector between species i and j, and $\mathbf{r}^N$ is the set of position vectors for all species present. The pair potential defines the potential energy between two atoms with a series of terms dependent on the interatomic distance. The various terms account for different interactions e.g. Coulombic, dispersion, dipole. Potentials can be formed for either soft or hard sphere systems. In this thesis we are only concerned with soft-sphere models. The number of terms added depends on the system being studied. The potential is then parametrized by determining coefficients for the individual terms that best fit experimental or *ab initio* data such as bond energies or structural distances. The parametrization of potentials is beyond the scope of this thesis. All parameters used in this thesis are taken from the literature.

The Coulombic interaction between charged species is a long-range interaction and straight forward to model. There are, however, shorter-range interactions present in chemical systems. These can have both repulsive and attractive contributions to the total energy. The overlap of electron clouds gives rise to a very short-range repulsive interaction. Beyond these repulsive interactions there are van der Waals, or London, interactions arising from the instantaneous formation of dipoles on both of the species. The London forces vary by r_{ij}^{-6} over distance, but are strongly dependent

on the characteristics of the particular ions. Initial attempts to account for short-range interactions using a pair-potential were made by Born and Lande (1918). This was later improved upon by Born and Mayer (1932). The Lennard-Jones (1924) potential was the first to include a term for the van der Waals interactions. The potential used for both the Li_3N and Li_2O studies is the Buckingham (1938) potential:

$$V(r) = \frac{q_1 q_2}{r} + A \exp\left(\frac{-r}{\rho}\right) - \frac{C}{r^6}, \tag{2.101}$$

where r is the separation of the two ions in question, q_i is the charge of species i, and A, ρ and C are constants. The first term describes the Coloumbic interactions between two particles, the second term accounts for the repulsion energy as formulated by Born and Mayer, and the last term models the Van der Waals interactions from Lennard-Jones. There is a cut-off used for the short range terms of the potential, typically 12 Å, after which the contributions from the short-range terms are negligible. Using FF or DFT the potential, and therefore forces, acting upon an individual atom can be calculated merely from the instantaneous positions and chemical identity. This allows the positions and velocities of the individual atoms to be calculated as a function of time using molecular dynamics. This is achieved using the classical equations of motion that are outlined Section 2.10.1.

2.9 Statistical Mechanics

The essential results of classical statistical mechanics are summarized below in preparation for subsequent discussions of equilibrium and non-equilibrium molecular dynamics. A thorough description of statistical mechanics is found in Hill (1986) and Tolman (1938). The computational methods used in this thesis involve modeling systems on the atomic level with hundreds of atoms present. This gives us a microscopic description of the system. Statistical mechanics connects this microscopic model with the macroscopic laws of classical thermodynamics. This allows the calculation of macroscopic properties, often in a form that can be compared with experimental results, from the atomic level.

The principles of classical statistical mechanics are similar to statistical mechanics for quantum systems, but there are some differences. The energy of quantum systems is quantized into discrete levels, but for classical systems it is continuous. The state of a classical system is defined by the positions and momenta, or velocities, of all atoms, not by the quantum state. The state of the classical system is described by $\mathbf{\Gamma} \equiv (\mathbf{p}, \mathbf{q})$, where $\mathbf{p}$ are the momenta and $\mathbf{q}$ are the positions.

The $6N$ dimensions of the positions and momenta is called the phase space. The state of a classical system is defined by one point in the $\mathbf{\Gamma}$ phase space. For a given quantum state there is an associated probability of occupation. For a classical system this is replaced for the canonical ensemble by a probability density function:

$$f_{NVT}(\mathbf{\Gamma}) = \frac{e^{-\frac{H(\mathbf{\Gamma})}{k_B T}}}{Q(N,V,T)}, \tag{2.102}$$

where $H(\mathbf{\Gamma})$ is the total classical energy and $Q(N,V,T)$ is the infinite sum over all phase-space for all positions and momenta, which can be written as:

$$Q(N,V,T) = \frac{1}{N!}\int \mathrm{d}\mathbf{\Gamma} e^{-\frac{H(\mathbf{\Gamma})}{k_B T}}. \tag{2.103}$$

The factor $N!$ allows for the distinguishable nature of classical particles, whereas quantum particles are indistinguishable.

2.10 Molecular Dynamics

Molecular dynamics is the method used in this thesis to simulate the motion of the atoms throughout time. If the potential energy of a system is known then MD can determine the movement of the atoms at finite temperature. The potential energy, and subsequently the interatomic forces, can be determined from a range of methods; therefore molecular dynamics can be used with a wide range of methods. The interatomic forces are used to determine the position of the atoms at a time t. However, as the atoms move the potential-energy surface changes, so the time period, $\triangle t$, is chosen to be small relative to the timescales of atomic motion and the potential-energy surface is recalculated after each period. This is repeated to generate a trajectory of the desired duration.

The trajectories of the atoms can then be analysed in order to derive macroscopic or collective parameters such as diffusion coefficients or ionic conductivities, and the trajectories of individual atoms or a small selection of atoms can be analysed to elucidate the microscopic details of diffusion pathways and atom motions.

Molecular dynamics solves the classical equations of motion by numerical integration for all the nuclei in the system. In MD the atomic nuclei are treated as classical mass points, therefore any quantum effects are ignored. The quantum effects of tunnelling through potential barriers and the Heisenberg uncertainty principle do not significantly contribute to the motion of atoms in the

classical limits of high temperatures and heavy particles. When investigating the diffusion and related properties of a system the electronic structure determines the interatomic forces and without accurate forces the trajectories generated from the equations of motion are spurious.

The equations of motion, if solved analytically, should give a deterministic answer and any little differences in the starting conditions lead to different trajectories even for short simulation times. The longer the simulations are run for, the greater the divergence of the two simulations. Whether the difference in starting conditions is a very small change in a single atom position or the use of a different computational architecture the results will vary greatly. However, the time averages of equilibrium properties must be independent of initial conditions and so the system must reach a point where the initial conditions are forgotten. This is called equilibration. A MD simulation starts with the input of the number, positions and velocities of the atoms. The simulation proceeds for a given amount of time until the system equilibrates, then the production phase can commence. This is the main part of a MD simulation and where the equilibrium phase-space trajectories, which are to be analysed for the desired properties, are generated. Identification of equilibrium is not simple and a detailed discussion can be found in Haile (1997). Equilibrium is a macroscopic concept and applies to a specific duration. The point of equilibration used in this thesis was taken to be when the conserved quantities of a simulation fluctuate about a stable average.

2.10.1 Equations of Motion

The classical equations of motion are used to describe the motion of atoms. The Newtonian equations of motion are integrated using numerical methods for each individual atom i:

$$\mathbf{F}_i = m_i \frac{\mathrm{d}^2\mathbf{r}}{\mathrm{d}t^2} = m_i \ddot{\mathbf{r}}_i, \tag{2.104}$$

where $\mathbf{F}_i$ is the force on atom i, m_i are the masses, and $\mathbf{r}_i$ is the three-dimension position vectors. The forces are determined from the gradient of the potential energy surface. This leads to a conservation of total energy in the system and the centre of mass is unchanged. The total energy, E can be written as:

$$E = U(\mathbf{r}_i) + K(\dot{\mathbf{r}}_i), \tag{2.105}$$

where U is the potential energy and K is the kinetic energy. The Newtonian equations of motion

can be written as:

$$\frac{\mathrm{d}}{\mathrm{d}t}(m_i\dot{\mathbf{r}}_i) = -\frac{\partial U}{\partial \mathbf{r}_i}. \tag{2.106}$$

The Lagrangian function, L, can be defined as the difference of the kinetic and potential energies:

$$L = K(\dot{\mathbf{r}}_i) - U(\mathbf{r}_i). \tag{2.107}$$

The conjugate momentum $\mathbf{p}_i$ is defined by:

$$\mathbf{p}_i = \frac{\partial L}{\partial \mathbf{r}_i} = \frac{\partial K}{\partial \mathbf{r}_i}. \tag{2.108}$$

The Hamiltonian is the energy expressed in terms of the position coordinates and the conjugate momentum:

$$H(\mathbf{p}_i, \mathbf{r}_i) = E. \tag{2.109}$$

The equations of motion can therefore be expressed in terms of position and conjugate momentum:

$$\frac{\mathrm{d}q_i}{\mathrm{d}t} = \frac{\partial H}{\partial \mathbf{p}_i}, \qquad \frac{\mathrm{d}\mathbf{p}_i}{\mathrm{d}t} = -\frac{\partial H}{\partial \mathbf{r}_i}. \tag{2.110}$$

For a system in equilibrium without external forces, the potential depends merely on the positional coordinates and not the velocities. If the kinetic energy is written as:

$$K = \frac{1}{2}m_i\dot{\mathbf{r}}_i^2, \tag{2.111}$$

then:

$$\mathbf{p}_i = \frac{\partial K}{\partial \dot{\mathbf{r}}_i} = m_i\dot{\mathbf{r}}_i, \tag{2.112}$$

and the Hamiltonian can be written as:

$$H(\mathbf{r}_i, \mathbf{p}_i) = \sum_{i=1}^{N} \frac{\mathbf{p}_i^2}{2m_i} + U(\mathbf{r}_i). \tag{2.113}$$

For a many-body system the equations of motion cannot be solved algebraically and must be solved numerically. This numerical integration of the Newtonian equations of motion is achieved by using the velocity Verlet algorithm (Verlet, 1967, 1968). It is widely used due to its low drift and stability compared to the Euler method (Press et al., 1992). Verlet integration also is time-reversible and area-preserving. The position, and therefore trajectories, after some time, $\triangle t$, can be written in terms of the positions and velocities at time $t = 0$ by using the expansion of a Taylor series:

$$\mathbf{r}_i(\triangle t) = \mathbf{r}_i(0) + \triangle t \mathbf{v}_i(0) + \frac{\triangle t^2}{2} \frac{\mathbf{F}_i(\mathbf{r}_i(0))}{m_i} + \mathcal{O}(\triangle t^3). \tag{2.114}$$

Initially the velocities are calculated at the middle of the time step, $^{\triangle t}/_2$ by:

$$\mathbf{v}_i(\triangle t/2) = \mathbf{v}_i(0) + \frac{\triangle t}{2} \frac{\mathbf{F}_i(\mathbf{r})}{m_i}. \tag{2.115}$$

The positions of the atoms at $\triangle t$ is therefore:

$$\mathbf{r}_i(\triangle t) = \mathbf{r}_i(0) + \mathbf{v}_i(\triangle t/2)\triangle t. \tag{2.116}$$

Now the new positions of the atoms are known, the interatomic forces can be calculated by DFT or FF. The forces at $\triangle t$ can then be used to determine the velocities at $\triangle t$:

$$\mathbf{v}_i(\triangle t) = \mathbf{v}_i(\triangle t/2) + \frac{\triangle t}{2} \frac{\mathbf{F}_i(\triangle t)}{m_i}. \tag{2.117}$$

This means the forces $\mathbf{F}_i(\triangle t)$, positions $\mathbf{r}_i(\triangle t)$, and velocities $\mathbf{v}_i(\triangle t)$ are all known and can be used as the inputs for the next step. Although the velocities are calculated twice per time step this carries little computational cost. The calculation of the forces is the computationally costly step and need only be performed once per time step. An advantage of the Velocity Verlet algorithm is the need to store only one value for each of the positions, velocity and forces per atom. This minimizes the memory requirements of such calculations to only $9N$ memory locations for N atoms. The velocity Verlet algorithm requires inputted positions, forces, and velocities. The positions are taken from the starting structure and the forces from the subsequent DFT or FF calculation. The velocities need to be initialised and this can lead to some initial instability in the conserved quantities. This is one of the reasons MD simulations require an initial equilibration period for the system to reach a steady state.

The integration of the Newtonian equations of motion should conserve the total energy, to within the error of the numerical integration (Section 2.10.3). This gives the microcanonical ensemble where the number of particles, volume and total energy are held constant. Specifying the total energy of a simulation is not convenient and it is preferable to set a temperature. The equations of motion must be changed to reflect the use of constant temperature rather than constant energy. These constraints, added to the equations of motion, are called thermostats.

2.10.2 Gaussian Isokinetic Thermostat

Gauss proposed a formulation for mechanics that is more general than Newton's formulation. Gauss's formulation is based upon the principle of least constraint and was used to generate a thermostat for use in equilibrium and non-equilibrium molecular dynamics by Evans et al. (1983). This thermostat produces an isokinetic ensemble where the kinetic energy is held constant. It is the thermostat used in the simulations presented in this thesis. This thermostat does not produce a trajectory equivalent to the canonical ensemble.

There are many other thermostats available, but a detailed discussion of them is beyond the scope of this thesis. The equations of motion including the constraints of the isokinetic thermostat are:

$$\dot{\mathbf{p}}_i = \mathbf{F}_i + \alpha \mathbf{p}_i, \tag{2.118}$$

where $\mathbf{p}_i$ is the momentum of atom i and α being the thermostat coefficient. This is can be derived from the conservation of the kinetic temperature, T_0 throughout the simulation. The kinetic temperature is defined as:

$$\sum_{i=1}^{N} \frac{\mathbf{p}_i^2}{m_i} = \frac{0N}{2} k_B T_0, \tag{2.119}$$

when differentiated with respect to time:

$$\sum_{i=1}^{N} \frac{\mathbf{p}_i}{m_i} \cdot \dot{\mathbf{p}}_i = 0. \tag{2.120}$$

Using Eqn. 2.118 as a substitution for $\dot{\mathbf{p}}_i$ the resulting is:

$$\sum_{i=1}^{N} \frac{\mathbf{p}_i}{m_i} \cdot \mathbf{F}_i + \alpha \sum_{i=1}^{N} \frac{\mathbf{p}_i^2}{m_i} = 0. \tag{2.121}$$

This can be rearranged to solve for α to give:

$$\alpha = -\frac{\sum_i \frac{\mathbf{p}_i}{m_i} \cdot \mathbf{F}_i}{\sum_i \frac{\mathbf{p}_i^2}{m_i}}. \tag{2.122}$$

It is notable that the kinetic temperature does not appear in the equations of motion or the thermostat coefficient. It is a requirement of the Gaussian isokinetic thermostat that the centre of mass does not drift as the temperature is defined by the sum of the individual atom momenta and if these are fluctuating then so will the kinetic temperature.

2.10.3 Drift in Conserved Quantities

The size of the timestep must be converged to the point where the conserved quantities do not drift over the duration of the simulation by more than an acceptable value. The timestep defines how frequently the interatomic forces are recalculated. If the timestep is too large then the forces are not sufficiently accurate and thus the inputs into the equations of motion are not valid and then the results, and conserved quantities, are also invalid.

2.11 Limitations of Molecular Dynamics

The severe limits on the simulation length and number of particles that can be managed with current computational resources restricts MD to studying diffusion in liquids or very fast-ion solid-state conductors at high temperatures. This is because the timescales accessible with MD are much shorter than the timescales typical of solid-state diffusion. There have been multiple attempts to extend MD to slower rates of diffusion by increasing the frequency of the rare diffusion events. Performing MD simulations at much higher temperatures will increase the ratio of thermal energy, $k_B T$, to the activation energy, E_A, which then increases the frequency of diffusion events. This tactic has been employed by Farrell et al. (2009) to study solid $Li_4BN_3H_{10}$ but the high temperatures melted the system. The physical description of the system at the simulation temperature cannot readily be extrapolated to temperatures and phases of interest. An alternative attempt involved heating only the mobile ions (Boulfelfel et al., 2011) in solid $LiFePO_4$. Selectively heating the

mobile Li^+ ions leads to much more frequent Li-ion hops without heating the anion framework and therefore not changing the structure. The setup of such a simulation is similar to an experiment where specific frequencies are applied to match vibrational modes of the mobile species. However, there is no theory that allows the results of selective heating simulations to be extrapolated back to the equilibrium point and therefore the results cannot be compared with experimentally-determined diffusion coefficients. These simulations do, however, give microscopic diffusion pathways with great detail. Rather than alternating the temperature of the system, another way to increase the frequency of rare events is to rescale the atomic masses (Tsuchida, 2011). The motion of atomic vibrations can be increased by reducing the atomic mass, alternatively the rate of atomic vibrations can be decreased by increasing the mass. Again this suffers from the inability to extract quantitative results that can be compared to equilibrium values. The meta-dynamics and hyper-dynamics simulation techniques (Laio and Parrinello, 2002; Laio and Gervasio, 2008; Voter, 1997) modify regular MD to elucidate the minimum free-energy paths of specific events. Where a MD simulation may get trapped in a small metastable region, meta-dynamics will escape this minima using the lowest available energy pathway. Such methods have been limited to small systems so far and require prior knowledge of events to parametrize the meta-dynamics algorithm.

In this work non-equilibrium molecular dynamics (NEMD) is used to increase the frequency of rare diffusion events. The transport phenomena are simulated directly by artificially introducing an external field to the system that only interacts with the mobile species of interest. The external field induces diffusion in a predictable manner. The response of the system to the external field is described by linear-response theory and therefore, despite being a non-equilibrium simulation, an equilibrium value for the diffusion coefficients can be calculated. Also, if the external field is small enough to only induce a linear response from the system then the nature of the microscopic diffusion processes is not changed, merely the frequency. NEMD thus yields meaningful values for macroscopic equilibrium diffusion coefficients and also can elucidate the microscopic diffusion pathways. There are a range of NEMD methods available to study diffusion as well as other transport properties. NEMD is discussed further in Section 2.12.

2.12 Non-Equilibrium Molecular Dynamics

Molecular dynamics is based upon systems in thermodynamic equilibrium, where the variables of the system do not depend on time or position. The transport properties in equilibrium systems

differ from non-equilibrium systems. Brownian motion of pollen grains suspended in a fluid made up of much lighter particles, as described by the Langevin equation is an example of transport in an equilibrium system. In the case of diffusion, including in solids, the self-diffusion coefficient from the Sutherland-Einstein relation (Eqn. 2.30) describes a random walk by a particle in an equilibrium system. However, transport phenomena are non-equilibrium by nature. Diffusion and heat flow, which consist of macroscopic movements, are described by Fick's law of diffusion and Fourier's law of heat conduction. Both processes involve transport from a region of high concentration to a region of low concentration. The aforementioned laws allow calculation of the transport coefficients from the determined fluxes.

In this thesis NEMD has been used to model solid-state diffusion in order to extend the temperature range accessible by equilibrium MD. NEMD has been applied to a wide range of fields (Evans and Morriss, 2008). One of the first NEMD simulations involved using inhomogeneous boundary conditions to model thermal conductivity. Ciccotti and Tenenbaum (1980) studied the thermal conductivity of a Lennard-Jones fluid by considering the system in a box where two opposing walls have different temperatures. The particles colliding with the respective walls were reflected with a new velocity determined by an equilibrium velocity distribution which is determined in turn by the two temperatures. This creates a thermal gradient and the thermal conductivity was then calculated using Fourier's law. The results compared well with experimental data. However problems, including the stacking of molecules near the walls, arise from using the two opposing walls at different temperatures and this can lead to a change in the microscopic structure. Also, to measure a statistically-significant heat flux the temperature difference between the two opposing walls, which are typically separated by a distance of tens of Angstroms, must be very large.

In the case of diffusion, an equivalent concentration gradient (or chemical potential) can be set up in the system. Instead of two opposing walls having two temperatures they could have two different chemical potentials. Attempts have been made at setting up such simulations by Heffelfinger and van Swol (1994). Their method is known as the dual-control-volume-grand-canonical molecular-dynamics method (DCV-GCMD). It involves a long supercell with opposing walls acting as particle reservoirs. This allows for the direct measurement of diffusion in the presence of a steady-state chemical potential. This method is hindered by the need for very large supercells to account for the concentration gradients, which can make such simulations computationally unfeasible. Early NEMD attempts at using concentration gradients (Maginn et al., 1993) involved attaching two systems to-

gether, with differing particle-number densities, then performing an equilibrium MD simulation. After enough time has passed the density goes from a step function to constant throughout the system. This method comes undone as, without extensive testing of different initial density differences, it is not known whether the system falls in the linear regime where Fick's law applies. Using opposing walls to create a concentration gradient forbids the use of periodic boundary conditions as the periodicity is broken creating an inhomogeneous system. This leads to strongly size-dependent results.

The next advance in NEMD was to replace the explicit concentration gradients with an external field that imitates the effect of the gradients. This is referred to as synthetic NEMD. This does not mimic experimental conditions in the same way as previous NEMD methods. Synthetic NEMD uses an external field to achieve the same effect. The external field is added into the equations of motion for each individual particle. Given all particles experience the external field, the system is therefore homogeneous and periodic. This allows periodic boundary conditions to be used, so the size of the system need not be bigger than the size used in an equilibrium MD study. Synthetic NEMD homogeneous algorithms have been developed for shear viscosity (Evans, 1979), thermal conductivity (Evans, 1982) and self-diffusion (Evans et al., 1983). The field is covered in a fuller description in Evans and Morriss (2008). In the cases of thermal conductivity and self-diffusion the external field replaces the need for temperature and concentration gradients respectively by acting on all the atoms. For shear viscosity, the algorithm is applied to the periodic boundary condition to induce shear stress.

In the synthetic formulation an external field is applied to the system. The effect of the external field is described by linear response theory. This makes synthetic NEMD exact and the application of the external field yields the desired response. The only application of NEMD in this thesis is to study self-diffusion and for the rest of this thesis it shall be the only type of NEMD discussed. However, much of what will be written about self-diffusion NEMD relates to other NEMD methods.

For self-diffusion, synthetic NEMD uses the external field, $\mathbf{F_e}$, which is introduced into the equations of motion for the mobile ions. The diffusing particles are labelled with a colour charge, c_i, for particle i, which couples the labelled particles to the external field. The force exerted on the ith particle is therefore $c_i\mathbf{F_e}$. This is equivalent to an electric field on an electric charge, except the colour charges on the particles do not interact and therefore, with no external field present, the system behaves as it would under equilibrium molecular dynamics. The external field is often

referred to as the colour field.

Synthetic self-diffusion NEMD had previously only been applied to liquids and gasses until Aeberhard et al. (2012) recently applied self-diffusion NEMD to solid state $LiBH_4$ and studied the transport properties. That work is used as the basis for studying the diffusion properties in this thesis.

2.12.1 Linear Response Theory

The result of the external field is described by linear response theory (Evans and Morriss, 1984), which is summarized briefly below. The strength of the external field is assumed to be sufficiently small to induce only a linear response from the system. For too large a field strength nonlinear, effects will occur such as too much heat being added to the system making a steady-state unobtainable. The range of field strengths that elicit a linear response is called the linear regime. In the linear regime only equilibrium fluctuations and processes are observed. The presence of the external field does not change the characteristics of the equilibrium processes, just how often they are observed. The external field is constant throughout space but not necessarily throughout time. For system of N atoms experiencing the external field $\mathbf{F}_e(t)$ from $t = 0$, the dynamics obey the following equations:

$$\dot{\mathbf{q}}_i = \frac{\mathbf{p}_i}{m_i} + \mathsf{C}_i \mathbf{F}_e(t), \tag{2.123}$$

$$\dot{\mathbf{p}}_i = \mathbf{F}_i + \mathsf{D}_i \mathbf{F}_e(t). \tag{2.124}$$

The matrices C_i and D_i couple the external field to the particles. It is assumed that in the absence of the external field and with the system at equilibrium the canonical kinetic energy satisfies the equipartition relation. The Hamiltonian of this system is the sum of the kinetic and potential energy:

$$H_0 = \sum_{i=1}^{N} \frac{\mathbf{p}_i^2}{2m_i} + E(\mathbf{q}). \tag{2.125}$$

It is not assumed that a Hamiltonian exists that will yield the field-dependent equations of motion. In the absence of the external field the total energy is a constant of motion. However, the external field performs work on the system generating heat. The rate of change in the total energy due to the application of the external field is:

$$\dot{H}_0 = \sum_{i=1}^{N} \left[\frac{\dot{\mathbf{p}}_i(t) \cdot \mathbf{p}_i}{m} - \dot{\mathbf{q}}_i(t) \cdot \mathbf{F}_i \right]. \tag{2.126}$$

Eqn. 2.126 can be rewritten using the definitions from Eqns. 2.123 and 2.124 as:

$$\dot{H}_0 = -\sum_{i=1}^{N} \left[-\frac{\mathbf{D}_i \cdot \mathbf{p}_i}{m} - \mathsf{C}_i \cdot \mathbf{F}_i \right] \mathbf{F}_e(t) \equiv -\mathbf{J} \cdot \mathbf{F}_e(t), \tag{2.127}$$

where $\mathbf{J}$ is the dissipative flux. The response of the system to the external field can be determined by measuring the average response of an arbitrary phase variable $B(\Gamma)$ after some time t.

$$\langle B(t) \rangle = \int \mathrm{d}\Gamma B(\Gamma) f(\Gamma, t). \tag{2.128}$$

This is the Schrödinger representation of the average response of B. This average response of the system to the external field is determined by applying the external field to an ensemble of initial phases. This then reduces the problem to determining the distribution function f, which is selected from the starting states from the equilibrium canonical ensemble. Once the perturbation of the external field is applied, determining the average response becomes equivalent to determining the perturbation to the distribution function. The distribution function of the perturbed system is separated into two parts; the unperturbed system f_c and the effect of the perturbation $\triangle f$:

$$f(\Gamma, t) = f_c + \triangle f(\Gamma, t). \tag{2.129}$$

The rate of change in the distribution function is defined by the Liouville equation. It can therefore be shown that the linear response of the phase variable B is:

$$\langle B(t) \rangle = \langle B(0) \rangle + \int \mathrm{d}\Gamma B(\Gamma) \triangle f(\Gamma, t). \tag{2.130}$$

The part of the distribution function describing the effect of the perturbation can be related to the dissipative flux using the Liouville operator on the distribution function for the canonical ensemble (Morriss and Evans, 1985):

$$\langle B(t) \rangle = \langle B(0) \rangle_{NVT} + \frac{1}{k_B T} \int_0^t \mathrm{d}s \, \langle B(t-s) \cdot \mathbf{J}(0) \rangle_{NVT} \cdot \mathbf{F}_e(s). \tag{2.131}$$

This defines the average response to the perturbation by the external field and the related dissipative flux. The applied external field performs work on the system, this then prevents the system from achieving an equilibrium state. The work is converted into heat and for small fields this work added is proportional to $|\mathbf{F_e}|^2$. This is a non-linear effect and thus requires the use of a thermostat to give isothermal linear-response theory.

2.12.2 Synthetic NEMD Algorithm for Self-diffusion in Solids

Section 2.12.1 is general to synthetic NEMD. In this subsection the above general results are used to derive the algorithm for self-diffusion in solids (Evans et al., 1983; Aeberhard et al., 2012). The response to the external field is used to determine the self-diffusion coefficient of the equilibrium system. The original algorithm developed by Evans et al. (1983) was designed for liquid systems and further developed by Aeberhard et al. (2012) for solid state lithium-ion conductors. This formulation assumes the lithium ions diffuse in a similar manner to diffusion in liquids, but in the presence of a static framework of anions. In the case of Li_2O and Li_3N the self-diffusion coefficient of the anion is approximately four orders of magnitude lower than that of the cation. Aeberhard et al. (2012) studied $LiBH_4$ where the difference is merely two orders of magnitude and this was a large enough difference for the timescales being studied. Therefore only the mobile lithium ions experience the external field and, the essentially static anions do not interact with the external field. Half of the lithium ions are labelled +1 colour charge and the other half as -1 colour charge, with the anions have 0 colour charge. The external field is then applied. The external field is conceptually similar to an electric field in that the displacement of the colour-labelled species parallel to the applied field is linearly proportional to the field strength. As the colour field strength increases from zero, the response is initially linear and is described by Eqn. 2.131, but when the field becomes too strong, nonlinear effects begin to dominate and linear response theory breaks down.

The general result of Eqn. 2.131 applied to the specific case of lithium-ion diffusion in solid-state systems is explained below in order to determine the self-diffusion coefficient of the lithium ions. The coupling coefficients of the external field to the system, as defined in Eqn. 2.123 and 2.124, are set to:

$$\mathsf{C}_i \to 0, \tag{2.132}$$

$$\mathsf{D}_i \rightarrow c_i, \tag{2.133}$$

where c_i are the colour charges for each individual atom. Using these coupling coefficients the dissipative flux is:

$$\mathbf{J}(\Gamma) = -\sum_{i=1}^{N} c_i \frac{\mathbf{p}_i}{m}. \tag{2.134}$$

Although that the external field has both a magnitude and direction, the response resulting from the external field is a scalar quantity and lacks direction. This scalar quantity is the colour flux, J_c, which is analogous to the electric-current density. The colour flux is a measure of how much colour charge, or how many lithium ions, passes through an area orthogonal to the direction of the external field. The velocity parallel to the external field is:

$$v_i(t) = \mathbf{v}_i(t) \cdot \frac{\mathbf{F}_e}{|\mathbf{F}_e|}. \tag{2.135}$$

The colour flux is therefore:

$$J_c(t) = \frac{1}{V} \sum_{i=1}^{N} c_i v_i(t). \tag{2.136}$$

Using the general result from linear response theory for the average value of the response (Eqn. 2.131):

$$\langle J_c(t) \rangle = \frac{V}{k_B T} \int_0^t \mathrm{d}s \, \langle J_c(t-s) \cdot J_c(0) \rangle \cdot \mathbf{F}_e. \tag{2.137}$$

In order to obtain a self-diffusion coefficient, the Green-Kubo relation discussed in Section 2.3 is used. This relates the self-diffusion coefficient to the single-particle velocity-autocorrelation function. The colour-current autocorrelation function, $\langle J_c(t-s) \cdot J_c(0) \rangle$, can be related to the single-particle velocity autocorrelation function using Eqn. 2.136. Then Eqn. 2.137 becomes:

$$\langle J_c(t) \rangle = \frac{1}{k_B V T} \sum_{i=1}^{N} c_i^2 \int_0^t \mathrm{d}s \, \langle v_i(t-s) \cdot v_i(0) \rangle \cdot \mathbf{F}_e. \tag{2.138}$$

This means that the average response to the external field after a given time can be determined

from the integral of the velocity-autocorrelation function. This can then be used to obtain a self-diffusion coefficient using the Green-Kubo relation (Section 2.3) in the limit of $t \to \infty$:

$$D = \frac{k_b T}{\rho_c} \lim_{t\to\infty} \lim_{F_e \to 0} \frac{\langle J_c(t) \rangle}{F_e}, \tag{2.139}$$

where the number density of colour-labelled particles $\rho_c = N_c/V$. In the above result the colour flux is measured after a given time from a starting point of a system in equilibrium. The above result is only valid if the system is in a steady-state, but in the long-time limit the work done by the external field will be converted to heat. This removes the steady state. In order to remove the added heat a thermostat is applied to the equations of motion to account for heat added by the external field. The linear response theory results are still valid for synthetic NEMD algorithms using a thermostat, as shown by Morriss and Evans (1985).

In this formulation of NEMD the equations of motion for an equilibrium MD simulation are modified to account for both the external field and the Gaussian isokinetic thermostat. The equations of motion for Li_2O and Li_3N become:

$$\dot{\mathbf{p}}_i = \begin{cases} \mathbf{F}_i + \alpha \mathbf{p}_i + \mathbf{F}_c & \forall i \in \{\mathrm{N},\, \mathrm{O}\} \\ \mathbf{F}_i + c_i \mathbf{F}_e & \forall i \in \{\mathrm{Li}\} \end{cases}, \tag{2.140}$$

where $\mathbf{F}_i$ are the interatomic forces upon atom i, which are calculated by force field or DFT methods. The colour charge of labelled atoms is c_i and the external, or colour, field is $\mathbf{F}_e$. The anions do not interact with the colour field, but are coupled to the thermostat by the parameter α and are subject to the constraint force $\mathbf{F}_c$, which maintains the centre of mass of the entire system as constant. This accounts for both drift due to numerical errors and movement of the centre of mass by the motion of the unconstrained lithium atoms. The Gaussian isokinetic thermostat requires the centre of mass not to drift.

$$\alpha = -\frac{\sum_{i\in\{\mathrm{N},\,\mathrm{O}\}} \frac{\mathbf{p}_i \cdot (\mathbf{F}_i + \mathbf{F}_c)}{m_i}}{\sum_{i\in\{\mathrm{N},\,\mathrm{O}\}} \frac{\mathbf{p}_i^2}{m_i}}, \tag{2.141}$$

$$\mathbf{F}_c = -\frac{1}{N_{N,\,O}} \sum_{i\in\{\mathrm{N},\,\mathrm{O}\}} \mathbf{F}_i. \tag{2.142}$$

The application of the colour field induces a streaming velocity for the colour-charged species,

but given that the mobile ions are not coupled to the thermostat the streaming velocities do not need to be calculated. The kinetic temperature, which the thermostat holds constant, is determined by the peculiar velocities. Therefore the thermostat removes heat isotropically. However the colour field only adds heat in a single direction. This leads to a situation where there is a build up of heat in the direction parallel to the direction of the colour field. The self-diffusion algorithm created by Evans et al. (1983) only applied the thermostat to the directions orthogonal to the direction of the colour field. Later versions (Evans and Morriss, 2008) applied the thermostat isotropically, but took account of the streaming velocities. This is very difficult to do for small systems due to large fluctuations in the instantaneous streaming velocity. The self-diffusion algorithm used in this thesis developed by Aeberhard et al. (2012) only applied the thermostat to the anions. This saves the need to compute the streaming velocities. The temperature of the mobile lithium ions is controlled via interactions with the anions. This has no effect on the linear response.

Aeberhard et al. (2012) modified the CP2K[1] program, which allows atomistic and molecular simulations of solid-state, liquid, molecular, and biological systems, in order to implement the self-diffusion NEMD algorithm (Eqn. 2.140). The original self-diffusion NEMD version of CP2K was designed to work only with DFT. This was updated by the present author to account for the use of force-field simulations used in this thesis.

2.12.3 Calculating Self-diffusion Coefficients from NEMD Simulations

It was shown in the previous sections that the equilibrium self-diffusion coefficient can be calculated from NEMD simulations. Eqn. 2.139 relates the self-diffusion coefficient to the steady-state average colour flux. The colour flux can be calculated using Eqn. 2.138 from the single-particle velocity-autocorrelation function. In practice this is cumbersome and a more convenient method is available. The time average of the steady-state colour flux is:

$$\langle J_c \rangle = \lim_{t\to\infty} \langle J_c(t) \rangle = \lim_{t_s\to\infty} \frac{1}{t_s} \int_0^{t_s} \mathrm{d}t\, J_c(t). \tag{2.143}$$

Using the definition of colour flux by Eqn. 2.136 this becomes:

[1] CP2K is a freely available suite of programmes for molecular dynamics simulations; it is available at: http://cp2k.org.

$$\langle J_c \rangle = \lim_{t_s \to \infty} \frac{1}{t_s V} \sum_{i=1}^{N} c_i \left[\mathbf{r}_i(t_s) - \mathbf{r}_i(0) \right]. \tag{2.144}$$

The energy dissipation is defined in Eqn. 2.127. Therefore the integrated energy dissipation is:

$$H_0(t) - H_0(0) = \int_0^t \mathrm{d}t \ \langle J_c(t) \rangle \, V F_e. \tag{2.145}$$

Using Eqn. 2.143 and 2.144 this becomes:

$$H_0(t) - H_0(0) = \int_0^t \mathrm{d}t \ \langle J_c(t) \rangle \, V F_e = F_e \sum_{i=1}^{N} c_i \Delta r_i(t). \tag{2.146}$$

This is the time-integrated dissipative flux conjugate to the field, where $\Delta r_i(t)$ is the displacement of atom i parallel to the colour field. If the time-integrated dissipative flux conjugate to the field is plotted against time, the gradient can then be used to determine the time average of the steady-state colour flux. This, in turn, can be used to calculated the self-diffusion coefficient. This plot is akin to plotting the mean squared displacement against time for equilibrium MD simulations. Both show the overall amount of displacement, details of discrete jumps can be discerned, and the gradients are proportional to the self-diffusion coefficient.

CHAPTER 3

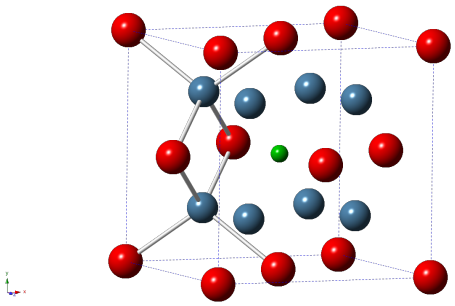
Li_2O

In this chapter, diffusion in solid lithium oxide, Li_2O, is simulated over the temperature range 873 $<$ T/K $<$ 1603 by using non-equilibrium molecular dynamics. Lithium oxide is one of the simplest binary compounds of lithium. There is a range of possible technological applications for Li_2O, for example as a blanket breeding material for nuclear fusion reactors, a component in lightweight high-power density batteries and, when used along side Li_3N, as a possible hydrogen store. When used as a nuclear fusion blanket material Li_2O acts to convert high-energy neutrons into heat and to allow rapid tritium release in order to maintain the deuterium-tritium fusion reaction. This relies on a high melting point and high thermal conductivity. When it is used in Li-ion or Li-air batteries the thermal properties are not of such importance, but the rapid diffusion of Li^+ cations is crucial.

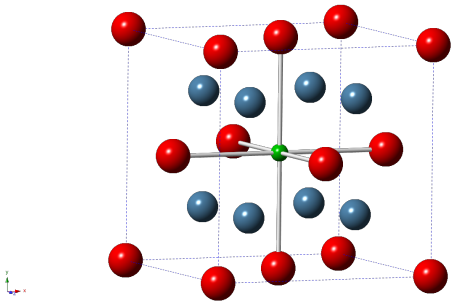
3.1 Fluorite Structure

Li_2O adopts the face-centred cubic anti-fluorite structure with Li^+ cations occupying the tetrahedral sites at $\left(\frac{1}{4}, \frac{1}{4}, \frac{1}{4}\right)$ in a close-packed array of oxide ions. This is the reverse of the arrangement of the fluorite structure. Each of the anions is thus coordinated by a cubic arrangement of eight Li^+ cations; the edges of this cube are parallel to those of the unit cell (Fig. 3.1a). A vacant interstitial site, coordinated by six O^{2-} anions, lies at the centre of the unit cell (Fig. 3.1b).

The fluorite structure is the same as the anti-fluorite structure adopted by Li_2O except for the interchange of the cations and anions; both adopt the space group $Fm\bar{3}m$. Many binary systems adopting the fluorite structure exhibit a type II transition to superionic conductivity. These include CaF_2, BaF_2, β-PbF_2, $SrCl_2$, UO_2, and ThO_2 (Keen, 2002; Roberts and White, 1986; Dickens et al., 1983, 1979; Elcombe and Pryor, 1970; De Vita et al., 1992a; Catlow et al., 1978; Matzke, 1970) . In fact most type II superionic materials adopt the fluorite or the anti-fluorite structure, but the fluorite systems have been studied to a greater extent than the anti-fluorite materials. In both cases, the



(a)



(b)

Figure 3.1: The unit cell of Li_2O; red and blue circles represent oxygen and lithium, respectively. The (a) tetrahedral coordination of lithium and edge-sharing of adjacent tetrahedra and (b) octahedral coordination of the interstitial site, represented by a green circle at $\left(\frac{1}{2}, \frac{1}{2}, \frac{1}{2}\right)$, are shown.

ions on the tetrahedral sites are the mobile species. This can be attributed to the lower activation energy needed to hop from a site with a lower coordination number and the mobile ion having a lower charge than the ion forming the close packed array. The associated transition temperature, T_C, is typically $\sim 80\,\%$ of the melting point e.g. CaF_2 $T_C = 1430$ K, $T_M = 1633$ K and $SrCl_2$ $T_C = 1000$ K, $T_M = 1146$ K. This transition temperature also corresponds to a Schottky-type anomaly in the specific heat (Catlow et al., 1978; Dickens et al., 1979, 1983) and a large decrease in the elastic constant C_{11} (Elcombe and Pryor, 1970; Kleppmann, 1978). The diffusion coefficient of the mobile anion shows a significant, but continuous, increase at the transition temperature. This apparently anomalous event involves the onset of thermally-induced disorder on the regular anion lattice. Aliovalent doping of the cation site with trivalent or tetravalent cations leads to an increase in anion concentration in order to maintain charge neutrality, e.g. $Ca_{0.94}Y_{0.06}F_{2.06}$, and a decrease in T_C whilst maintaining the fluorite structure (Hofmann et al., 1997).

3.2 Superionic Diffusion in Li_2O

One difference between Li_2O and the other fluorite systems exhibiting superionic conductivity is the lack of sudden change in the specific heat in Li_2O (Tanifuji et al., 1978), but as with the other fluorites there is the drop in the elastic constant C_{11} (Hull et al., 1988). The diffusion coefficient was measured over a wide temperature range by Oishi and Kamei (1979) using the tracer method. No radioactive isotope of lithium is readily available and the stable isotope ^{6}Li was therefore employed as a tracer. Two samples were prepared: one with a natural abundance of ^{6}Li, 7.42 %, and the other enriched in ^{6}Li to 95 %. The self-diffusion coefficient was determined by the distribution of the isotopes after a diffusion-anneal. The analysis assumed no grain-boundary enhancements of the diffusion coefficient and measured a wide temperature range, which makes this data set ideal for comparison with the computational results. The results are shown in Fig. 3.2 in an Arrhenius-type plot. By fitting two straight lines to the data, two temperature-dependence regions were identified with different activation energies. This analysis suggests a sudden discontinuous change from non-superionic to superionic behaviour. As mentioned earlier, the transition in type II superionic conductors, although sudden, is smooth and continuous. Therefore the activation energies and frequency factors determined from this analysis are of limited value. The self-diffusion coefficient of the oxide ion was measured by Akiyama et al. (1981) and is approximately five orders of magnitude lower than the lithium ion self-diffusion coefficient over the entire temperature range. The oxide diffusion coefficient shows a linear temperature dependence on an Arrhenius plot. There is also negligible electronic conductivity (Akiyama et al., 1981). The temperature dependence and absolute values of the diffusion coefficient for both the lithium and the oxide ions are similar to the diffusion coefficient of fluoride and calcium, respectively, in CaF_2.

The diffusion properties of Li_2O have made it a candidate for use in glass-ceramic and polymer-ceramic electrolytes in Li-air batteries (Kumar et al., 2010a). In these batteries a Li-metal anode, a highly Li-ion conducting solid electrolyte and a composite air cathode form a Li-O_2 cell. These solid-electrolyte Li-ion batteries have a significant safety advantage over traditional Li-ion batteries that use liquid electrolytes because the source of most safety issues involves rupture of the container, followed by ignition and explosion of the liquid electrolyte. The Li-O_2 cell provides an open-circuit voltage of $\sim 3.0\,\mathrm{V}$ and a theoretical specific energy of $11\,140\,\mathrm{Wh\,kg^{-1}}$ if the oxygen, which can be readily accessed from the air, is not considered as part of the battery. Considering these intrinsic

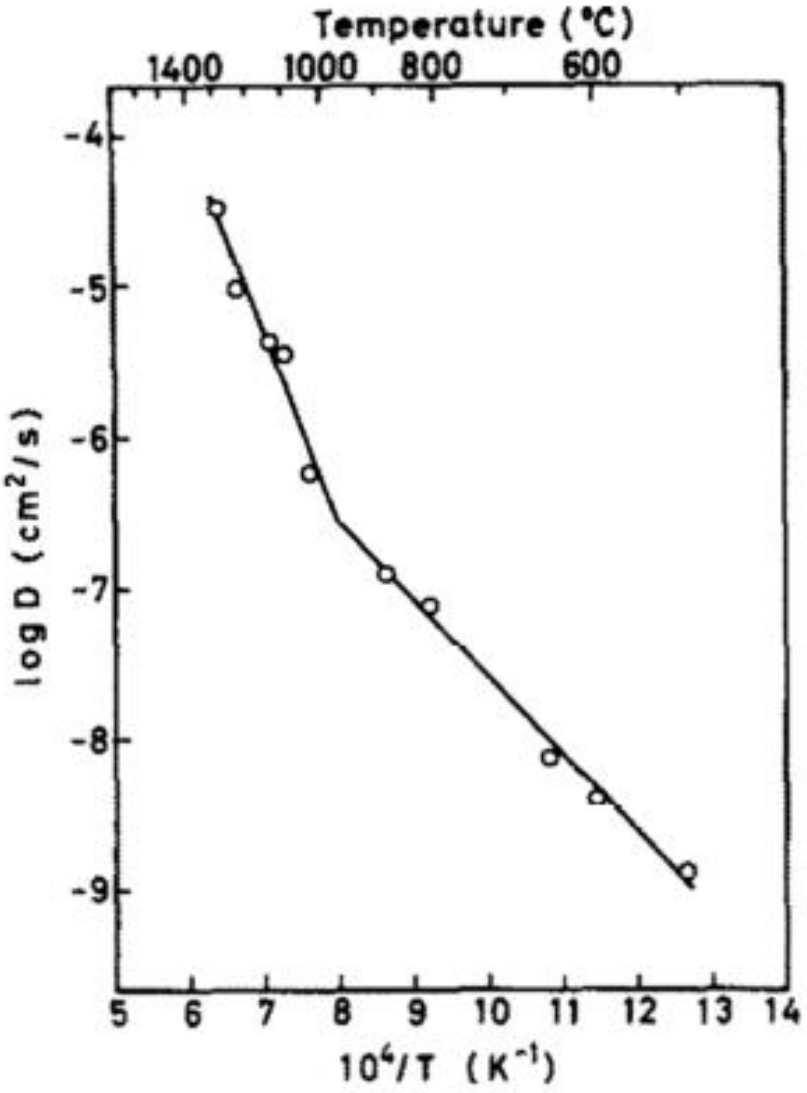


Figure 3.2: Self-diffusion coefficient of lithium ion in Li_2O as a function of temperature, from Oishi and Kamei (1979).

benefits of Li-air batteries, along with their thermal stability and rechargeability, Li-air devices have the potential to be viable high-energy and high power density batteries. The use of Li_2O in the electrolyte has been shown to improve conductivity and long-term stability (Kumar et al., 2009, 2010a,b).

Earlier studies of Li_2O were triggered by the potential for use in deuterium-tritium fusion reactors as a blanket breeder material (Smith et al., 1985; Kulcinski et al., 1986; Harries et al., 1985). Both the lithium and tritium diffusion are important properties for a potential solid-breeder material. The diffusion of lithium and tritium are considered to be closely related (Noda et al., 1994). A single-crystal neutron diffraction study performed by Farley et al. (1991) identified the rapid increase in the fraction of lithium ions occupying the octahedral-interstitial site to form a Frenkel defect in the region of 1200 K. This transition temperature, being $\sim 0.7\,T_m$, corresponds to the onset of superionic behaviour among the lithium ions. *Ab initio* calculations to model Li_2O showed the experimentally-observed rate of diffusion is too high to be solely attributed to the low concentration of Frenkel defects and therefore another, most likely concerted, mechanism must be operating simultaneously (De Vita et al., 1992a,b).

Li_2O has been the focus of many computational studies (Duan and Sorescu, 2009; Dovesi et al., 1991; Hayoun et al., 2005; Hayoun and Meyer, 2008, 2013; Fracchia et al., 1998; Pfeiffer et al., 2000; Goel et al., 2004; Gupta et al., 2012). Molecular dynamics simulations have been performed over a range of temperatures. The pathways of individual lithium atoms have been identified (Hayoun et al., 2005; Hayoun and Meyer, 2008) for diffusion in the superionic regime. However, diffusion in the non-superionic regime has not been modeled with much success. Diffusion coefficients have been calculated from MD simulations, but the values show poor agreement with the experimental data, especially so in the non-superionic temperature range where often no diffusion events were observed for the entirety of the MD simulation. The study by Fracchia et al. (1998) calculated the parameters for the Buckingham pair-potential using *ab initio* methods. These were then used in MD simulations. The short simulation time (10 ps) used limited the accessible temperature range. Only at the highest temperature simulated, 1300 K, was lithium diffusion observed. This significantly limits the comparison with experimental data. Pfeiffer et al. (2000) also used a pair-potential MD simulation to model Li_2O. They used a Pauling-type potential and again the simulation durations were rather short, 7.5 ps. Their simulations yielded no lithium or oxygen diffusion at the temperatures simulated in stoichiometric Li_2O, but they also simulated lithium deficient and oxygen

deficient supercells that did show diffusion on the timescales simulated. These two MD studies did not manage to yield diffusion coefficients comparable to experimental data and did not provide insight into the underlying diffusion mechanisms. However, both managed to show the effective use of pair-potentials for modelling the Li_2O system. The MD studies by Hayoun et al. (2005; 2008; 2013) investigated the mechanistic details of superionic diffusion in Li_2O. Different pathways were identified and their relative probabilities were proposed. However, the studies were limited to studying the superionic regime and did not offer insight into the low-temperature non-superionic regime.

3.3 Computational Details

The theoretical background and practical considerations for the FF-MD, FF-NEMD, and DFT-NEMD simulations performed on Li_2O were outlined in Chapter 2. These methods were implemented in the case of Li_2O as follows. In order to perform accurate calculations certain parameters need to be determined before long-timescale simulations can be performed. These include the time step for the integration of the equations of motion and the size of the supercell to be used in both MD and NEMD simulations. When DFT is used with MD or NEMD, the QUICKSTEP method, as implemented in CP2K, provides a very efficient method for calculating the interaction forces and it relies upon a dual basis set comprising of atom-based Gaussians and plane waves. Before a simulation can be undertaken the size of the Gaussian basis set and the cutoff energy of the plane waves must be determined to provide accurate results. The classical force-field simulations use the Buckingham potential with parameters previously determined by Fracchia et al. (1998) All of the MD and NEMD simulations were performed using the CP2K package.

The time step required is dependent on both the system being simulated and the chosen numerical integrator. During a MD simulation, once the positions and subsequently the forces are known the equations of motion can be solved to give the position of the atoms after some short time, Δt, called the time step. Obviously as soon as the atoms have been displaced the forces will change. However, if they are recalculated with enough frequency then the change in forces is small enough to provide a smooth and accurate trajectory. If the time between recalculation of the forces, the time step, is too large, the trajectory will be inaccurate and the conserved quantities will drift. However, in order to maximise the total simulation time and size of the system achievable with finite computational resources, the larger the time step the better. The highest frequency oscillation present in the system

will be the limiting factor for the time step, as this must be sampled sufficiently to give an accurate trajectory. A good starting point for determining the time step is to sample the highest frequency present 10-15 times per oscillation. Short duration simulations, 2.5 ps, were performed with the NVE thermostat on a 2x2x2 supercell of Li_2O at 1273 K with different time steps. The drift of the total energy, a conserved quantity, for different time steps is shown in Fig. 3.3. For Li_2O using a time step of 2 fs yields an energy drift of less than 0.002 eV/ formula unit over 2.5 ps, so a time step of 2 fs was chosen for all Li_2O MD and NEMD simulations in this thesis. Using a smaller time step does not significantly reduce the drift in the conserved quantity, whereas th 4 fs time step showed significant drift in the conserved quantity. Using this time step would yield an inaccurate trajectory for any simulation duration of use in modelling diffusion processes.

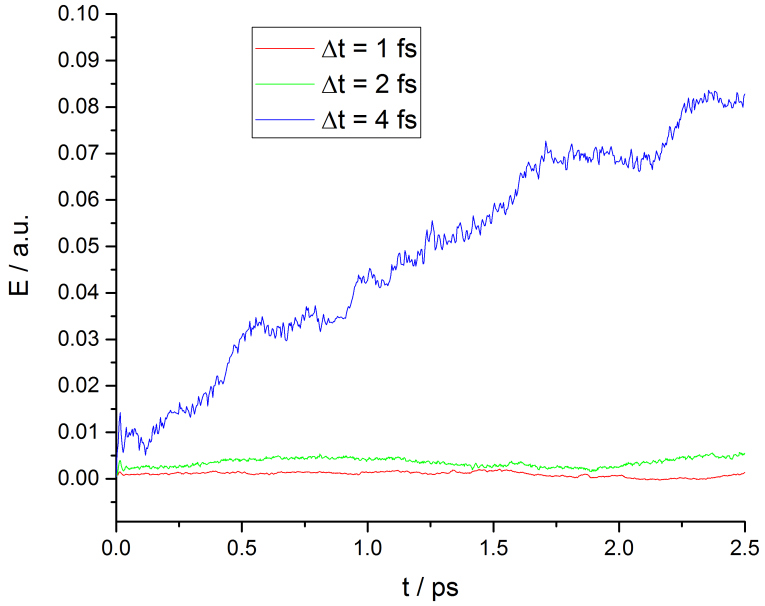


Figure 3.3: The total energy against time for MD simulations using the NVE thermostat at 1273 K performed on a 2x2x2 supercell of Li_2O. The red, green, and blues lines represent time steps of 1, 2, and 4 fs respectively.

The self-diffusion coefficient will vary with the direction of the applied field in a way that reflects the cubic symmetry of Li_2O. FF-NEMD simulations were performed as described above with the colour field applied along the [001], [110], and [111] directions. The simulation cell was then extended to form a supercell with lengths and number of atoms equivalent to or greater than the 2x2x4

supercell for a field applied along [001]. The linear regime was sampled at 0.02, 0.04, and 0.06 eV $Å^{-1}$ for each direction. Using a colour field of a greater magnitude gave a response that did not lie in the linear regime. From Table 3.1 we see that diffusion is greatest in the [001] direction, with the other two directions being three or four times smaller. This is unsurprising given the [001] direction is parallel to the direct path between nearest neighbour sites.

Periodic boundary conditions were used in all simulations presented. This leads to self-interaction issues where ions push-pull their periodic images, which can lead to inaccurate simulations (Probert and Payne, 2003; Castleton and Mirbt, 2004; Mattsson et al., 2005). When modelling and measuring diffusion coefficients this leads to very misleading results. In order to minimize the problem of self-interaction a large enough supercell must be used to separate the periodic images from themselves. However, increasing the size of the supercell significantly increases the computational cost for calculating forces and integration of the equations of motion. The thorough way to test for the effect of self-interaction is to repeat simulations for supercells of increasing size and then measure the diffusion coefficient of each to test for convergence. Preliminary studies showed that the unidirectional diffusion in response to the colour field allows for the use of an anisotropic supercell without biasing the computed diffusion coefficients. The length of the supercell parallel to the direction of the colour field was determined by a series of FF-NEMD simulations with the external colour field applied along the [001] direction and using supercells formed by a 2x2xN array of Li_2O unit cells, where the value of N was varied. The temperature was set at 1273 K, which lies at the beginning of the superionic regime for Li_2O. The linear regime was sampled for colour field strengths between $0.02-0.06$ eV $Å^{-1}$. The resulting trajectories were used to determine the lithium self-diffusion coefficient. This method is outlined in Section 2.12.3. The results represented in Fig. 3.4 show that as the length of the supercell increases in size, the diffusion coefficient along the z direction decreases and then converges. The NEMD simulations presented in this work were therefore performed on a supercell consisting of 128 formula units (384 atoms) in a 2x2x8 array of cubic unit cells. Calculations on 4x4x8 and 2x2x12 supercells, performed at 1273 K, which showed finite size errors in the Li diffusion coefficients of less

Table 3.1: The self-diffusion coefficient of lithium parallel to the direction of applied colour field.

Direction of applied field	D_{Li} / 10^{-7} cm^2 s^{-1}
[100]	2.701
[110]	1.006
[111]	0.779

than 14 %, showing the convergence limit. The lattice parameters used at all temperatures were determined from neutron single-crystal diffraction experiments (Farley et al., 1991). This means the 2x2x8 supercell at 1273 K has the dimensions of 9.54 Å × 9.54 Å × 38.16 Å. At these experimental densities the simulated dynamic pressures were ±2.5 GPa. The lattice parameters used were from experimental data because DFT calculations using the PBE functional typically overestimate the lattice parameter (Haas et al., 2009). This is due to the underestimation of nonbonded interactions, and lattice parameters derived from DFT should be used with caution or if possible avoided.

For the NEMD simulations all the lithium ions in the supercell were given a colour charge, as they are the mobile ions of interest. The oxide ions were not assigned colour charges as they are essentially static compared to the lithium ions. The self-diffusion coefficient for oxygen is about four orders of magnitude lower than the lithium self-diffusion coefficient. As proposed by Evans et al. (1983), in order to maintain overall net colour neutrality half of the lithium atoms were assigned +1 and the other half -1 colour charge. When the colour field was applied along [001] alternating (010) sheets of Li^+ cations were assigned +1 and -1 colour charge, as shown in Fig. 3.5.

The DFT calculations were performed with the QUICKSTEP package implemented in CP2K. This uses a dual basis set, rather than a single basis set, to represent the valence electrons and thus dramatically reduces the computational cost of force calculations. The use of short-range atom-centred Gaussian basis sets reduces the size of the plane wave basis set required. The core electrons are represented by the Goedecker-Tetter-Hutter pseudopotentials (Goedecker et al., 1996). The double-zeta Gaussian-basis set (VandeVondele and Hutter, 2007) was chosen as it gave a reasonable compromise between accuracy and computational cost (Fig. 3.6a). The plane wave cut-off energy of 280 Ry was chosen (Fig. 3.6b). The basis set and cutoff energy were determined by convergence of better than 1 meV in energy and 0.005 eV $Å^{-1}$.

The Buckingham potential is used to model interatomic forces for Li_2O (Eqn. 3.1). The parameters used in the calculations presented in this thesis are taken from Fracchia et al. (1998); the potentials derived in earlier studies do not reproduce the high-temperature properties of Li_2O. Their parameters were determined by fitting to a full *ab initio* Hartee-Fock model with an emphasis on the high temperature superionic properties. The energy difference between the Hartree-Fock and fitted potentials was less than 1 % at all distances measured.

$$V(r) = A\,exp(-r/\rho) - C/r^6. \tag{3.1}$$

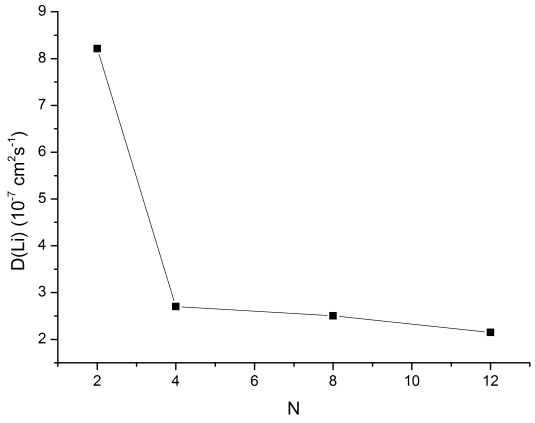


Figure 3.4: The self-diffusion coefficient of lithium in Li_2O supercells of 2x2xN unit cells.

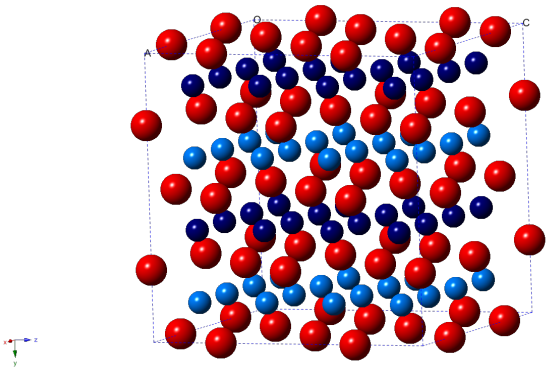
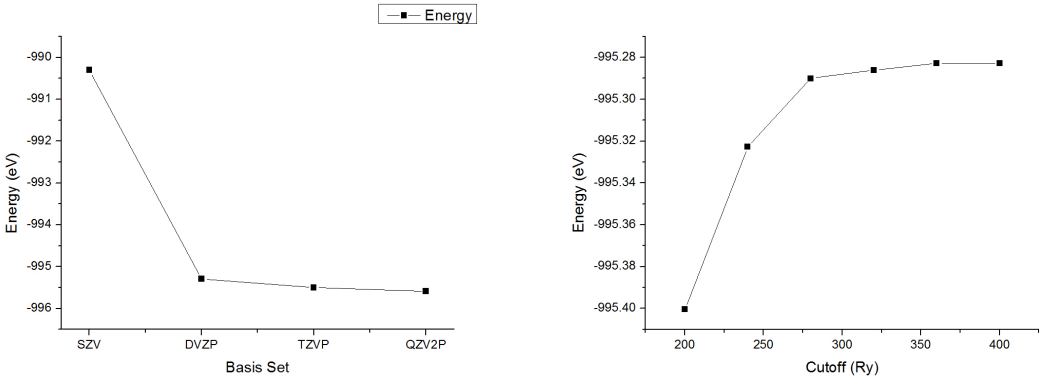


Figure 3.5: The application of colour charges to Li_2O: red circles represent oxygen, dark and light blue circles represent +1 and -1 colour charged lithium, respectively.



(a) (b)

Figure 3.6: Convergence testing for (a) the plane wave cut-off energy and (b) the basis set size.

The values used are as follows:

Interaction	A (eV)	ρ (Å)	C (eV Å^6)
Li^+/ Li^+	0.0	1.0	0.0
O^{2-}/ Li^+	653.84	0.285723	0.0
O^{2-}/ O^{2-}	0.0	1.0	76.651

Table 3.2: Pairwise potential parameters for Li_2O using the Buckingham potential. All with cutoff of 12 Å.

All of the MD and NEMD simulations performed used the Gaussian isokinetic thermostat. Details of the non-equilibrium method are outlined in Section 2.12. The time duration of the each simulation was 50 ps when DFT was used and 500 ps when classical force fields were used. In the case of NEMD simulations the colour field was applied after an initial equilibration period.

3.3.1 Density Functional Theory

The charge densities and the Mulliken populations (Section 2.7.7) were calculated using CASTEP (Clark et al., 2005). CASTEP implements the Kohn-Sham formalism (Kohn and Sham, 1965) and the Hohenberg-Kohn theories (Hohenberg and Kohn, 1964), as described in Section 2.7. CASTEP uses a combination of plane-waves (Payne et al., 1992) and ultra-soft pseudopotentials to describe the valence and core electrons respectively. In calculating using pseudopotentials the plane-wave cut-off energy, fine-grid-max spacing, and the k-point grid-spacing were varied independently of each other until the forces and energies on all atoms converged to within tolerances of 0.01 eV Å^{-1} and 0.1 eV, respectively. The Perdew-Burke-Ernzerhof exchange-correlation functional was used for all calculations (Perdew et al., 1996). The calculation of Mulliken populations and charge analysis have been implemented in CASTEP by Segall et al. (1996a,b). The plane-wave basis set is non-local by nature and therefore information regarding the localization of electrons or charge density is not directly available. In order to perform a population analysis, the plane-wave states must be projected onto a localized-basis set instantaneous(Sanchez-Portal et al., 1995). The projected local states can then be used in a Mulliken analysis for the population of orbitals and bonds and thus the effective charge (Mulliken, 1955).

3.4 Equilibrium Molecular Dynamics

Before using non-equilibrium molecular dynamics it is important to test equilibrium molecular dynamics to find its limitations. This should allow for a comparison of both macroscopic and microscopic properties between MD and NEMD.

Li_2O was simulated at four temperatures 973, 1123, 1273, and 1473 K using the FF-MD method for a simulation time of 500 ps. These temperature choices mean the superionic and the non-superionic regions are each sampled twice. Previous MD-based studies have managed to model the superionic region at high temperatures, but fail to reproduce the experimentally observed diffusion in the non-superionic region at low temperatures. Given there is no colour field present, the supercells do not benefit from being anisotropic and were chosen to consist of a 4x4x4 array of unit cells. The mean-squared displacement was measured for each temperature and the results are shown in Fig. 3.7. As described in Section 2.12.3 the gradient of the mean-squared displacement against time is proportional to the diffusion coefficient by way of the Einstein-Sutherland relation.

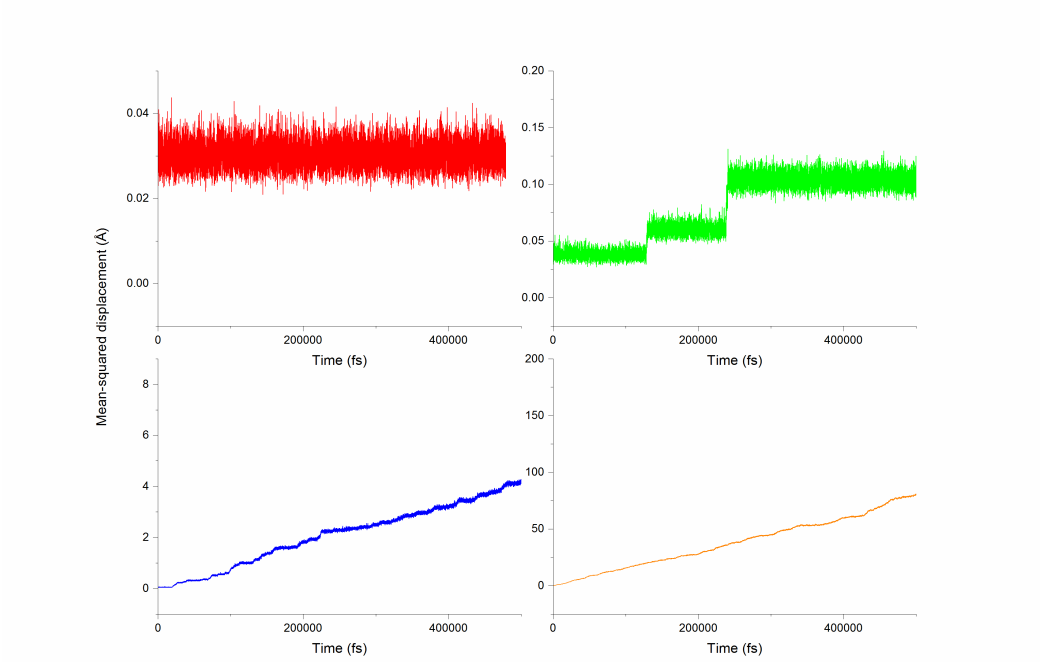


Figure 3.7: The mean-squared displacement of 4x4x4 Li_2O simulated as a function of time. The red, green, blue, and orange represent simulation temperatures of 973, 1123, 1273 and 1473 K respectively.

Clearly the high temperature simulations (1273 and 1473 K), in the superionic regime, show many diffusion events. This leads to a nearly linear relationship between mean-squared displacement and time. However at 1123 K only three diffusion events occur and for 973 K no diffusion events happen over the entirety of the simulation. These FF-MD simulations clearly show that in the superionic regime there are plenty of diffusion events, so the resulting diffusion coefficients have a significant level of precision whereas in the non-superionic regime there are too few diffusion events occurring to yield a meaningful diffusion coefficient, despite the use of a long simulation time. This rules out any reasonable comparison to experimental data. Also, the relatively small number of events makes studying mechanistic details troublesome, as the sample size is too small to be meaningful.

These results show the limitations of MD, even with very long simulation times. The fundamental issue with using equilibrium MD to model solid state diffusion for non-superionic diffusion rates is that the timescale of diffusion events is significantly longer than the timescale accessible with MD. The rate of diffusion will vary by many orders of magnitude over a few hundred kelvin and although the timescale of MD simulations can be increased with greater computational resources, increases in computational resources by orders of magnitude are not feasible. This limits MD diffusion studies to small temperature ranges that may not include the points of interest in the temperature dependence of the diffusion coefficients.

3.5 Non-equilibrium Molecular Dynamics

In order to increase the temperature range accessible with MD-based methods NEMD is used, as described in Sections 2.12.3 and 3.3. Two initial NEMD simulations were performed on Li_2O at 1273 K, one using force fields and the other using DFT. This allows a direct comparison and also a comparison to result of the FF-MD simulations. The NEMD calculations were performed with the methods outlined in Section 2.12. However, for the first NEMD simulation presented the process of setting up the different simulations and the extraction of self-diffusion coefficients will be presented in detail. Subsequent NEMD simulations shall be presented with more brevity.

The simulations were set up as described in Section 3.3. A diffusion coefficient can be calculated from a single simulation performed at a single colour-field magnitude. However, in order to be valid the value of the colour-field strength must lie in the linear regime, so the boundary of the linear regime must be previously known or has to be determined. A range of colour-field strengths were simulated starting at $0.02\,\mathrm{eV\,\AA^{-1}}$. This value was chosen as it is similar to the values used by

Aeberhard et al. (2012) for NEMD simulations on $LiBH_4$. The field strength was then varied to determine the width of the linear regime.

For the FF-MD simulation the lithium self-diffusion coefficient was calculated using the Einstein-Sutherland relation (Eqn. 2.30). For the NEMD simulations the diffusion coefficient was calculated using the method outlined in Section 2.12.3.

3.5.1 FF-NEMD Simulation at 1273 K

The simulations performed at 1273 K followed the setup as outlined in Section 3.3. The starting structure of Li_2O as defined in Section 3.1 was a 2x2x8 supercell and was subjected to an initial equilibration period of 30 ps using the Gaussian-isokinetic thermostat. The resulting state was used as the initial input for all the NEMD simulations performed. The NEMD simulations were performed at a range of colour-field strengths. Each of the simulations was performed for 250,000 time steps each of length 2 fs, giving a total simulation time of 500 ps. In this instance the colour-field strengths used were: 0.025, 0.05, 0.075, and $0.1\,\mathrm{eV\,\AA^{-1}}$. The response to the external field is shown in Fig. 3.8. Unsurprisingly, the larger the external colour field, the greater the response.

The steady-state average flux $\langle J_c(t)\rangle$ is measured by fitting a straight line to the response as shown in Section 2.12.3. The relevant equation 2.146 is stated again as a reminder:

$$\int_0^t \mathrm{d}t\ \langle J_c(t)\rangle\, VF_e = F_e \sum_{i=1}^{N} c_i \Delta r_i(t).$$

The self-diffusion coefficient is calculated using Eqn. 2.139, again restated:

$$D = \frac{k_b T}{\rho_c} \lim_{t\to\infty} \lim_{F_e\to 0} \frac{\langle J_c(t)\rangle}{F_e}.$$

The self-diffusion coefficient is calculated by fitting a straight line to the time-averaged responses against colour field that goes through the origin (Fig. 3.9). The main source of error in this method for calculating the self-diffusion coefficient is the measurement of the steady-state average flux. This is due to the form of the response. For self-diffusion in liquids and gases the running-average response is continuous, whereas in the solid state the diffusion consists of a series of hops over a specific distances. This leads to a response resembling a sort of step function. Fitting a straight line to such a response can lead to large errors if the number of events, i.e. steps, is small. This

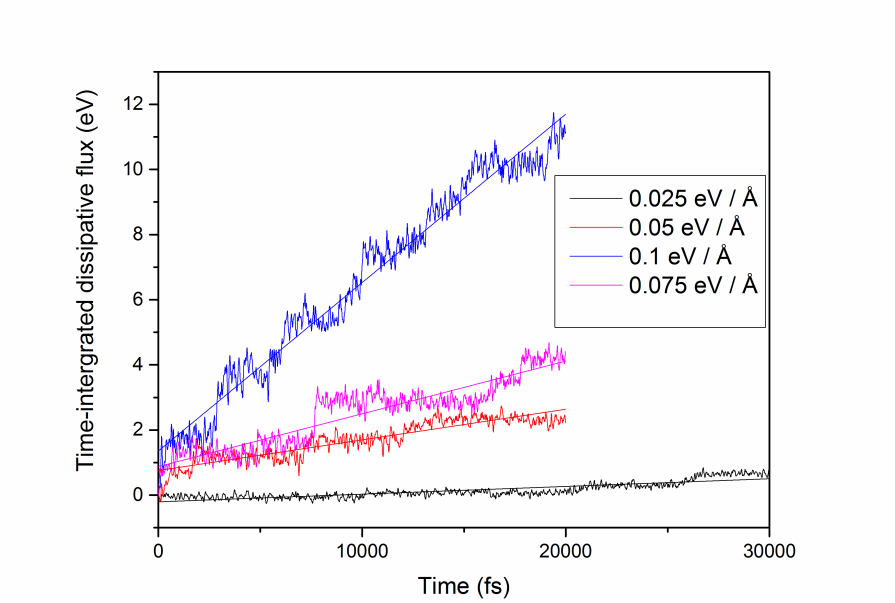


Figure 3.8: The time-integrated dissipative flux (Eqn. 2.146) plotted against time showing the magnitude and time dependence of the response to colour fields of varying strength. A straight line is fitted through the origin to measure the steady-state average flux $\langle J_c(t)\rangle$.

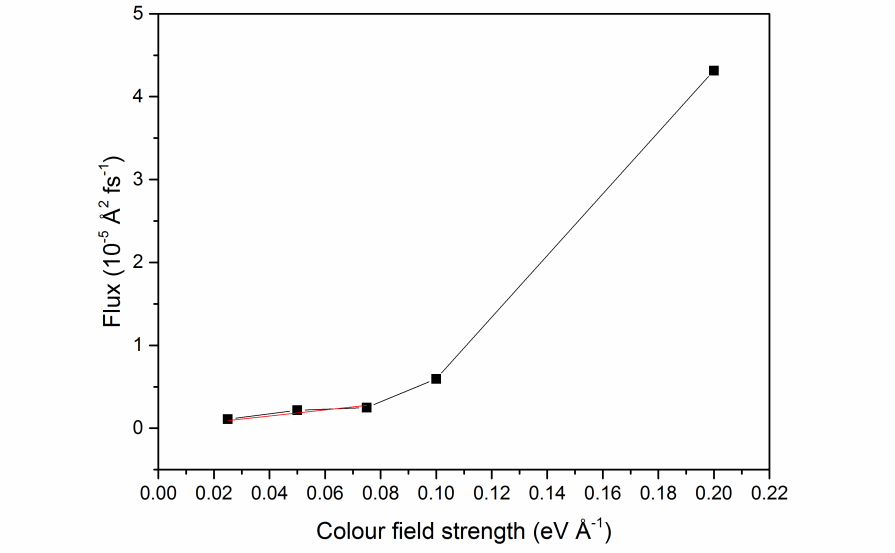


Figure 3.9: The time-averaged response to the colour field plotted against the strength of the colour field, solid squares. The interconnecting straight black lines are guides for the eye only. The red line represents the fitting of a straight line, through the origin, to the points in the linear regime.

source of error decreases proportionally to the square root of the number of diffusion events. The other main source of error in the NEMD method used in this thesis is the introduction of non-linear responses and effects due to the application of the external field.

3.5.2 Comparison of Computational Methods at 1273 K

The initial temperature simulated was chosen to be 1273 K. This temperature lies in the superionic region where the rate of diffusion is elevated. As can be seen in Fig. 3.7 at 1273 K there are a significant number of diffusion events during the duration of the MD simulation time, enough to calculate a self-diffusion coefficient with a reasonable error. For FF-MD simulations at lower temperatures the self-diffusion coefficient cannot be determined with any real accuracy. The DFT-NEMD simulation was setup in the same manner as the FF-NEMD simulation, but with both a shorter simulation time of 50 ps and a shorter initial equilibration period of 10 ps, as the computational cost of DFT is much greater. The self-diffusion coefficients calculated from these three different methods are shown in Table 3.3. There is a reasonable level of agreement between the three methods and, more importantly, significant agreement with the experimental data from Oishi and Kamei (1979). Note that there is a 39 K difference between the simulation temperature and the experimental temperature of the diffusion coefficient in Table 3.3. The temperature dependence of both experimental and computational self-diffusion coefficients is covered in greater detail later.

The associated error was smallest for FF-NEMD and largest for DFT-NEMD. This is because the simulation time of DFT-NEMD is an order of magnitude lower than that of the FF-MD and FF-NEMD methods, which have the same simulation times. The error in FF-NEMD is smaller than FF-MD due to the application of the colour field and therefore a greater number of diffusion events is observed, which in turn reduces the error. Also to be noted from the agreement in values between FF-NEMD and DFT-NEMD is the transferability of the potential parameters determined by Fracchia et al. (1998). However, the main difference between FF-NEMD and DFT-NEMD is

Method	$\log D_{Li}/\mathrm{cm}^2\,\mathrm{s}^{-1}$	Simulation Time / ps
FF-MD	-5.96 ± 0.05	500
FF-NEMD	-6.18 ± 0.03	500
DFT-NEMD	-6.02 ± 0.08	50
Oishi et al.	-6.23	-

Table 3.3: Lithium self-diffusion coefficients obtained from different computational methods at 1273 K. The experimental result obtained from Oishi and Kamei (1979) was measured at 1312 K.

the computational efficiency; DFT-NEMD requires high-performance computing resources whereas FF-NEMD can be run on single-core machines. Due to the lower computational cost per timestep, FF-NEMD gives access to much longer simulation times and a more thorough sampling of the linear regime. The difference in computational efficiency between FF-MD and FF-NEMD is insignificant as the rate determining step in both methods is the calculation of forces. The added computations due to the colour-field algorithm are not the limiting factor. Due to both the computational efficiency and accuracy, FF-NEMD is the method of choice used to study Li_2O over a wide range of temperatures.

Along with the agreement between the self-diffusion coefficients determined from the three different computational methods, the mechanistic detail observed using all three methods was similar, as will be discussed in Section 3.5.3.

3.5.3 Temperature Dependence of Self-diffusion Coefficient

Using the FF-NEMD method, simulations were performed at six further temperatures: 873, 973, and 1123 K, which are in the non-superionic regime, and 1373, 1473, and 1603 K, which are in the superionic regime. The FF-NEMD calculated self-diffusion coefficients are shown in Fig. 3.10, along with the results from FF-MD and the experimental data of Oishi and Kamei (1979). There is very good agreement between the experimental results and the FF-NEMD calculations over the entire temperature range simulated, despite the self-diffusion coefficient varying by more than four orders of magnitude. The results of the FF-MD calculations agree very well, akin to the agreement with FF-NEMD, at high temperatures above 1250 K. However at lower temperatures the agreement is very poor. The error in the calculated self-diffusion coefficient increases as the temperature decreases for both FF-MD and FF-NEMD due to the decrease in the number of hopping events. The FF-MD simulation performed at 973 K produced no diffusion hopping events. The value of $D_{Li} \approx 10^{-11}\,\mathrm{cm^2\,s^{-1}}$ is indistinguishable from zero. It is only included in Fig. 3.10 to indicate the sensitivity limits of the FF-MD method.

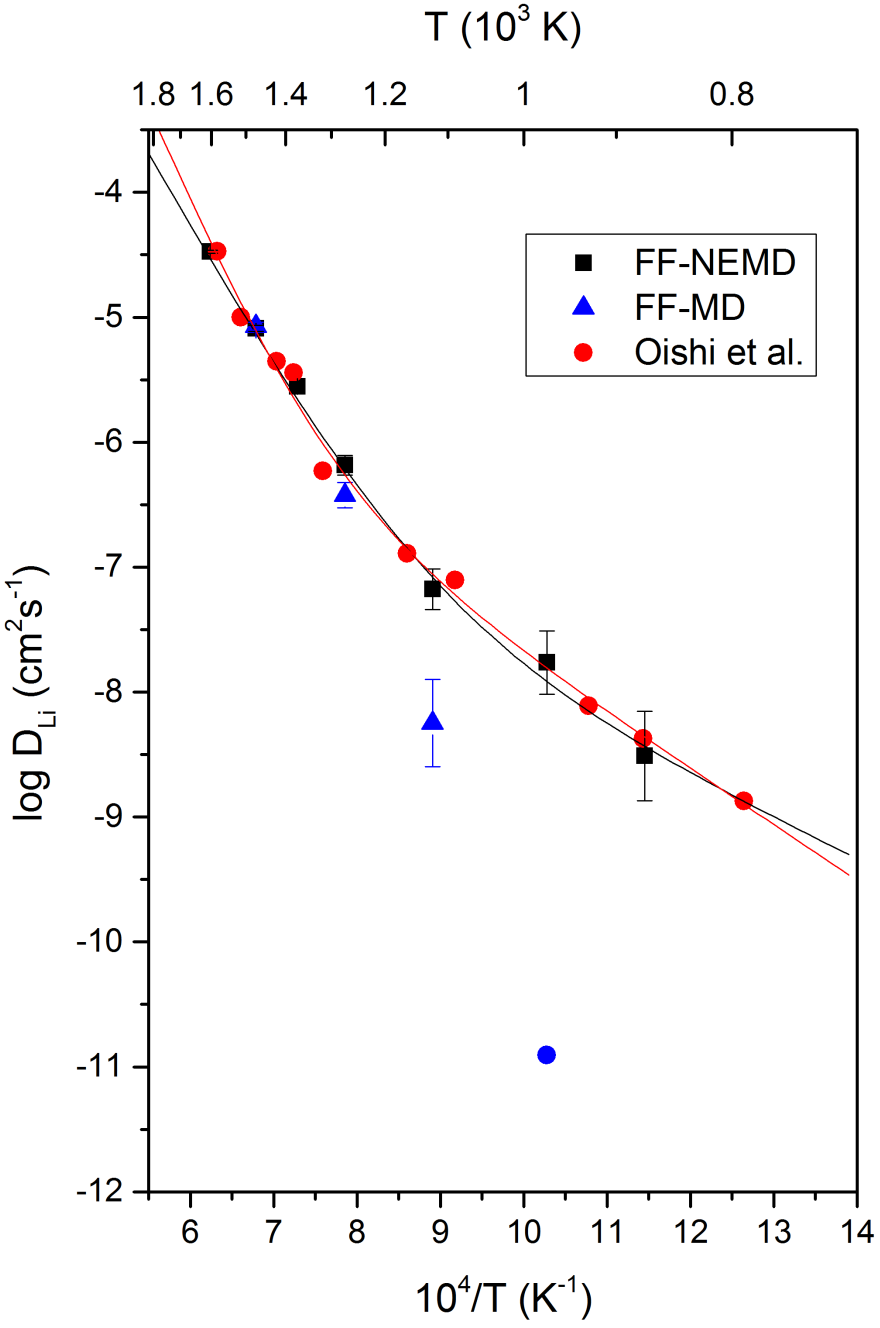
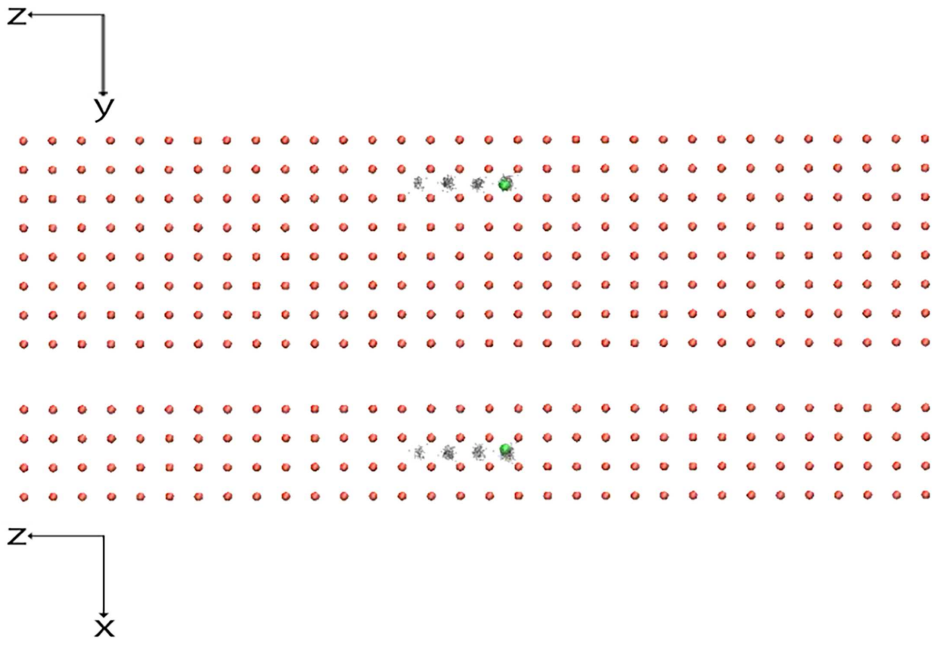


Figure 3.10: Temperature dependence of the Li^+ diffusion coefficient in Li_2O. Red circles represent values from Oishi and Kamei (1979); black squares represent values from FF-NEMD simulations; blue triangles and the blue circle represent values from FF-MD simulations. The red and black lines are fits to Eqn. 3.2 for the experimental and FF-NEMD simulated data, respectively.

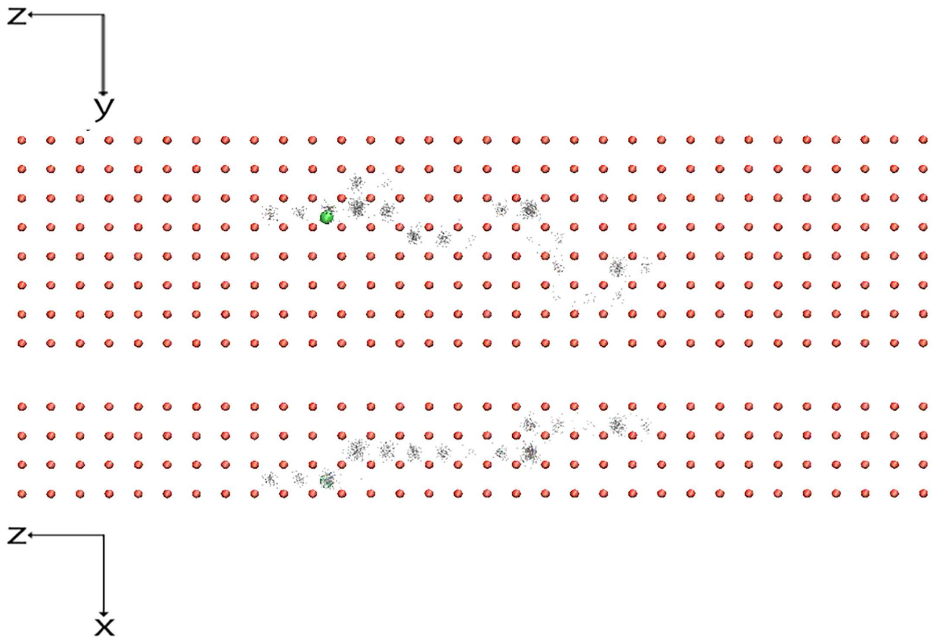
The temperature dependence of the lithium self-diffusion coefficient shows an increase in gradient above ~1273 K. Using the Arrhenius model (Section 2.4) the change in gradient can be interpreted as a change in the activation energy and would imply a change in the underlying diffusion process or, if multiple diffusion mechanisms are present, a change in the dominant process. The dominant microscopic diffusion process responsible for the macroscopic diffusion at a given temperature can be found in the individual lithium trajectories. The trace of a single lithium atom from an entire simulation (490 ps) is shown in Fig. 3.11 for two simulation temperatures. These traces illustrate how the individual microscopic diffusion events cause the macroscopic diffusion. The trace at 973 K shows movement of the lithium between nearest-neighbour sites forming a straight line parallel to the colour field (001). There is no significant displacement in the plane orthogonal to the direction of the colour field. At 973 K, an individual lithium atom does not move far during the simulation, whereas at 1373 K there is a significant net displacement. The trace at 1373 K shows a lot of hopping between nearest neighbour sites parallel to the direction of the colour field, similar to the 973 K trace. There is also movement between sites perpendicular to the colour field. These hops consist both of nearest-neighbour hops moving along the $\langle 100 \rangle$ directions and hops between next-nearest-neighbour sites. Appendix I contains movies of the traces in Fig. 3.11 showing the movement of the specific lithium over time, see Movies 3.1† and 3.2† for traces shown in Figures 3.11a and 3.11b, respectively. The movies show the lithium atom moving in the $[00\bar{1}]$ direction despite the colour field being applied along the [001] direction. This should be expected as half of the lithium atoms have a -1 colour charge label and would be expected to move along the $[00\bar{1}]$ direction over time due to the interaction with the colour field.

In the non-superionic regime the hopping is much less frequent than in the superionic regime. From Fig. 3.11 it is clear that in same time period (490 ps) the lithium atom has traveled between three regular lithium sites parallel to the colour field, whereas in the superionic regime the lithium traveled between 14 regular lithium sites. If we consider the FF-MD simulation performed at 973 K and the resulting mean-squared displacement for all lithium atoms (Fig. 3.7), there were no lithium diffusion hops at all, but with FF-NEMD one lithium atom hopped three times in the same time period. This highlights the effectiveness of FF-NEMD. The difference in distance travelled by an individual lithium atom illustrates the much smaller error associated with the self-diffusion

† Attached in the back cover is a CD that contains movies of diffusion referred to in this thesis. The captions for these movies can be found in Appendix I.



(a)



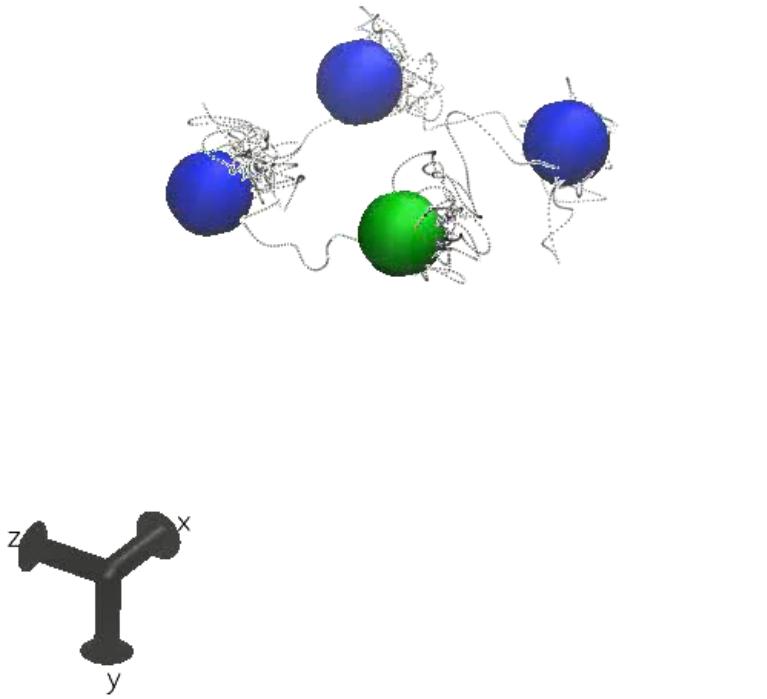
(b)

Figure 3.11: Traces showing diffusion of one Li^+ cation (green) through the oxide sublattice (red), over a time of 490 ps (a) at 973 K and (b) at 1373 K. The upper (lower) part of both (a) and (b) is projected along [100] ([010]). Each black point in the trace represents a time window of 200 fs.

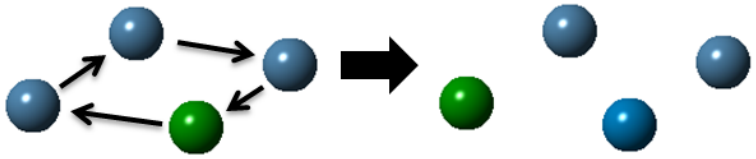
coefficients measured with FF-NEMD in the superionic regime compared to the non-superionic regime (Fig. 3.10) as the error of the self-diffusion coefficient is proportional to $\sqrt{N}/N$ where N is the number of hops throughout the entire simulation for all lithium atoms.

The dominant diffusion mechanism in the non-superionic regime is the nearest-neighbour (nn) mechanism. The lithium atom proceeds via a direct hop between nearest-neighbour regular lithium sites of separation $a/2$. There is little discernible movement in the plane perpendicular to the direction of the hop. The nn mechanism always involved four neighboring lithium sites, forming a closed loop. This is illustrated in Movie 3.3† and Fig. 3.12, which shows one of the hops shown in Movie 3.1†. This nn mechanism is the dominant mechanism in the non-superionic regime and it is observed at all temperatures simulated, but in the superionic regime it becomes significantly less prevalent. The concerted nature of this mechanism allows for diffusion without the need for a cation vacancy on the regular site i.e. no movement of a lithium to an interstitial site. Despite the nn mechanism being the main source of diffusion in the non-superionic regime there is a limited amount of diffusion initiated by movement of a lithium along $\langle 111 \rangle$ to the octahedral-interstitial site at $\left(\frac{1}{2}, \frac{1}{2}, \frac{1}{2}\right)$ of the unit cell that can be seen in Fig. 3.1b. The occupation of the octahedral-interstitial site creates a vacancy on the regular lithium lattice. This vacancy can then rapidly diffuse throughout the structure by a series of $\langle 100 \rangle$ hops between nearest-neighbour sites until the lithium on an interstitial site returns to the regular lattice, recombining with the vacancy and thus terminating the diffusion mechanism. In the low temperature region this interstitial-mediated diffusion mechanism involves four regular sites forming a square. This is illustrated in Movie 3.4† and Fig. 3.13. The maximum residence time of the octahedral interstitial site is 400 fs.

With increasing temperature the octahedral-interstitial mechanism begins to dominate the diffusion and the nn mechanism becomes much less significant. At low temperatures the octahedral-interstitial mechanism involves four cations moving, but at high temperatures the number of cations moving increases to typically 12 or 14. This is due to the increase in the maximum residence time of the interstitial site of up to 4 ps. This allows for many more $\langle 100 \rangle$ hops between adjacent sites to occur. Although the vast majority of lithium movements consists of $\langle 100 \rangle$ hops, a small number of $\langle 110 \rangle$ hops are also observed. Movie 3.5† and Fig. 3.14 shows the octahedral-interstitial mechanism operating at high temperatures; a $\langle 110 \rangle$ hop occurs during the course of the movie.

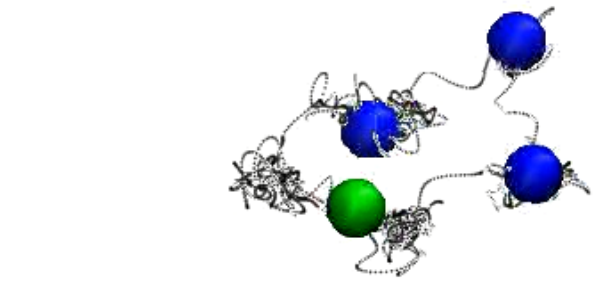


(a)



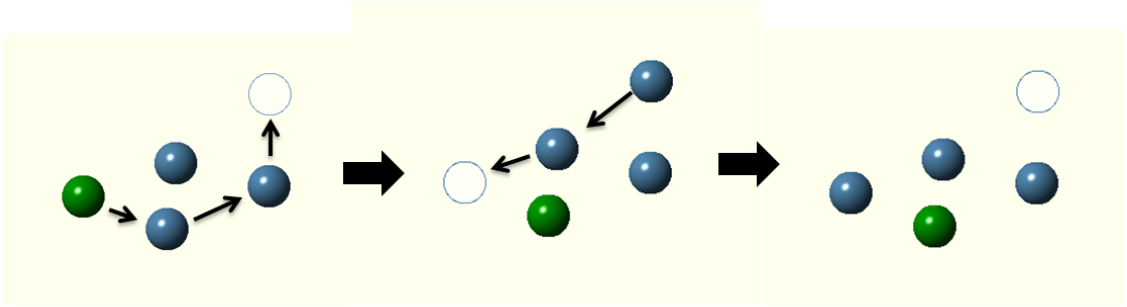
(b)

Figure 3.12: A concerted nearest-neighbour (nn) mechanism. (a) Traces showing the diffusion of Li^+ cations. The green sphere is the Li^+ cation shown in Movie 3.1† and Fig. 3.11a at 973 K. The blue spheres are neighbouring Li^+ cations involved in the diffusion mechanism. Each black point in the trace represents a time window of 2 fs. (b) Graphical depiction of the motion of atoms.



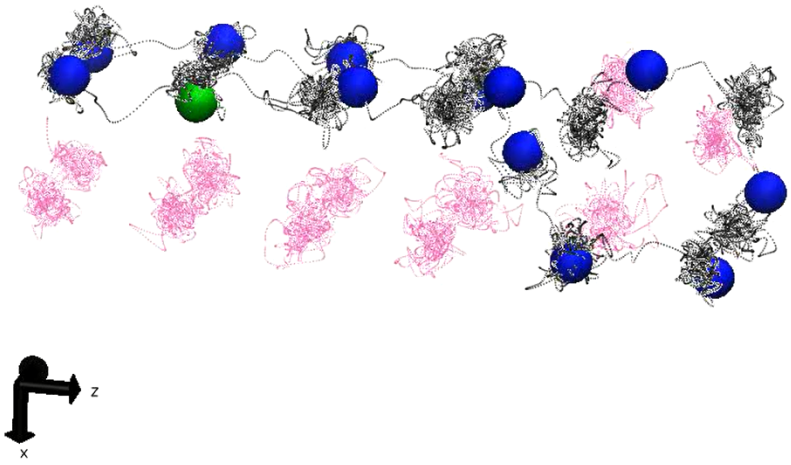


(a)

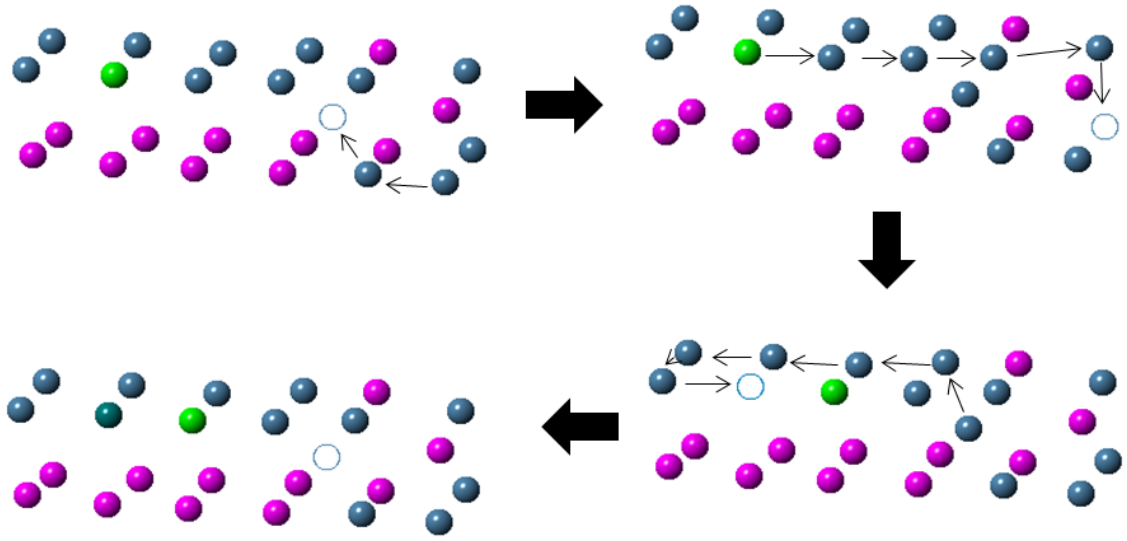


(b)

Figure 3.13: The octahedral interstitial mechanism operating in the low temperature regime. (a) Traces showing the diffusion of Li^+ cations. The green sphere is the Li^+ cation shown in Movie 3.1† and Fig. 3.11a at 973 K. The blue spheres are neighbouring Li^+ cations involved in the diffusion mechanism. Each black point in the trace represents a time window of 2 fs. (b) Graphical depiction of the motion of atoms.



(a)



(b)

Figure 3.14: The octahedral-interstitial mechanism operating in the high-temperature region involving a ⟨110⟩ hop also occurs. (a) Traces showing the diffusion of Li^+ cations. The green sphere is the Li^+ cation shown in Movie 3.2† and Fig. 3.11b at 1373 K. The blue spheres are neighbouring Li^+ cations involved in the diffusion mechanism. The black points in the trace represents a time window of 2 fs. The pink points represent neighbouring Li^+ cations not involved in the diffusion mechanism but added for clarity. Each point represents a time window of 2 fs. (b) Graphical depiction of the motion of atoms.

The temperature dependence of the diffusion coefficient is shown in Fig. 3.10 and has a smooth increase in gradient around $\sim 1200\,\mathrm{K}$ as the system moves from non-superionicity to superionicity. The superionic regime is dominated by the octahedral-interstitial mechanism, with the concerted nearest-neighbour mechanism being a minor contributor. The opposite situation is observed in the non-superionic regime. The increase in the frequency of octahedral-interstitial mechanisms with increasing temperature is consistent with the fractional occupation of the octahedral-interstitial site as measured by neutron diffraction (Farley et al., 1991). This showed a rapid increase in the occupation of the interstitial site above 1200 K. The temperature dependence of the lithium diffusion coefficient presented by Oishi and Kamei (1979) was described by the Arrhenius equation (Section 2.4) with two sets of values for the activation energy and the attempt frequency i.e. each of the superionic and non-superionic regimes was described by a straight line, with the lines intersecting near 1273 K. It is clear from Fig. 3.10 that the temperature dependence changes gradually between the two regimes; there is no discontinuity. The temperature dependence of the diffusion coefficients, for both the the FF-NEMD values and the experimental results (Oishi and Kamei, 1979), was therefore fitted to the function:

$$\log D_{Li} = \log\left(\exp\left[k_1 - \frac{\Delta E_1}{k_B T}\right] + \exp\left[k_2 - \frac{\Delta E_2}{k_B T}\right]\right) \tag{3.2}$$

where the subscripts 1 and 2 correspond to the nearest-neighbour and the octahedral-interstitial mechanisms, respectively. The values of the activation energy, ΔE_i, and attempt frequency, k_i, are tabulated in Table 3.4. It is clear from both Fig. 3.10 and the fitted values that the agreement

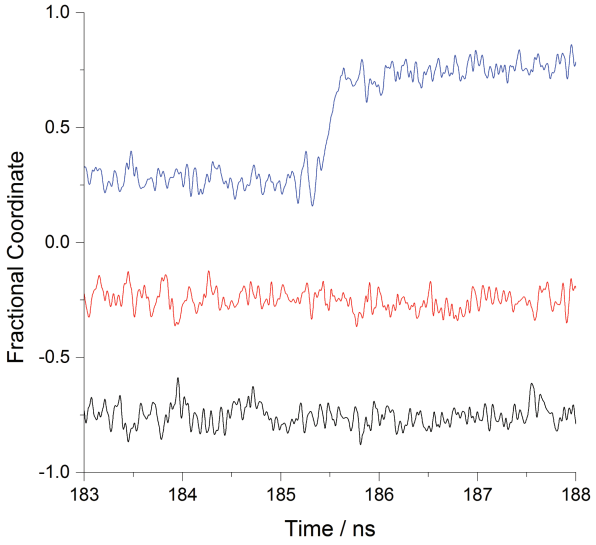
Method	FF-NEMD	Oishi et al.
k_1	-4.81 ± 0.13	-3.25 ± 0.13
k_2	2.91 ± 0.80	5.43 ± 0.80
$\Delta E_1 / \mathrm{kJ\,mol^{-1}}$	26.9 ± 1.5	37.2 ± 1.0
$\Delta E_2 / \mathrm{kJ\,mol^{-1}}$	100 ± 6.7	134 ± 6.7

Table 3.4: Parameters derived in fitting experimental and simulated diffusion coefficients to Eqn. 3.2

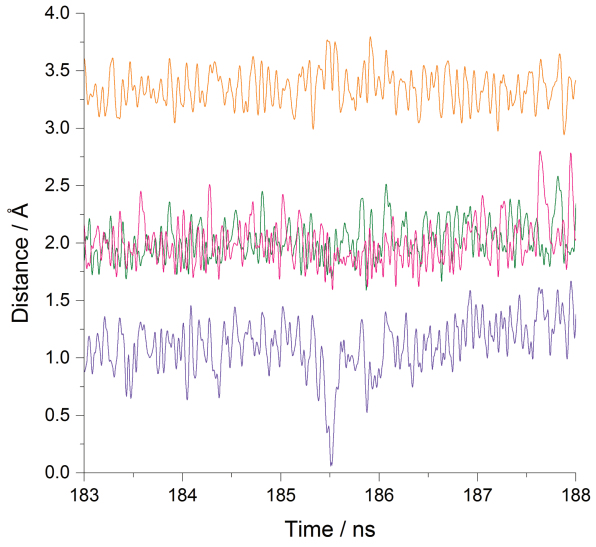
between the experimental and computational results is excellent across a wide temperature range. The activation energy of the octahedral-interstitial mechanism is much greater than the activation energy of the nearest-neighbour mechanism. This difference explains why the octahedral-interstitial mechanism is rarely observed at lower temperatures. The values of k_1 and k_2 are consistent with

the observation that the octahedral-interstitial mechanism becomes more important at higher temperatures as the ratio $\Delta E_i/k_BT$ decreases. The difference between the activation energies of the two mechanisms is consistent with the details of the different paths taken. For a nearest-neighbour hop the lithium atom proceeds through the edge of an oxide tetrahedron along [001] whereas in the octahedral-interstitial mechanism the lithium moves through the less-crowded triangular face of the oxide tetrahedron; more details are presented below. Despite the good agreement between the diffusion coefficients calculated by FF-NEMD and determined experimentally by Oishi and Kamei (1979), their fitted parameters do differ. This shows how sensitive the derived parameters are to the function to which they are fitted. It would be reasonable to consider adding more terms to the function Eqn. 3.2. Although two principal classes of diffusion mechanisms have been observed there are subtle variations within each, as would be expected from a process driven by thermal motion. For example, some events involve a [110] hop.

Fig. 3.15a shows the coordinates of a lithium cation as it proceed along a nearest neighbour [001] hop. The linear path between two regular lattice sites proceeds through the edge of an oxide tetrahedron (Fig. 3.1a). The edge of the oxide tetrahedron is $a_0/\sqrt{2} \approx 3.25\,\text{Å}$ in length. This would make the Li - O distance at the midpoint of the [001] hop $\sim 1.63\,\text{Å}$, which is clearly chemically unreasonable. The time dependence of the O - O and the Li - O distances was therefore studied more closely, see Fig. 3.15b. It is clear that the lithium does not move along a linear path, as the two Li - O distances are reasonably constant before, during, and after the hop. Also Fig. 3.15a shows movement in the z direction by $a_0/2$ and there is some limited movement in the plane perpendicular to the direction of the hop. The distance between the moving lithium and the instantaneous midpoint of the O - O vector (Fig. 3.15b) shows the lithium passing close to, but not through, the midpoint. The average minimum distance between the lithium and O - O vector midpoint during a hop is 0.017(12) Å and the lowest value observed was 0.0059 Å. The oxide ion separation also remains essentially constant throughout and the standard deviation of the O - O separation from its mean value is 0.16 Å in a 1.5 ps time window centred on the nn hop and 0.17 Å over the entire simulation. The angle formed by the three atoms involved in the nn hop, O - Li - O, should reach 180° if the lithium passes directly through the oxide tetrahedron edge. The absolute value of the deviation, $|\delta|$, for the O - Li - O angle from 180° is shown in Fig. 3.16. Both before and after the nn hop occurring at $\sim 185.5\,\text{ps}$ the deviation is $\sim 70.5°$ as the angle of O - Li - O when all atoms are on their regular lattice sites is approximately $(180° - 70.5°) = 109.5°$. During the hop the deviation nears 0° but



(a)



(b)

Figure 3.15: The trajectories of a Li^+ cation at 973 K simulated with FF-NEMD; (a) the black, red, and blue lines represent the x, y and z fractional coordinates, respectively, of the cation for the nn mechanism along [001]. (b) The orange line shows the separation of the two oxide ions between which the cation passes. The pink and green lines show the two lithium-oxygen distances. The purple line shows the distance between the cation and the instantaneous midpoint of the two oxide ions.

never reaches it. The minimum value achieved is $\sim 4^{\circ}$.

The NEMD data shows the lithium atom passing very close to the midpoint of the O - O vector during a nn hop, but not perfectly through the middle. The simulations are performed at high temperatures and it is clear from Fig. 3.15a that there are plenty of high frequency oscillations about the ideal crystal positions. In order to study this point more closely the energy profiles for various possible nn trajectories were calculated using the nudged elastic band method implemented in CP2K (Henkelman et al., 2000; Henkelman and Jonsson, 2000; Trygubenko and Wales, 2004) and using the force-field as mentioned in Section 3.3. The nn hop was for a lithium atom moving towards a vacant regular lithium site in a 4x4x4 supercell with lattice parameters corresponding to 1273 K. Initially the coordinates of the hopping lithium atom orthogonal to the direction of motion were fixed to yield a straight (001) hop. Subsequent NEB calculations involved setting the coordinates of the lithium atom as it passes through the O - O vector away from the midpoint, thus forcing the lithium atom to take a curved trajectory around the midpoint. The results are shown in Fig. 3.17. The lowest energy barrier corresponds to the straight hop through the midpoint of the O - O vector. For all other trajectories, where the midpoint was avoided, the energy barrier was higher. The difference in energy barrier is very small suggesting a broad flat basin in the potential energy surface. This agrees with the MD data that shows the Li-ion trajectories follow a distribution of pathways centred about the midpoint.

The energy profile for the motion of a Li atom from a regular Li site along one of the $\langle 100 \rangle$, $\langle 110 \rangle$, and $\langle 111 \rangle$ directions towards a vacancy has previously been calculated using DFT by Gupta et al. (2012) using the lattice parameters associated with two different temperatures: one temperature corresponding to non-superionic rates of diffusion and one to superionic. The energy profile for movement along [100] is similar at both superionic and non-superionic temperatures, but the energy barrier is much lower for former, $\sim 0\,\mathrm{eV}$, than the latter, $0.3\,\mathrm{eV}$. The shape and size of the energy profile obtain by Gupta et al. (2012) is in good agreement with the energy profiles obtained using force-fields, further suggesting the force-field is a good representation of the interaction potential.

Similarly Fig. 3.18a and 3.18b show the coordinates and relevant interatomic separations of an octahedral-interstitial hop. The x, y and z coordinates of the mobile lithium ion each show a displacement of $a_0/4$ in the direction $[\bar{1}\bar{1}\bar{1}]$, to an octahedral-interstitial site. After an interstitial-residence time of $\sim 600\,\mathrm{fs}$ the lithium cation proceeds a distance of $a_0/4$ along $[\bar{1}11]$ and thus returns to a regular lithium lattice site. When the lithium proceeds to the six-coordinate octahedral site it

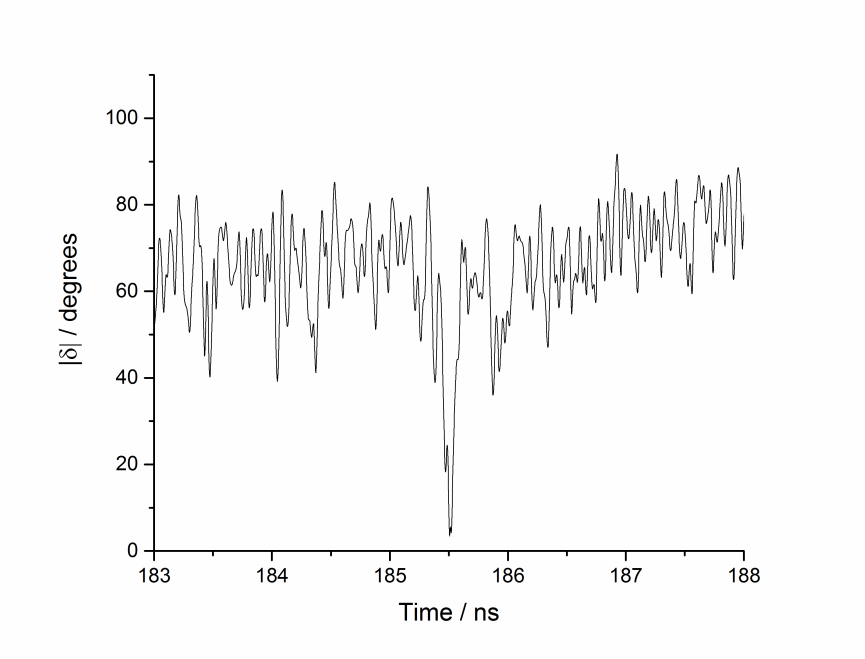


Figure 3.16: Time dependence of the absolute deviation from 180° of the O - Li - O angle, $|\delta|$, for the nearest neighbour [001] hop shown in Fig. 3.15a and 3.15b.

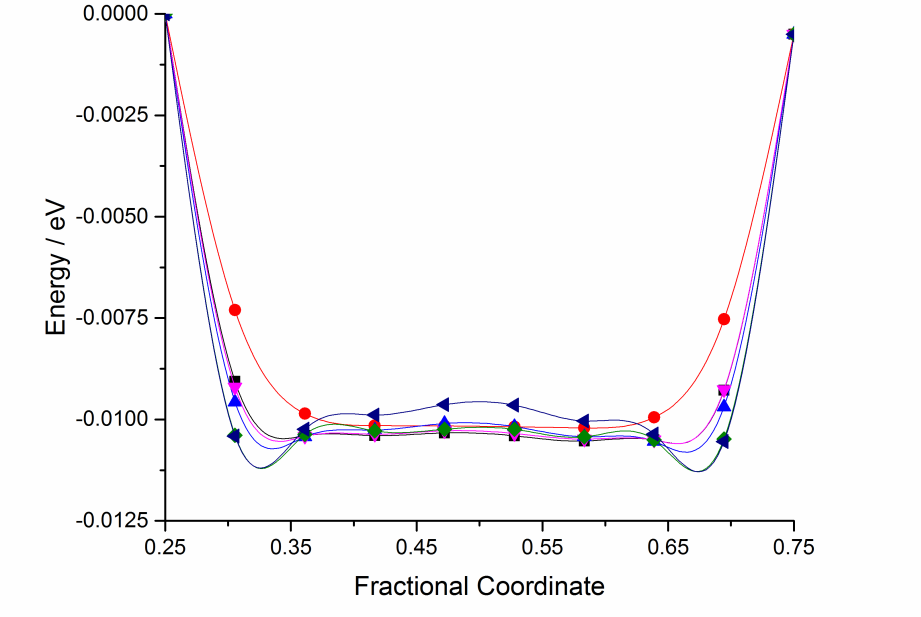


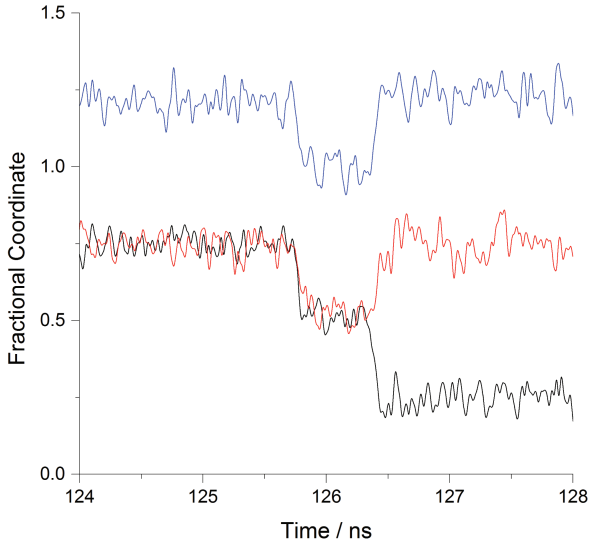
Figure 3.17: The energy profile for lithium ion movement along [001]. The black squares are for direct nn hop. The blue, green, red and purple represent curved trajectories avoiding the O-O vector midpoint.

passes through the equilateral triangular face of the oxide tetrahedron. The Li - O distance, in an undistorted structure when the lithium ion occupies the octahedral interstitial site is $a_0/2 \approx 2.3\,\text{Å}$. This distance is longer than expected for a typical six coordinate Li - O distance of approximately 2.08 Å (Battle et al., 2003). In order to accommodate the occupation of the octahedral-interstitial site the six surrounding oxide ions are displaced towards the interstitial site. The result is a mean Li - O distance of 2.14 Å after this displacement. Three of the O - O nearest neighbour distances of the oxide octahedron surrounding the lithium-interstitial site are shown in Fig. 3.18b. They show a decrease from a mean of 3.33 Å before and after the occupation of the interstitial site to 3.19 Å whilst the site is occupied.

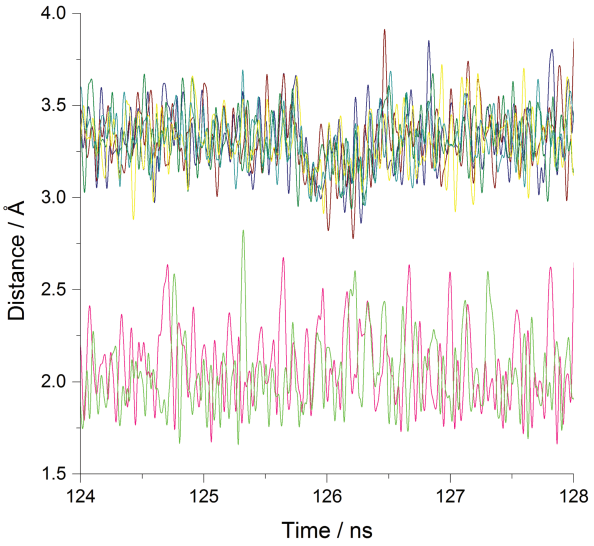
The occupied octahedral-interstitial site is a local energy minimum. A series of configurations were taken from NEMD trajectories where such a site is occupied and then submitted to a geometry optimisation. The site remained occupied upon geometry optimisation. The energy profile for the occupation of an octahedral-interstitial site and the subsequent diffusion of a regular site vacancy away from the interstitial were calculated using force-field NEB, as mentioned earlier (Fig. 3.19). The initial energy barrier of $\sim 1.8\,\text{eV}$ is a similar to the value obtained by Gupta et al. (2012) for movement of a single lithium atom along a $\langle 111 \rangle$ direction through a vacant octahedral-interstitial site. After the initial large energy increase a series of smaller barriers are as as result of the nn hops moving the vacancy away from the occupied interstitial.

For the octahedral-interstitial mechanism shown in Fig. 3.13 and Movie 3.3 the charge density was analysed. The atomic positions were generated from a FF-NEMD simulation and therefore the electron density was not determined. The atom positions used were from the midpoint of the process, when one of the lithium atoms occupies the octahedral-interstitial site and another is at the midpoint of an adjacent nearest-neighbour hop. The charge density and Mulliken charges were calculated using DFT methods as outlined in Section 3.3.1. For the octahedral-interstitial mechanism the lithium atom occupying the interstitial site has a charge of $0.25\,e$ and the six-coordinating oxygen atoms had an average charge of $-0.880 \pm 0.015\,e$. The lithium atom moving through the edge of the oxide tetrahedron has a charge of $0.42\,e$ and the two oxygen atoms forming the edge have a charge of $-0.89 \pm 0.01\,e$.

For comparison the charge density and Mulliken charges were also calculated using the crystal structure of Li_2O as shown in Fig. 3.1. The charge for the oxygen atoms in the ideal crystal was $-0.90\,e$ and for the lithium atoms $0.45\,e$. The calculation was repeated for a random timestep after



(a)



(b)

Figure 3.18: The trajectories of a Li^+ cation at 1273 K simulated with FF-NEMD; (a) the black, red, and blue lines represent the x, y and z fractional coordinates, respectively, of the cation as it follows the octahedral-interstitial mechanism along $[\bar{1}\bar{1}\bar{1}]$ to the interstitial site, then along $[\bar{1}11]$ to the final site; (b) The yellow, navy, dark red and olive lines show the four of the oxygen-oxygen distances around the interstitial site. The pink and green lines show the Li - O distances in the triangular window through which the cation passes.

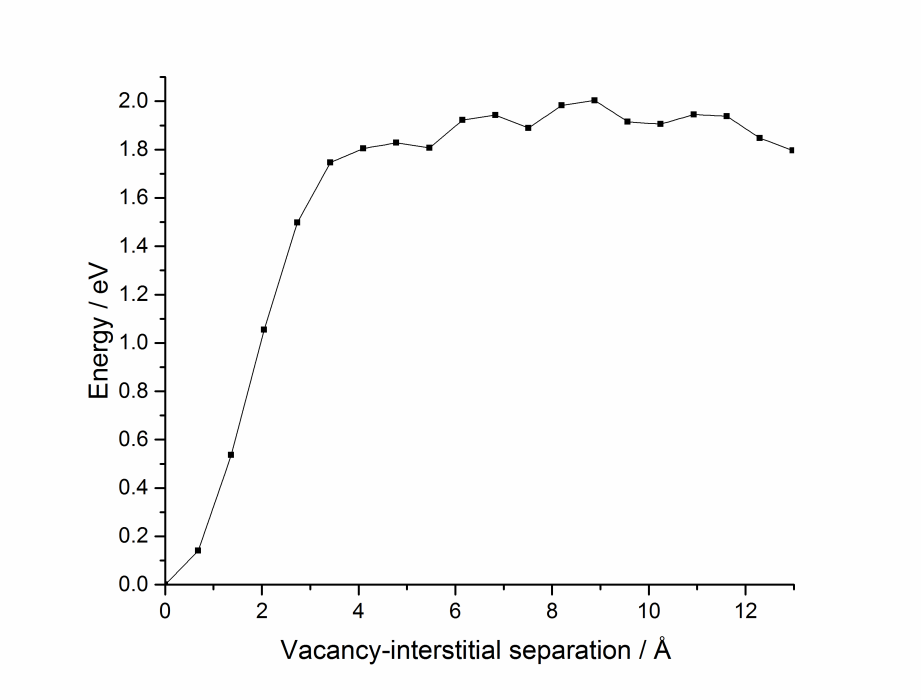


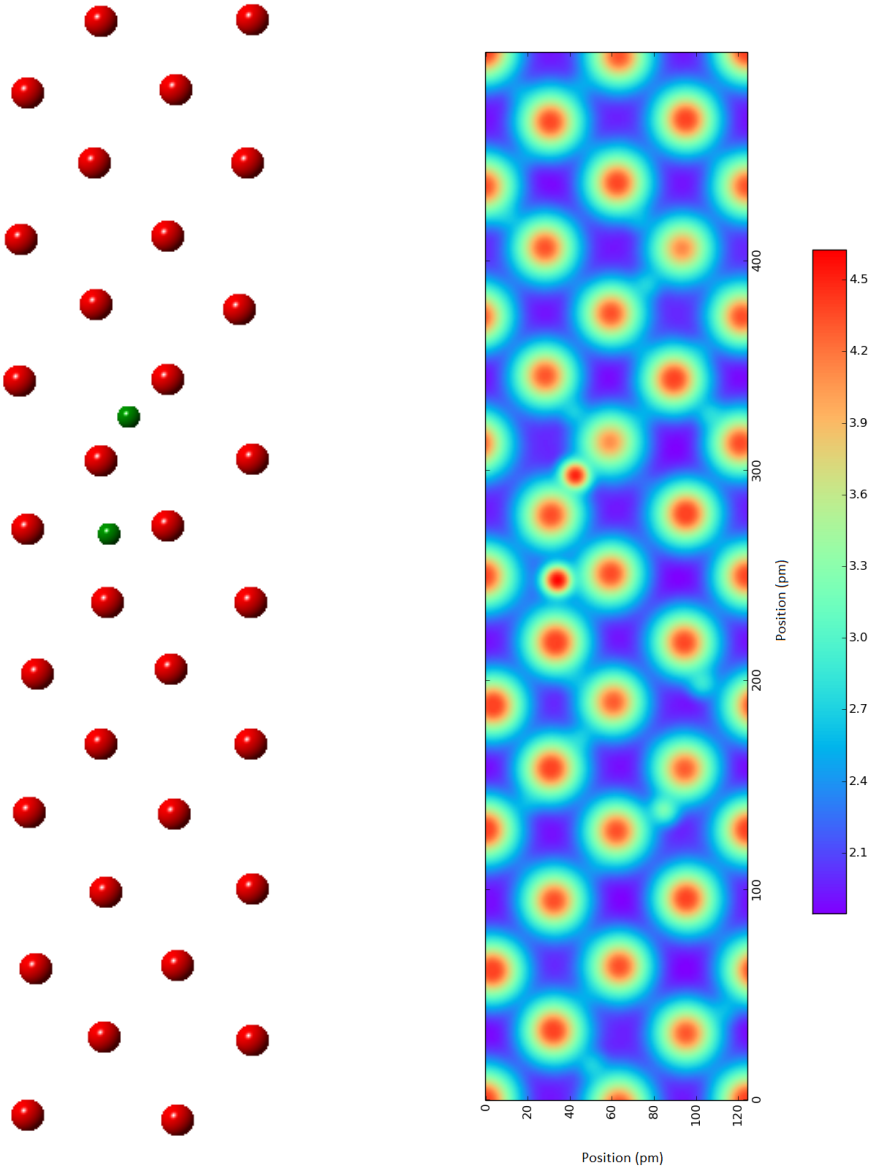
Figure 3.19: The energy profile for lithium ion movement along $\langle 111 \rangle$ and the subsequent diffusion of a vacant regular lithium site.

the system had reached equilibrium. The average charge for all lithium atoms was $0.446 \pm 0.044\,e$ and for the oxygen atoms $-0.892 \pm 0.014\,e$. The difference between the ideal crystal structure and the equilibrium values is due to the movement of individual atoms from their ideal positions due to thermal motion. However, in both systems there is overall charge neutrality.

The partial charge of the lithium atom occupying the octahedral-interstitial site is much lower than the partial charge of lithium atoms on their equilibrium positions. This is due to the increase in coordination of the lithium atom as it moves from the tetrahedrally-coordinated regular lattice site to the octahedrally-coordinated interstitial site. The extra coordinating oxygen atoms share electron density with the lithium atom and thus reduce the partial charge of the lithium atom. The six coordinating oxygen atoms have a similar partial charge to the oxygen atoms in the equilibrium system. For the lithium atom proceeding along a nearest-neighbour hop the partial charge is essentially unchanged from the equilibrium value. This is also the case for the two oxygen atoms between which the lithium atom passes.

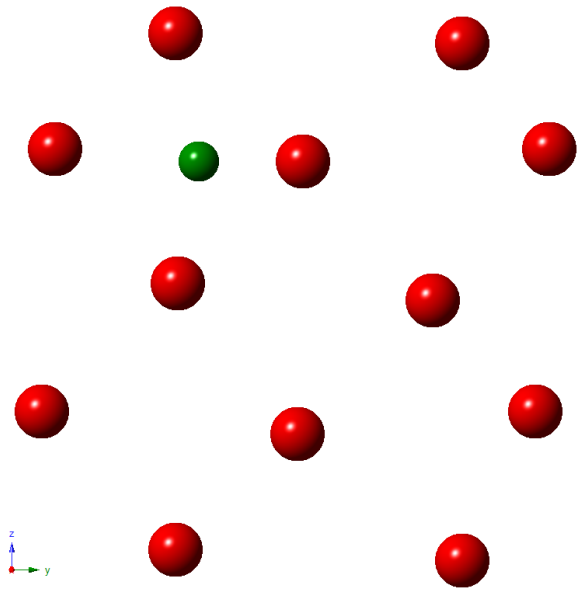
The DFT calculations performed on the midpoint of the octahedral-interstitial mechanism also yield the charge density as a function of position. The values of the charge density of a plane are

shown in Figs. 3.20 and 3.21 with colour maps where the colour is proportional to the logarithm of charge density. The charge density is localized, in an approximately spherical distribution, about the atomic positions. The colour maps show the greater charge density for the oxygen atoms compared to the lithium atoms; this agrees with the Mulliken analysis. Figs. 3.20 and 3.21 also show distortions of the spherical charge distribution when a lithium atom occupies the octahedral-interstitial site or is at the midpoint of a nn hop.

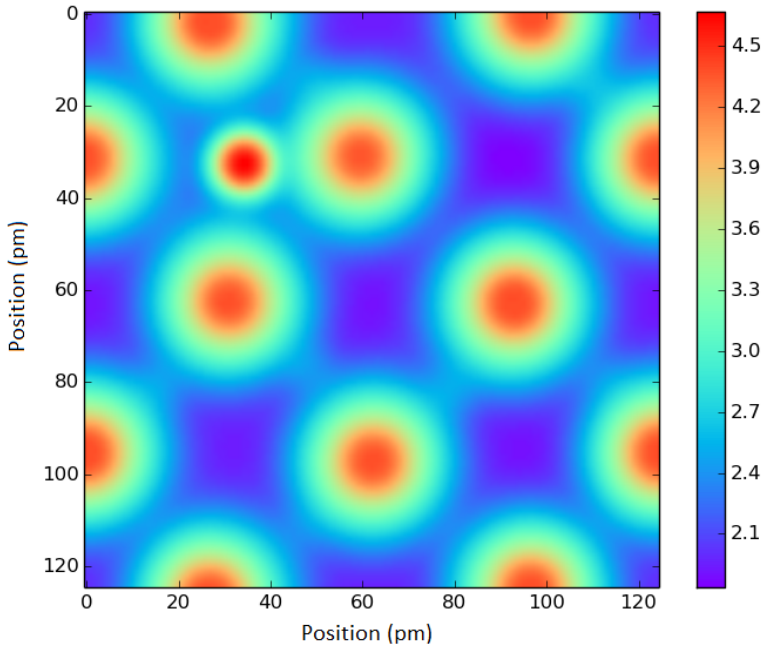


(a) (b)

Figure 3.20: The midpoint of an octahedral-interstitial mechanism viewed as a plane containing the diffusing lithium atoms normal to the (100) direction . (a) The positions of the oxygen atoms (red) and the lithium atoms (green) in a plane. (b) A colour map showing the logarithm of the charge density for plane.



(a)



(b)

Figure 3.21: The midpoint of an octahedral-interstitial mechanism viewed as a plane containing the diffusing lithium in the octahedral-interstitial site normal to the (100) direction . (a) The positions of the oxygen atoms (red) and the lithium atoms (green) in a plane. (b) A colour map showing the logarithm of the charge density for plane.

3.6 Conclusion

In this chapter the diffusion of lithium-ions in Li_2O has been modelled over a wide temperature range. Specifically, excellent agreement has been achieved between the calculated lithium diffusion coefficient values and the experimental data. This agreement was observed over the entire temperature range, $873 < T/\mathrm{K} < 1603$, and is a significant improvement compared to previous computational studies (Hayoun et al., 2005; Hayoun and Meyer, 2008; Fracchia et al., 1998; Pfeiffer et al., 2000; Goel et al., 2004; Gupta et al., 2012), which were limited to the high-temperature regime. The ability to model diffusion coefficients for lower temperatures, and consequently slow rates of diffusivity, comes from using non-equilibrium molecular dynamics. The atomic trajectories produced by the NEMD simulations allowed the mechanistic detail of individual diffusion events to be elucidated. Two mechanisms were revealed: the nearest-neighbour mechanism and the octahedral-interstitial mechanism. Although both mechanisms were observed at all temperatures, their relative importance changes. At low temperatures the nearest-neighbour mechanism dominates the diffusion, whereas at high temperatures the octahedral-interstitial mechanism is dominant. In the octahedral-interstitial mechanism, once the octahedral-interstitial site is occupied a number of nearest-neighbour hops occur. The number of these hops increases as the temperature increases. When the octahedral-interstitial site is occupied there is an induced response from the oxide sublattice, which has not been recognized in previous studies. The increase in the prevalence of the octahedral-interstitial mechanism at higher temperatures accounts for the increase in the temperature dependence of the diffusion coefficient whereas at lower temperatures, the lower temperature dependence of the diffusion coefficient is due to the dominance of the nearest-neighbour mechanism. Energy profiles of the diffusion mechanisms identified in NEMD were optimised using the force-field. These were in agreement with previous energy profiles calculated using DFT (Gupta et al., 2012) and with the mechanisms observed in the NEMD simulations. The NEMD method allows for the modelling of diffusion at lower temperatures using the colour field to increase the frequency of the diffusion events in a predictable manner but, significantly, without altering the nature of the diffusion events themselves. This allowed for the modelling of multiple diffusion mechanisms over a wider temperature range than has been previously achieved. Non-equilibrium MD extends the range of diffusivity that can be modeled with equilibrium MD to significantly slower rates, whilst maintaining diffusion as an emergent property.

The work described in this chapter is the basis for the published article:

A. D. Mulliner, P. C. Aeberhard, P. D. Battle, W. I. F. David and K. Refson

Diffusion in Li_2O studied by non-equilibrium molecular dynamics for $873 < T/\mathrm{K} < 1603$

Physical Chemistry Chemical Physics, 2015, **17**, 21470.

CHAPTER 4

Li_3N

In this chapter the diffusion of Li^+ in lithium nitride is modelled using the NEMD method over a wide temperature range. Lithium nitride is a simple, binary solid compound that exhibits superionic lithium conductivity. The high Li^+ ionic conductivity has led to much interest in Li_3N for technological applications. In the field of hydrogen storage (Makepeace et al., 2014; Ning et al., 2014), Li_3N is part of the Li-N-H system, which shows facile reversibility and acceptable volumetric and gravimetric hydrogen densities. Li_3N has long been of interest as a solid-electrolyte in solid-state batteries (Rabenau, 1982), and is still of interest as there is as yet no suitable solid-state electrolyte with which to replace the currently-used liquid electrolytes.

4.1 Crystal Structure

Two solid-state structures of Li_3N have been identified. α-Li_3N adopts a hexagonal structure consisting of alternating layers of lithium cations, usually referred to as Li(1), and layers of composition Li_2N (Fig. 4.1). The layers are stacked in an ABABAB... manner and are therefore eclipsed. In the Li_2N layer the lithium atoms are coordinated by three nitrogen atoms and the nitrogen atoms are coordinated by six lithium atoms in the layer, forming a hexagon. The Li(1) atoms lie at the midpoint of the interlayer vector between the nitrogen atoms, bringing the total coordination number of nitrogen to eight. The alpha phase belongs to the $P6/mmm$ space group with the lattice parameters $a = b = 3.648$ Å, $c = 3.875$ Å at 150 K. It is stable at room temperature and ambient pressure. The alpha phase was first identified by Zintl and Brauer (1935) and the structure was later refined by Schulz and Schwarz (1978). The alpha phase undergoes a phase transition at 300 K and 4.2 GPa to the beta phase (Beister et al., 1988). The beta phase also adopts a hexagonal structure with the space group $P6_3/mmc$ where the lattice parameters a and b show a slight contraction and the c parameter nearly doubles compared to that of the alpha phase. However, there is a significant

volume reduction of 21.6 % (Cui et al., 2009). A cubic gamma phase has been predicted at very high pressures (Lazicki et al., 2005; Ho et al., 1999).

4.2 Bonding in Li_3N

The unique structure of Li_3N is a result of the nature of the bonding interactions present in Li_3N. The presence of the N^{3-} ion is significant given the large negative charge. The bonding in Li_3N is considered to be highly ionic in character (Fister et al., 2008; Gregory, 2001). The structure, consequently assumed to contain N^{3-} and Li^+ ions, has been studied by variable-temperature, single-crystal X-ray diffraction (Schulz and Schwarz, 1978) and also by Raman and infrared spectroscopies (Chandrasekhar et al., 1978). Further neutron and Compton scattering studies also produced an ionic picture of the bonding in Li_3N (Kress et al., 1980; Pattison and Schneider, 1980; Pattison et al., 1984). Cui et al. (2009) studied the α, β and γ phases of Li_3N using first-principles calculations and concluded all three phases are strongly ionic. Gordienko (2009) similarly studied γ-Li_3N and also favoured a highly ionic bonding picture.

More recently Fister et al. (2008) carried out an extensive study of the local electronic structure of α-Li_3N using both experimental and theoretical methods. DFT methods were used to measure the electron density and the occupied electronic states. The calculated electron density showed an ionic picture of bonding with only weak deviations from sphericity in the valence charge distribution about the nitrogen atoms. Good agreement was obtained between experimental and calculated l-DOS. Non-resonant inelastic X-ray scattering was used to investigate the unoccupied electronic states of all species present.

Neighbouring, mutually-repelling negatively-charged N^{3-} ions must be effectively screened from each other by surrounding Li^+ ions. In α-Li_3N the N^{3-} ions are separated by 3.648 Å within the *ab* plane and 3.875 Å along the *c* direction. For N-N interactions along the [001] direction the nitrogens are either side of a Li^+ ion on a Li(1) site, which effectively screens the N-N interaction. However, for nearest-neighbour nitrogens within the *ab* plane there is no Li^+ ion directly between them, instead they are screened by two Li^+ ions occupying Li(2) sites forming an edge of a hexagon formed of Li atoms with a separation of 2.1 Å .

The bond populations were calculated from a plane-wave calculation performed on the ideal crystal α-Li_3N structure using CASTEP. The calculations used a Mulliken population analysis (Segall et al., 1996a,b) as implemented in CASTEP. The population of the Li-N bond has a value of 0.26,

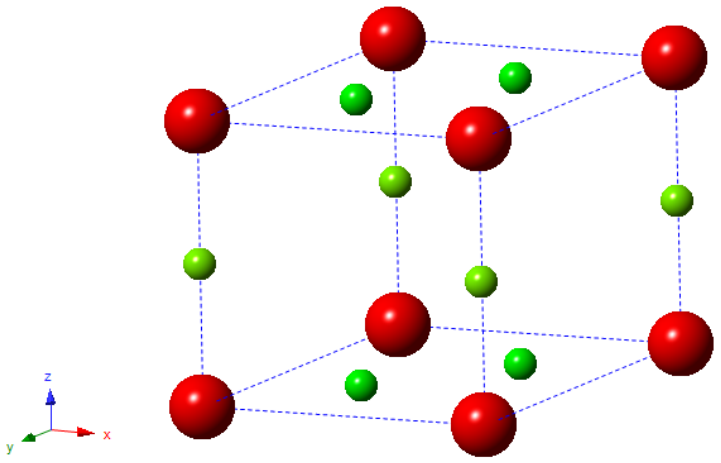


Figure 4.1: The hexagonal unit cell of Li_3N; green sphere represent lithium atoms and the red spheres represent nitrogen atoms.

which is similar to those of NaCl and NaF (Segall et al., 1996b) and well below the values found in typically covalent compounds. This supports the ionic nature of the bonding present in Li_3N.

4.3 Superionic Behaviour

Lithium nitride was first identified as a solid-state fast-ion conductor by Boukamp and Huggins (1976) in measurements made on a polycrystalline sample. Further studies by Alpen et al. (1977) measured the ionic conductivity of a single-crystal sample and found a significant temperature-dependent anisotropy of the ionic conductivity; at 300 K the measured ionic conductivity parallel to the c axis was two orders of magnitude lower than perpendicular to the c axis. It was also shown that the conductivity is purely ionic. It was recognized many years ago that, in the absence of structural disorder, it is difficult to explain the high ionic conductivity of this compound. Following the analysis of single-crystal X-ray diffraction data, Schulz and Schwarz (1978) reported that the occupancy of the lithium site in the Li_2N layers, usually labelled Li(2), was temperature-dependent and that 1.8(4) % of these sites were vacant at 293 K. No occupied interstitial sites were located and the compound was therefore described as lithium deficient. Schulz and Thiemann (1979) subsequently proposed that the apparent charge imbalance was compensated by the presence of nitride ions or

oxide ions that were incorporated during crystal growth. In 1979, Wahl measured the conductivity of several single-crystal samples and concluded, on the basis of vibrational spectroscopy data, that they were all contaminated with hydrogen. He proposed the lithium vacancies were compensated by the formation of NH^{2-} anions and the conductivity increased with increasing contamination. Lapp et al. (1983) confirmed this result, also on single crystals, and described hydrogen-doped Li_3N as an enhanced intrinsic conductor. However, extrapolation of their data led them to suggest, in agreement with Bell et al. (1981), that pure Li_3N would also be a good ionic conductor. Many of the syntheses performed by Wahl and Lapp et al. deliberately introduced hydrogen into the material. However, there is no satisfactory explanation as to why it should be present in samples that were intended to be pure. Furthermore, subsequent structural studies using neutron diffraction (Gregory et al., 2002; Huq et al., 2007) failed to identify a significant concentration of vacancies on the lithium sublattice and no convincing evidence was found for the presence of charge-compensating O^{2-} or NH^{2-} anions in the polycrystalline samples used in these experiments. These structural studies have been complemented by increasingly sophisticated ^6Li and ^7Li NMR spectroscopic studies that have elucidated the dynamics of the cation diffusion (Wilkening and Heitjans, 2012). For example, Wang et al. (2012) using NMR have used polycrystalline samples to determine the activation energy for diffusion in the Li_2N layers to be 0.150 ± 0.009 eV, in reasonable agreement with the value determined using NMR spectroscopy by Nishida et al. (1983), but less compatible with values determined from transport measurements (Alpen, 1979). There have been many NMR studies on the superionic conductivity of Li_3N (Messer et al., 1981; Brinkmann et al., 1982; Bechtold-Schweickert et al., 1984; Schirmer et al., 1992; Heitjans et al., 2008; Wilkening and Heitjans, 2012). The often measured Li(1) - Li(2) inter site jump rate shows a linear temperature dependence when plotted on a Arrhenius plot (rate of site hopping against $^1/_T$). However the temperature range of such experiments is often limited. The NMR studies indicate the rapid Li(2)-Li(2) site interchange, but relatively much slower Li(1)-Li(2) site interchange.

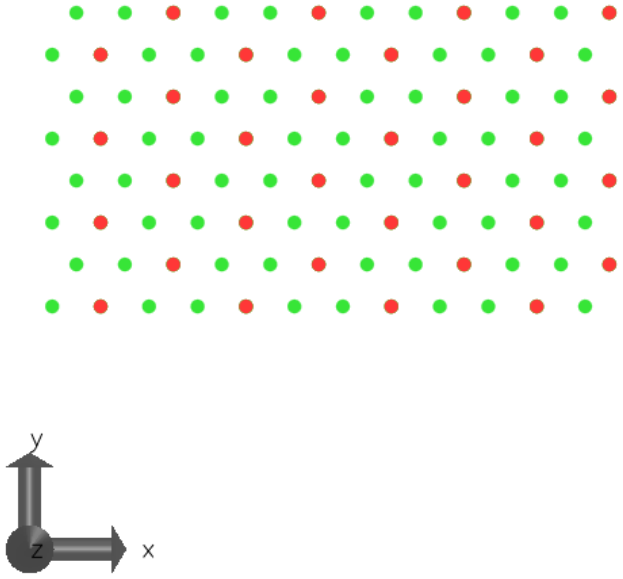
Along with the experimental studies of Li_3N, a number of computational studies have been conducted in attempts to elucidate the diffusion properties of Li_3N. The first molecular dynamic simulations performed on Li_3N were by Taylor et al. (1981); Wolf et al. (1984); Wolf and Catlow (1984). These studies were severely limited by the computational resources available at the time and the calculated diffusion coefficients were, understandably, far different from the experimental values. Despite the limitations, the analysis of single-atom trajectories began to elucidate the underlying

diffusion processes. The MD simulations by Ihara and Suzuki (1985), again constrained by the computational resources available at the time, also showed limited agreement between calculated and experimental diffusion coefficients. They also investigated the migration of individual lithium atoms and introduced the idea of ring-like motion in the Li_2N layer. Both of these early studies did manage to model the anisotropy of the diffusion. The study by Sarnthein et al. (1996) was the first study to use DFT-MD. It improved upon the agreement between calculated and experimental diffusion coefficients. A significant difference in the work by Sarnthein et al. was the modelling of a non-stoichiometric system. This was achieved by removing a single lithium cation from the supercell. The mechanistic details presented were the most comprehensive to date, with the introduction of site sharing, or horizontal Li_2 dumbbell formation, on the Li(1) site using static DFT calculations. The static calculations by Wu et al. (2009) showed that vacancies are more stable on the Li(2) than Li(1) sites. Using *ab initio* MD, Blomqvist et al. (2010) showed that creating vacancies in Li_3N increased the measured diffusion coefficient compared to fully stoichiometric Li_3N.

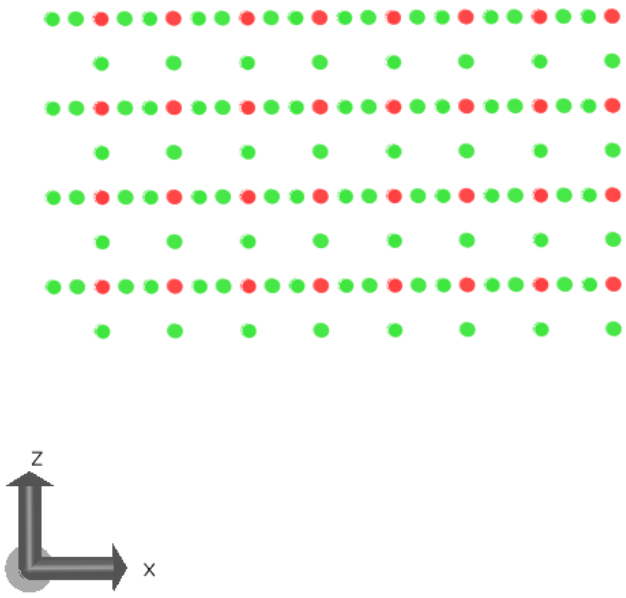
The historical account presented above demonstrates that there are discrepancies between different sets of experimental data collected on lithium nitride, and that the composition of the material and the detailed mechanism behind the ionic conductivity are still uncertain. No computational study has reproduced the measured transport coefficients to an acceptable level of accuracy. We therefore considered it timely to undertake a new study of stoichiometric lithium nitride using modern computational methods, namely NEMD, in an attempt to resolve some of these issues. In view of the proven success of NEMD in modelling Li_2O, it is appropriate to apply it to Li_3N.

4.4 Computational Details

For ease of computation, the hexagonal unit cell of Li_3N was transformed to an orthorhombic cell with$a_{ort} = a_{hex}$, $b_{ort} = \sqrt{3}/2\,(2b_{hex} + a_{hex})$ and $c_{ort} = c_{hex}$. These orthogonal axes are used in the Figures and Movies referred to in the following discussion. For reference purposes, [001] and [010] projections of the structure are shown in Figs. 4.2a and 4.2b. The supercell used for all the NEMD simulations presented was a 4x4x4 array of these orthorhombic cells containing a total of 128 formula units (512 atoms) with dimensions 25.3846 x 14.6558 x 15.5172 Å. As described in Section 3.3 for the case of Li_2O, the optimum size of the supercell was determined by performing a series of simulations with supercells having different sizes and then calculating the diffusion coefficients to check for convergence. In the case of Li_3N these test calculations showed that for supercells



(a)



(b)

Figure 4.2: Projections along (a) [001] and (b) [010] of the α-Li_3N structure in an orthogonal Cartesian unit cell having $a_{ort} = a_{hex}$, $b_{ort} = \sqrt{3}/2\,(2b_{hex} + a_{hex})$ and $c_{ort} = c_{hex}$. Green and red circles represent lithium and nitrogen atoms, respectively.

larger than or equal to 4x4x4 the errors due to finite-size effects were not greater than 11 %. The NEMD simulations were performed using a version of the CP2K package that had been modified (Aeberhard et al., 2012) to include the colour-diffusion algorithm of Evans et al. (1983). Use of the colour-diffusion algorithm necessitates the use of a Gaussian-isokinetic thermostat. The integration of the equations of motion was performed with a 1 fs time step in order to minimize the drift in conserved quantities. Simulations were run for 100 ps after an initial 10 ps equilibration period. The forces used in the NEMD calculations were calculated from a Buckingham potential that defines the interaction energy between atoms i and j as:

$$V_{ij}(r_{ij}) = \frac{q_i q_j}{r_{ij}} + A_{ij} \exp\left(\frac{-r_{ij}}{\rho_{ij}}\right) - \frac{C_{ij}}{r_{ij}^6}. \tag{4.1}$$

The Coulombic term dominates the long-range interactions and short-range interactions are dominated by the parametrized terms; values of the latter were taken from Wolf et al. (1984):

Interaction	A (eV)	ρ (Å)	C (eV Å^6)
Li^+/ Li^+	916.59366	0.14270	0.0
N^{3-}/ Li^+	232.59366	0.43284	0.0
N^{3-}/ N^{3-}	22259.27515	0.282	2102.66667

Table 4.1: Pairwise potential parameters for Li_3N using the Buckingham potential.

The values of the parameters for the Buckingham model of the bonding in Li_3N are shown in the table above. The Buckingham model was also used for modelling Li_2O (Section 3.3) Despite both being simple binary ionic compounds with a common cation the values derived for the parameters vary significantly. This is not unusual for the Buckingham potential. Telfert et al. (1996) fitted parameters for a range of binary metal ionic oxides. The resulting parameters gave good agreement with experimental data for lattice parameters and elastic constants. However, the values of the parameters varied widely often by orders of magnitudes. The difference in the values for Li_2O and Li_3N is consistent with the very different environments present in the two compounds. Li_2O adopts the ubiquitous anti-fluorite structure and the parameters are rather normal, where as Li_3N adopts a unique structure that is dominated by the presence of the N^{3-} and therefore the derived parameters are also rather unique. The force-field derived for Li_2O by Fracchia et al. (1998) was fitted using Hartree-Fock calculations and where as the Li_3N force-field was only fitted to lattice parameters. The nature of the Buckingham potential means the A and the ρ parameters are highly correlated.

The potentials for Li-O and Li-N are plotted in Fig. 4.3 and despite the different values of the parameters yield similar overall curves.

In order to model diffusion perpendicular to and within the *ab* plane the NEMD colour field was applied along the [001] and [100] directions, respectively. The lithium ions in alternating –(Li_2N – Li)– double layers were assigned colour charges of +1 and -1. At each chosen temperature, NEMD simulations were performed using three different colour-field strengths which were in the linear regime, e.g. at 400 K the colour field strengths of 0.025, 0.05, 0.075, and 0.1 eV $Å^{-1}$ were used. Care was taken to ensure that the responses were linear and the extrapolation to equilibrium conditions, i.e. the absence of a colour field, was therefore valid. The lithium diffusion coefficients for both directions were calculated from the individual atom trajectories using the method described previously in Section 2.12.3.

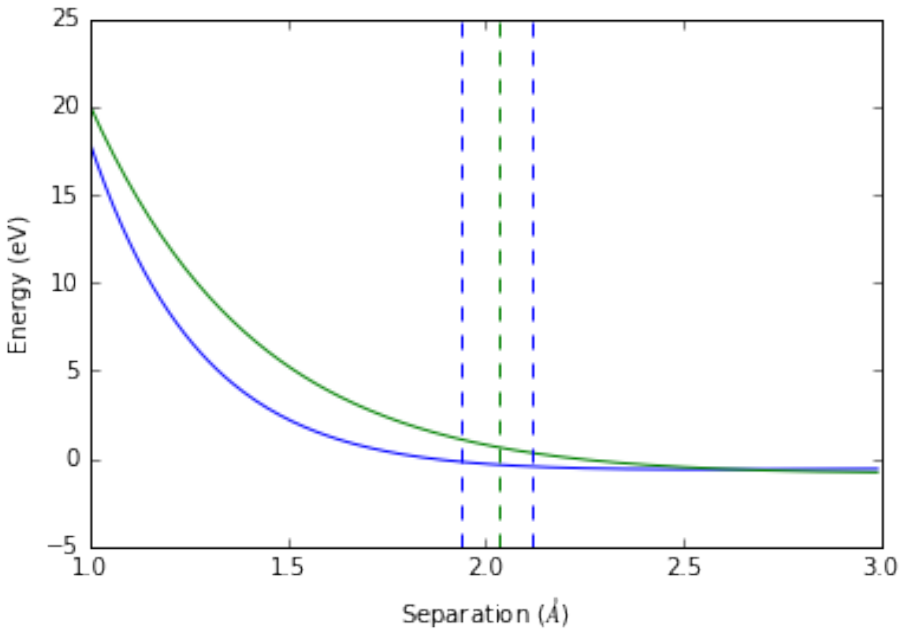


Figure 4.3: A comparison of Li-O and Li-N potentials from Fracchia et al. (1998) and Wolf et al. (1984). The green line represents Li-O and the blue line represents Li-N. The vertical dotted lines represent the nearest-neighbour distances present for Li-O (green) and the Li(1)-N and Li(2)-N (blue).

4.5 Results and Discussion

Simulations were performed over a wider temperature range than has previously been reported. The resulting lithium atom trajectories were used to calculate the lithium diffusion coefficient, and associated errors, using the method outlined in Section 2.12.3 and previously used in Section 3.5.1.

4.5.1 Temperature Dependence of the Lithium Diffusion Coefficient

The temperature dependence of the lithium diffusion coefficients determined by the NEMD simulations, and experimental results from Wang et al. (2012), are shown in Fig. 4.4 for the diffusivity both parallel and perpendicular to the [001] direction. For both directions, the measured diffusion coefficient decreases as temperature decreases, as would be expected. For all temperatures simulated the diffusion in the xy plane was faster than the diffusion perpendicular to the plane. The difference between the two rates decreases as the temperature increases. The lithium diffusion coefficients for the xy plane determined experimentally by Wang et al. (2012) are also shown in Fig. 4.4, and can be seen more clearly in the inset. Unfortunately the temperature range of the experimental data is small compared to the temperature range of the NEMD simulations and the comparison is therefore limited. However, there is good agreement between the experimental and computational results for the available temperature range. The rate of diffusion is related to the number of diffusion events which also defines the error in the calculated diffusion coefficient therefore the error increases as the temperature decreases. Given the much slower diffusion perpendicular to the (001) plane compared to that in the plane, the lowest temperature accessible with FF-NEMD is much higher along [001]. In order to allow rapid diffusion to occur in fully stoichiometric Li_3N, a regular lattice site must become vacant for long enough to initiate a diffusion process. Upon inspection of the atom trajectories, it can be seen that vacancies are formed via two distinct mechanisms.

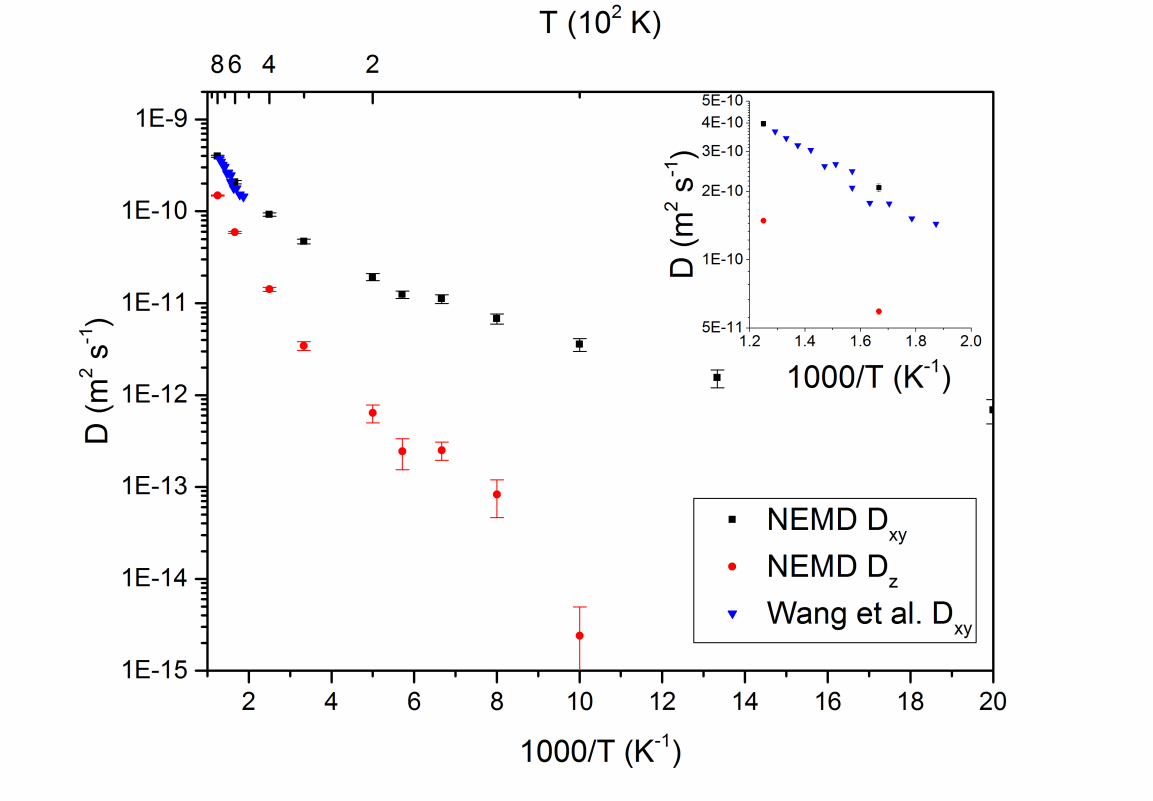
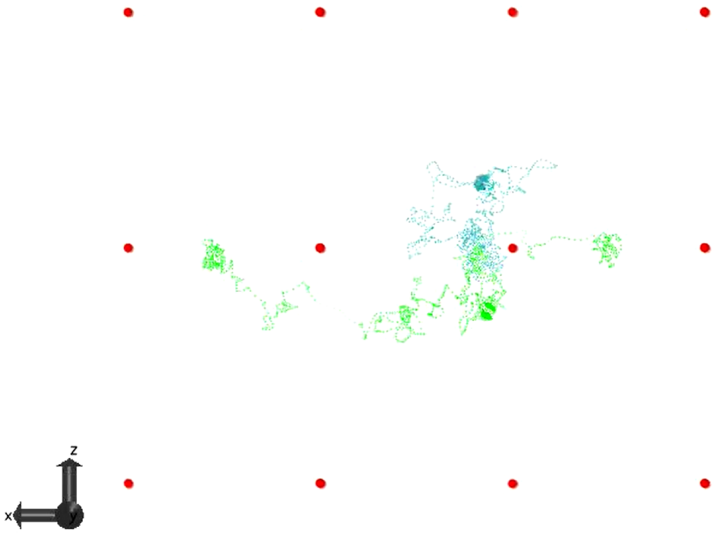


Figure 4.4: The temperature dependence of the lithium diffusion coefficient in Li_3N. Black squares represent values from FF-NEMD simulations for diffusion in the xy plane; red circles represent values from FF-NEMD simulations for diffusion perpendicular to the xy plane; blue triangles represent values from Wang et al. (2012).

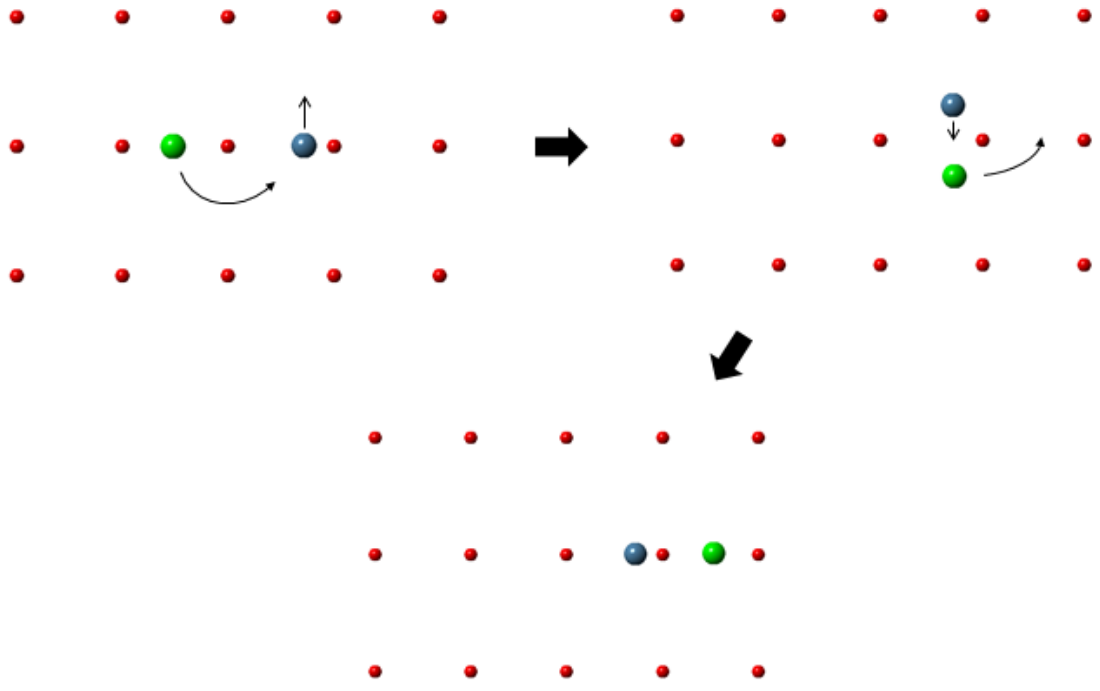
4.5.2 Vertical Dumbbell Around the Li(2) Site

The first of the two vacancy-creating mechanisms involves the formation of a vertical dumbbell about a Li(2) site consisting of two lithium ions. A lithium atom from a Li(2) site leaves the Li_2N plane and moves towards an adjacent Li(2) site, diffusing approximately 2.1 Å through the structure at a distance $\pm c/4$ above or below the Li_2N layer. As the diffusing Li(2) moves towards an occupied Li(2) site, the resident lithium atom is displaced to a position approximately $\mp c/4$ from the site. These two lithium atoms form a dumbbell sharing the Li(2) site aligned along [001]. The separation between the two lithium atoms, forming the dumbbell, is approximately 2.1 Å. The dumbbell exists for approximately 2 ps. The termination of the vertical dumbbell involves either of the lithium atoms moving onto the Li(2) site; the other lithium atom concomitantly moves on in the interlayer space to repeat the process until it also moves to a vacant site in the layer. Whilst the dumbbell exists the vacancy on a Li(2) site can rapidly diffuse through the Li_2N layer. The mechanism is shown in Movie 4.1†; stills from the movie are shown in Fig. 4.5a. The movie shows the migration of a lithium cation to the interlayer space, brief sojourns close to two adjacent Li(2) cations (not shown), a detailed depiction of the dumbbell formation and motion around the third Li(2) site that is encountered and, finally, the termination of the process when the featured cation is able to return to the Li_2N layer. The time dependence of the distance between the two lithium atoms forming the dumbbell is shown in Fig. 4.6. The dumbbell exists for approximately 2.5 ps in the centre of the time window. The Li-Li separation is approximately 2.1 Å whilst the dumbbell exists and after it is terminated the separation is similarly 2.1 Å, as the two lithium atoms are nearest-neighbours on the Li_2N layer. The Li-Li separation of the dumbbell is very similar to the nearest-neighbour separations found in the regular structure. The deviation of the vertical dumbbell from ideal geometry is shown in Fig. 4.7a. The angle formed by the two lithium atoms and the ideal Li(2) site is shown as a function of time; if these three positions were colinear, the angle would be 180°. During the lifetime of the dumbbell, the angle is near 180°. It does not exceed 180° as the angle is measured by the dot product of the two vectors formed from the ideal Li(2) site to the two lithium atoms forming the dumbbell. Before and after the existence of the dumbbell the value of the angle provides no great insight. The orientation of the dumbbell is shown in Fig. 4.7b. The tilt angle, δ_v, is the angle between the [001] direction and the vector formed by the positions of the two lithium atoms forming

† Attached in the back cover is a CD that contains movies of diffusion referred to in this thesis. The captions for these movies can be found in Appendix I.



(a)



(b)

Figure 4.5: The vertical dumbbell mechanism on a Li(2) site, which is also shown in Movie 4.1†, viewed along [010]. (a) The green and blue spheres are Li^+ cations. The red spheres represent the N^{3-} anions. The traces show the diffusion of Li^+ cations. Each point in the trace represents a time window of 1 fs. (b) Graphical depiction showing the motion of the atoms.

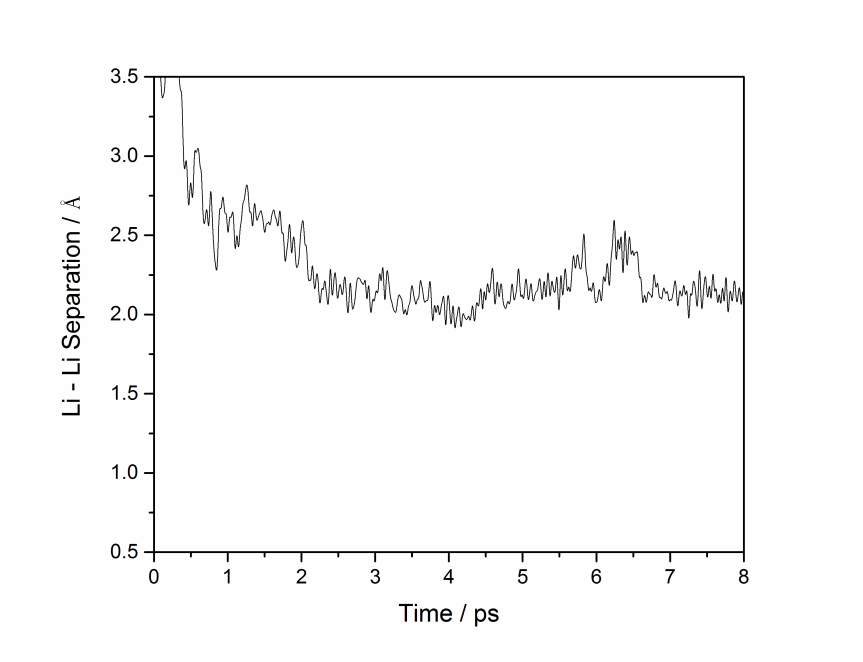
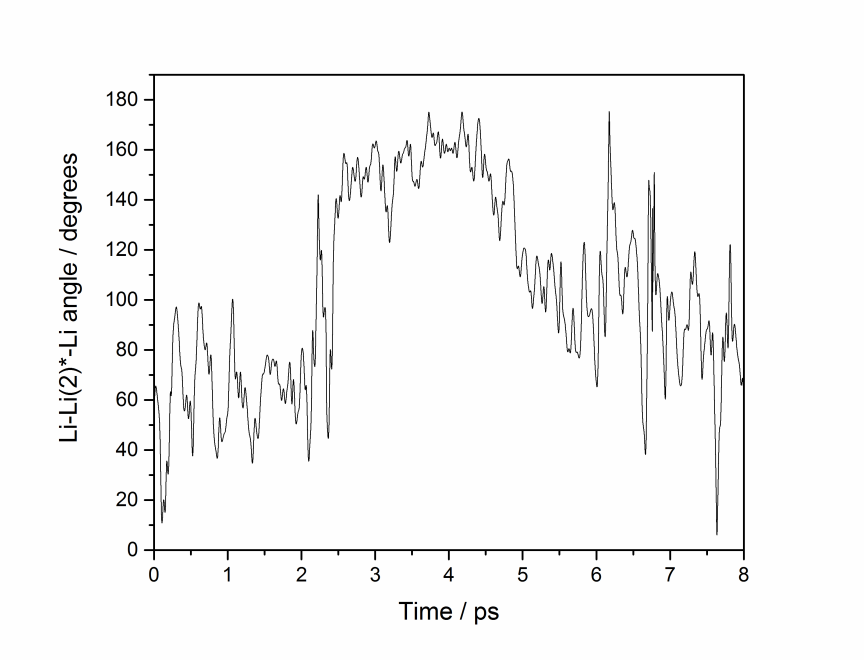
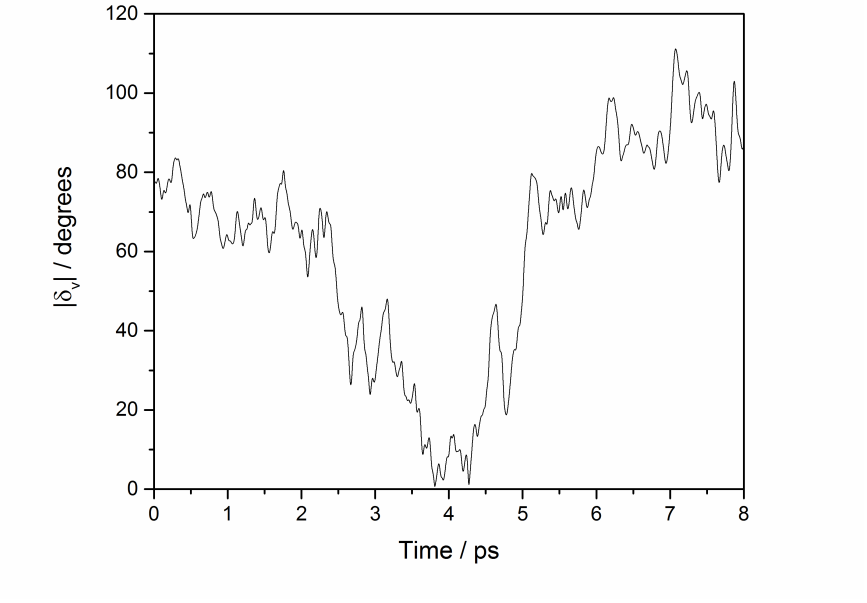


Figure 4.6: Time dependence of the Li - Li bond length in a Li_2 dumbbell formed around a Li(2) site. The dumbbell can be considered to exist for $2 < t \text{ / ps} < 5$.

the dumbbell. These figures show the two lithium ions forming the dumbbell are colinear with the Li(2) site they form about for the entirety of its existence, and can be considered to be parallel to [001] for about half of the overall lifetime.



(a)



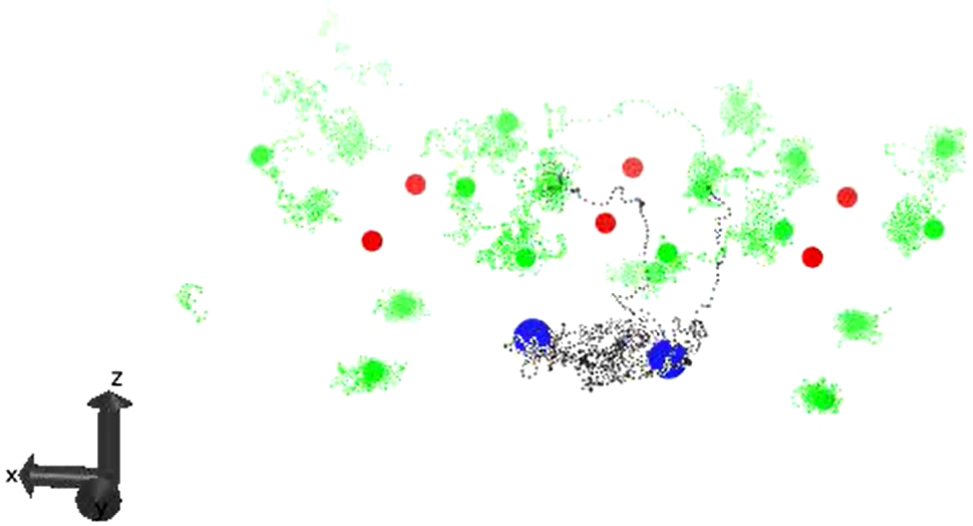
(b)

Figure 4.7: Time dependence of the angles in a Li_2 dumbbell formed around a Li(2) site; (a) the Li - Li(2)* - Li angle (where Li(2)* represents the ideal Li(2) site) and (b) the tilt angle, δ_v, between the Li - Li vector and [001]. The dumbbell can be considered to exist for $2 < t/ps < 5$.

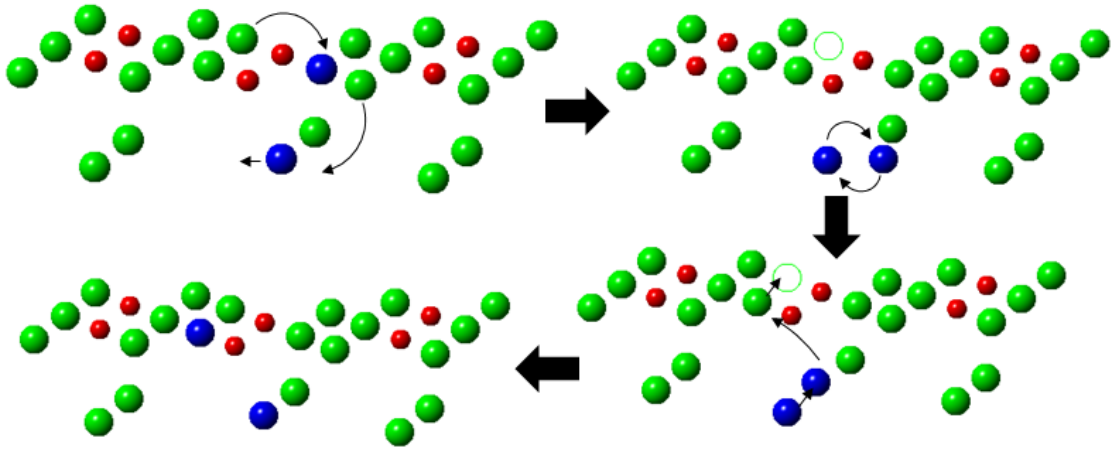
4.5.3 Horizontal Dumbbell Around the Li(1) Site

The second mechanism for creating a vacancy on a Li(2) site involves the Li(1) site. This mechanism is similar to the vertical dumbbell mechanism, but instead a dumbbell is formed about a Li(1) site. Along with promoting diffusion in the Li_2N plane, it allows for extended diffusion in the [001] direction. The dumbbell formed about the Li(1) site lies in the (001) plane. The mechanism is initiated by a lithium atom from a Li(2) site moving towards an occupied Li(1) site. Then the lithium atom lying on the Li(1) site moves off its site. The two lithium atoms form a horizontal dumbbell about the Li(1) site. The mechanism is terminated when one of the two lithium atoms moves towards a vacant Li(2) site in an adjacent Li_2N layer and the other lithium returns to the Li(1) site. Movie 4.2† and Fig. 4.8 show the horizontal dumbbell mechanism. Once the dumbbell is formed, the vacant Li(2) site can rapidly diffuse throughout the Li_2N layer. The two lithium atoms forming the dumbbell rotate about the Li(1) site. This type of dumbbell exists for typically, 4 ps. The Li(1) site lies directly between two nitrogen atoms. The interatomic separations of the two lithium and two nitrogen atoms forming the extended dumbbell motif are shown in Fig. 4.9a - the key is shown in Fig. 4.9b. The dumbbell can be considered to exist in the time period 1.5 to 5.5 ps. The Li - Li distance, represented by the green line, is approximately 2.1 Å for the duration of the dumbbell. Before and after the existence of the dumbbell the distance corresponds to the Li(1) - Li(2) nearest-neighbour distance. The four Li - N distances are also about 2.1 Å during the existence of the dumbbell. The N - N distance, represented by the red line, shows a clear decrease from its equilibrium value during the existence of the dumbbell. This contraction in the N - N separation is to stabilize the dumbbell by maintaining an appropriate Li - N distance. The colinearity of the dumbbell with the Li(1) site is shown in Fig. 4.10a by the angle between the two lithium atoms of the dumbbell and the ideal Li(1) site. The angle for the duration of the dumbbell is near 180°, but as before does not go beyond 180°. The angle before and after the dumbbell is meaningless, as one of the lithium atoms lies on the ideal Li(1) site. The dumbbell lies in the (001) plane. The deviation of the vector formed by the two lithium atoms from the (001) plane is shown in Fig. 4.10b. The dumbbell lies in the plane, or at least very close, throughout its existence.

From Movie 4.2†, and more clearly in Movie 4.3† (the top-down view) the dumbbell is oriented in three specific directions in the (001) plane and rotates between them. This will be discussed further in Section 4.5.6.

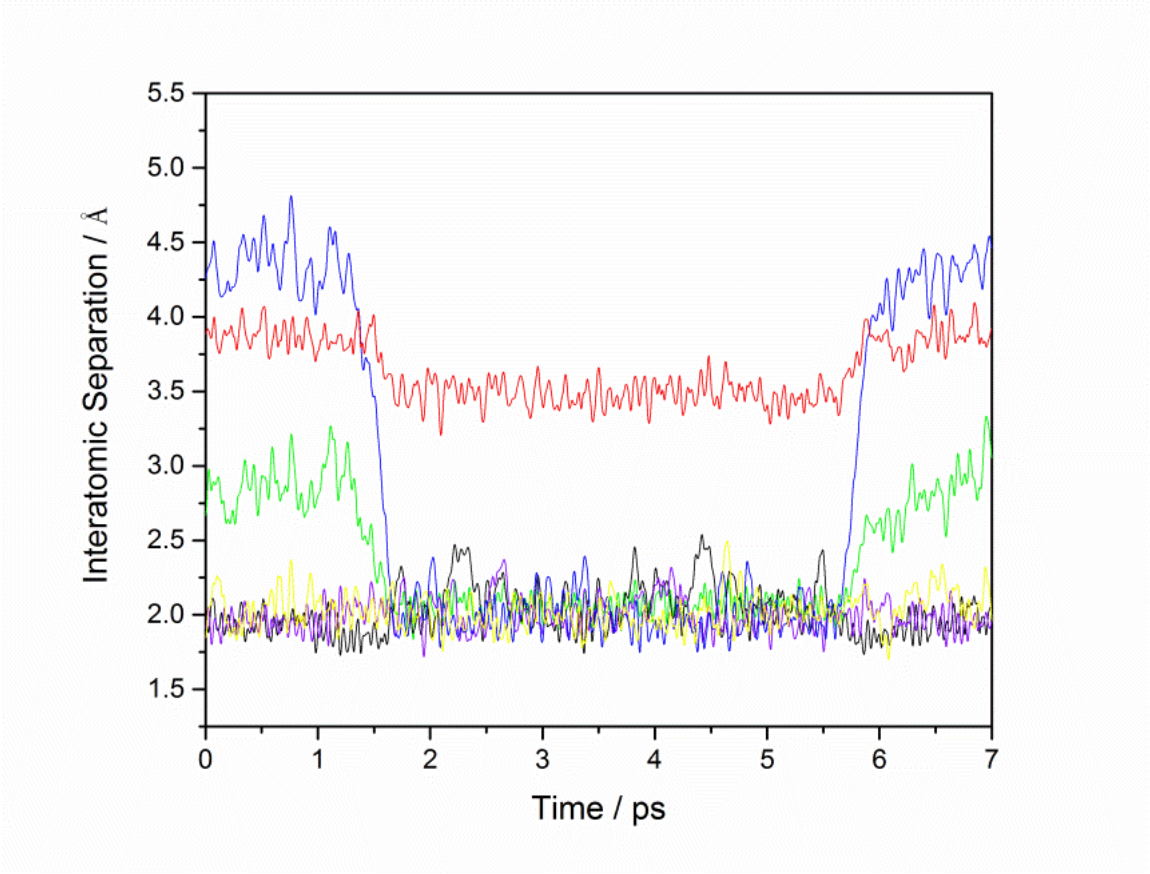


(a)

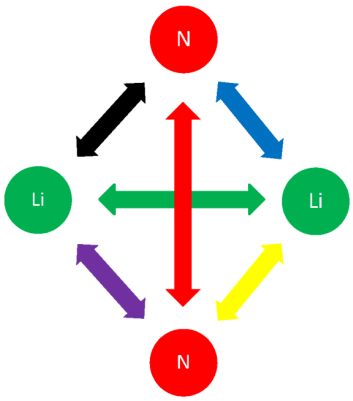


(b)

Figure 4.8: The horizontal dumbbell mechanism around a Li(1) site, which is also shown in Movie 4.2†. (a) The green and blue spheres are Li^+ cations. The blue spheres are for the two Li^+ cations that form the dumbbell and the green spheres show nearby Li^+ cations. The red spheres represent the N^{3-} anions. The traces show the diffusion of Li^+ cations. Each point in the trace represents a time window of 1 fs. (b) Graphical depiction showing the motion of atoms.

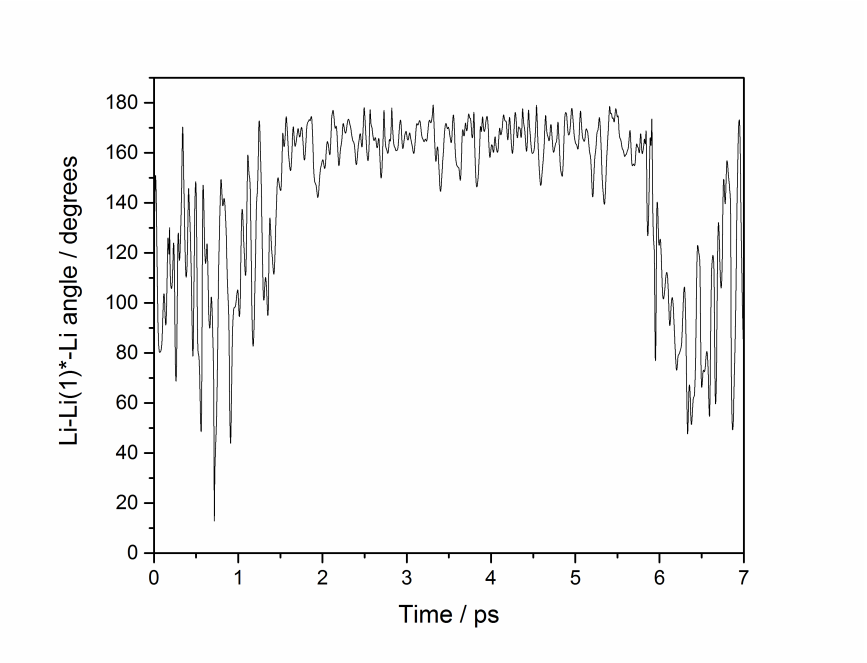


(a)

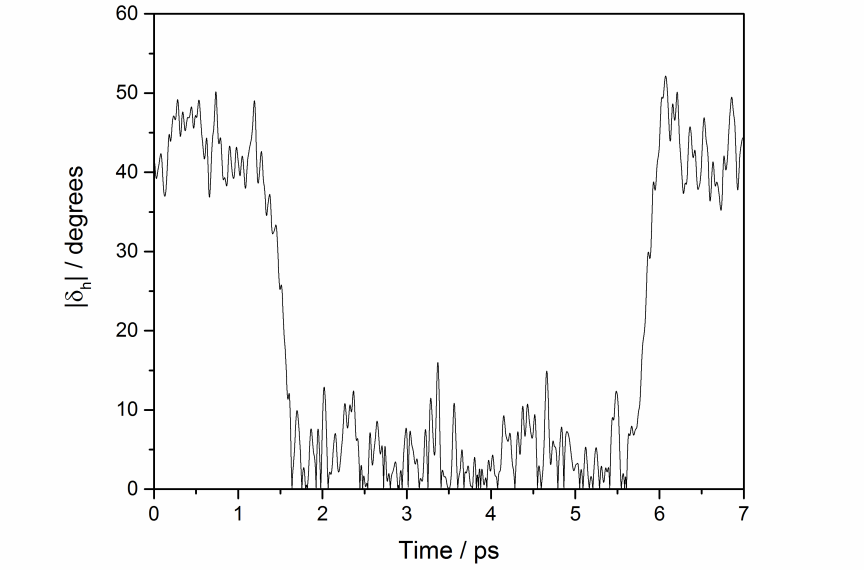


(b)

Figure 4.9: (a) Time dependence of the bond lengths in a Li_2 dumbbell formed around a Li(1) site. (b) A colour key to identify the interatomic distances.



(a)



(b)

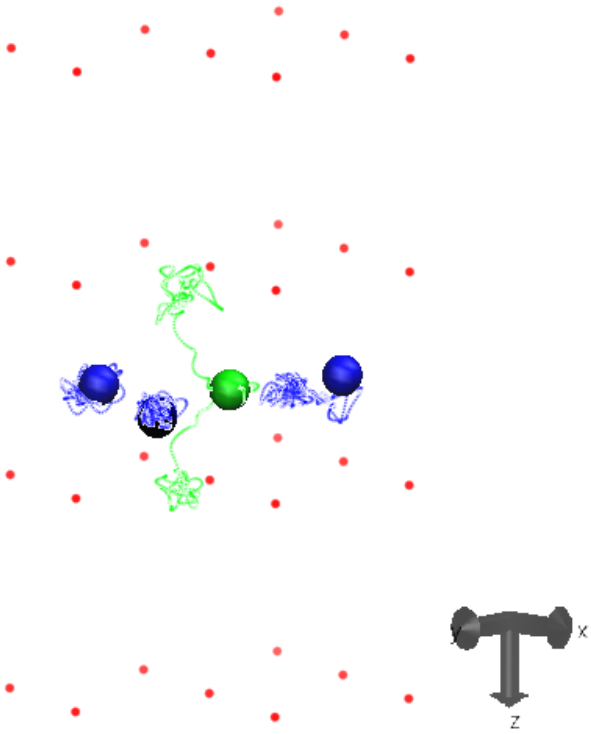
Figure 4.10: Time dependence of bond angles in a Li_2 dumbbell formed around a Li(1) site; (a) the Li - Li(1)* - Li angle (where Li(1)* represents the ideal Li(1) site) and (b) the angle, δ_h, between the Li - Li vector and the Li_2N plane. The dumbbell can be considered to exist for $2.5 < t\,/\,ps < 6.5$.

It is interesting to note that during the lifetime of the dumbbell the repulsion between a pair of nitride ions in neighbouring Li_2N layers is screened by two lithium cations midway between the two layers with a Li-Li separation of 2.1 Å apart. This is very similar to screening provided within the normal Li_2N layers, where pairs of nitride ions are screened by two lithium cations located on regular Li(2) sites separated by 2.1 Å, see Figs. 4.2a and 4.2b. Dumbbell formation is therefore capable of providing the necessary interlayer screening; in the absence of the dumbbell this screening is provided by a single lithium cation at the midpoint of the N-N vector, a Li(1) site. Any lithium deficiency in the Li(1) layer would remove this crucial screening, but the presence of of excess lithium in the form of a dumbbell is acceptable.

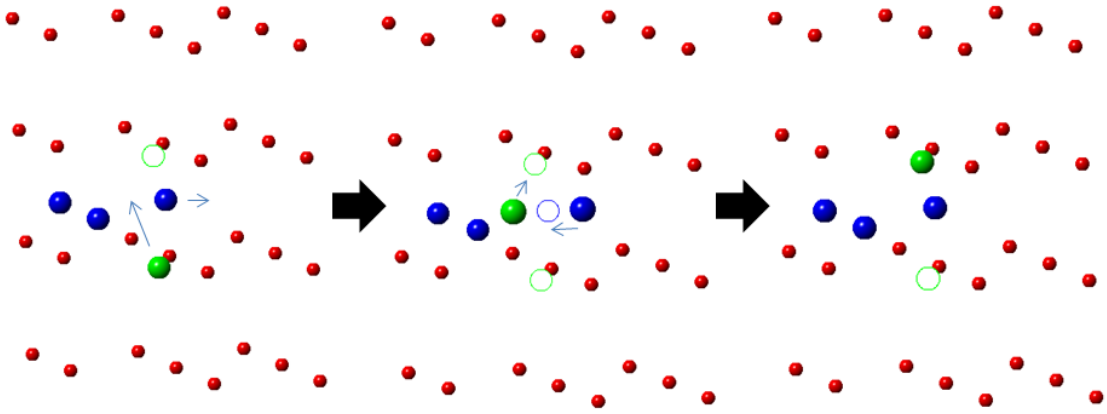
4.5.4 Mechanisms of Diffusion Along [001]

The diffusion of lithium atoms parallel to the z axis typically involves their movement between the Li_2N and Li(1) layers. It has been previously shown (Section 4.5.3) that a lithium atom can move from the Li_2N layer towards an occupied Li(1) site, whereupon the two lithium atoms form a horizontal Li_2 dumbbell centred on the site. This dumbbell is terminated when one of the two lithium atoms moves to a nearby vacant Li(2) site. This process allows the movement of lithium atoms between Li_2N layers as the termination of a dumbbell allows a lithium atom to return to its original layer or to proceed to the adjacent Li_2N layer. The horizontal dumbbell can exist for a few picoseconds, but can also be extremely short lived i.e. ~ 0.5 ps. Such a short-lived dumbbell is shown in Fig. 4.11a and Movie 4.4†. This mechanism shows a lithium atom moving from one Li_2N layer to another. The initial and final sites have the same x and y coordinates, thus the overall result is pure [001] diffusion. If the lithium were to proceed along a hypothetical vertical path, it would pass through the centre of an equilateral triangle formed by three Li(1) atoms. However, it is clear the mobile lithium atom does not proceed through the centre of the triangle, but passes closer to one of the Li(1) atoms with which it forms the dumbbell. The interatomic separations between the diffusing lithium atom and the three Li(1) atoms are shown in Fig. 4.12a. The black line represents the interatomic separation between the mobile lithium and the Li(1) that forms the temporary dumbbell. The three separations are approximately equal (≈ 2.75 Å), except for the brief reduction in distance between the two lithium atoms forming the dumbbell to a distance of approximately 2.1 Å in the time period of 1 to 1.5 ps. This is the same distance as observed in the horizontal dumbbell formed during diffusion in the (001) layers (Fig. 4.9a). The three bond lengths in the Li(1) triangle are shown in Fig. 4.12b. They are initially equivalent, as would be expected from an equilateral triangle, but when the dumbbell is formed two of the distances increase and one remains constant. The formation of the dumbbell thus requires the equilateral triangle to change into an isosceles triangle. This is the dominant mechanism of [001] diffusion.

There is a secondary, less frequent, mechanism for [001] diffusion in which a lithium atom proceeds between Li_2N layers, but does not form a dumbbell on a Li(1) site. The diffusing lithium atom moves directly between adjacent Li_2N layers proceeding through an edge of a triangle formed by the nearest-neighbour Li(1) atoms. This direct interlayer mechanism is shown in Fig. 4.13a and Movie 4.5†. Unlike in the dumbbell-mediated interlayer diffusion, the overall direct diffusion mechanism involves

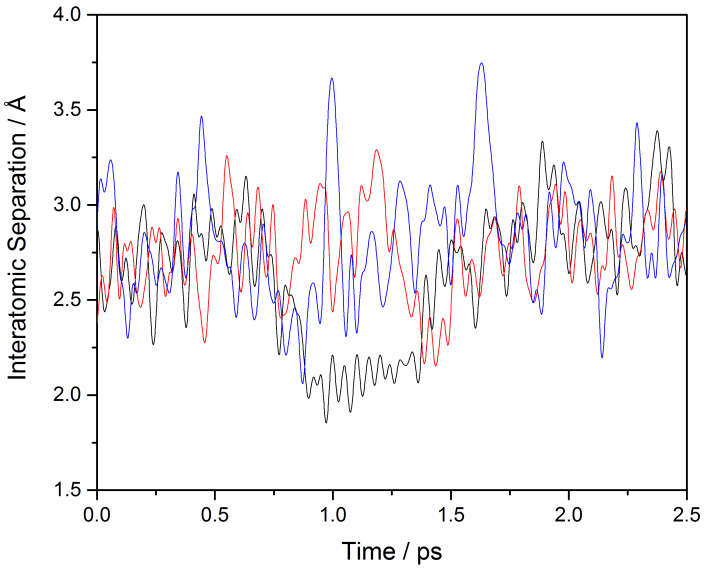


(a)

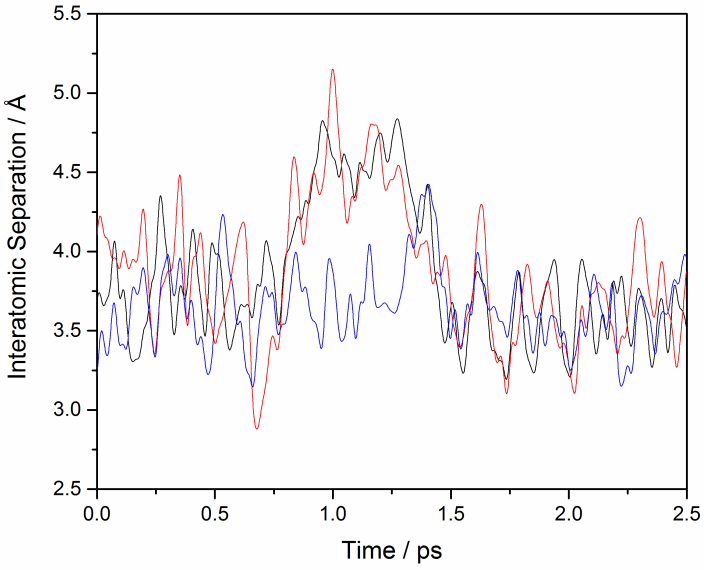


(b)

Figure 4.11: Interlayer diffusion via a Li(1) site at 600 K, corresponding to Movie 4.4†. The red and blue spheres represent Li(2) and Li(1) atoms respectively. The green sphere is the diffusing lithium atom. (a) The coloured points represent a 1 fs time window. (b) Graphical depiction of the motion of atoms.



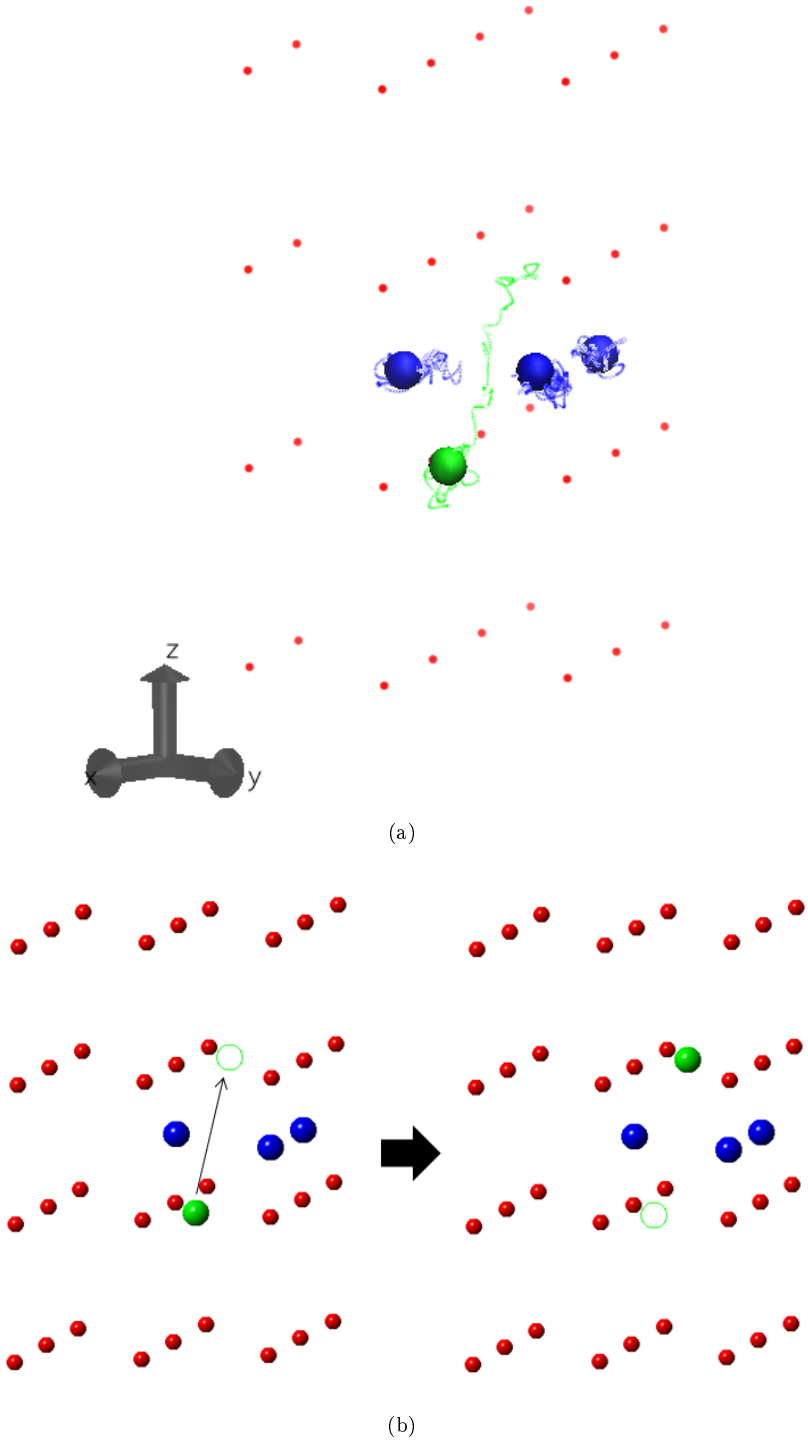
(a)



(b)

Figure 4.12: Time dependence of bond lengths for the interlayer dumbbell diffusion mechanism shown in Fig. 4.11a and Movie 4.4†. (a) The separations between the diffusing lithium atom, Li(2), and the three Li(1) lithium atoms. (b) The bond lengths between the three Li(1) lithium atoms that form a triangle of nearest-neighbours, which the Li(2) cation passes through.

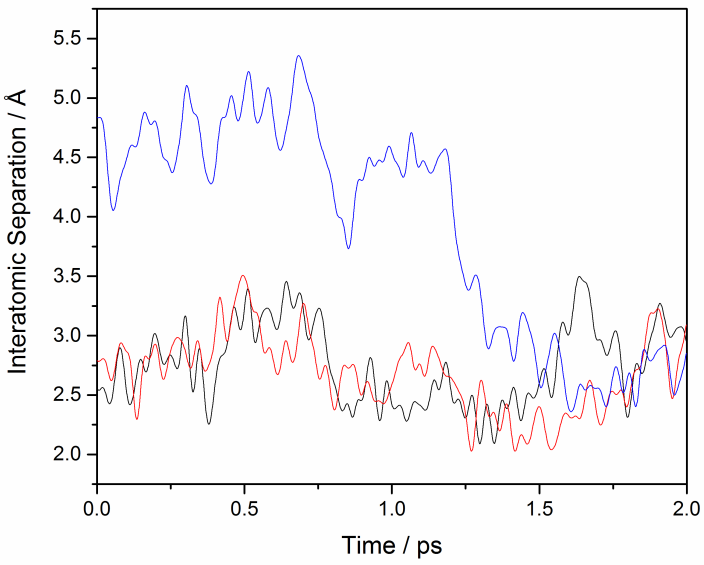
not only diffusion in the z direction, but also in the xy plane. The bond lengths between the diffusing lithium atom and the three Li(1) atoms forming the triangle are shown in Fig. 4.14a. The distances represented by the red and black lines are approximately constant whereas the distance represented by the blue line shows a significant change due to the diffusion in the xy plane. Comparing Fig. 4.14a to Fig. 4.12a, it is clear that in the former there is no temporary shortening of one of the Li - Li distances, i.e. the formation of a dumbbell, which does occur in the latter. Fig. 4.14b shows the bond lengths between the three Li(1) atoms forming a triangle. The values do not change significantly throughout the mechanism and remain approximately equal. This means the three Li(1) atoms remain on their lattice sites during this direct interlayer mechanism, whereas for the dumbbell-mediated interlayer mechanism shown in Movie 4.4†, the position of one Li(1) atom is significantly altered.



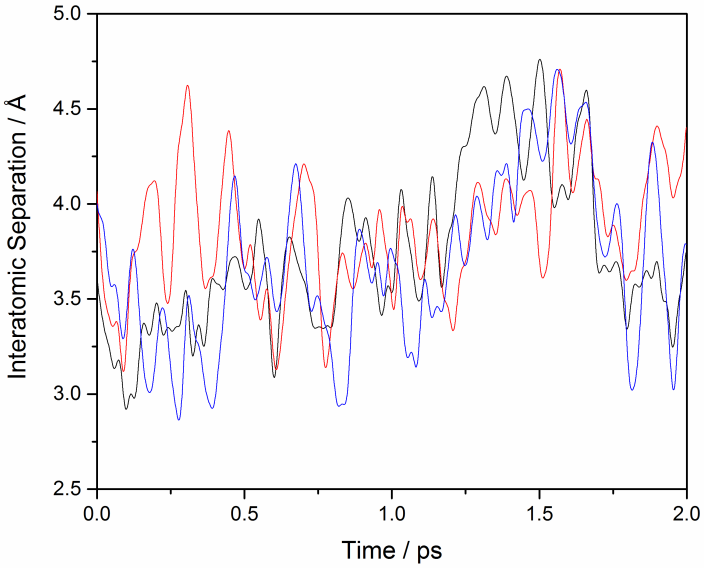
(a)

(b)

Figure 4.13: Interlayer diffusion through a Li(1) - Li(1) edge at 600 K corresponding to Movie 4.5†. The red and blue spheres represent are the Li(2) and Li(1) atoms respectively. The green sphere is the diffusing lithium atom. (a) The coloured points represent a 1 fs time window. (b) Graphical depiction of the motion of atoms.



(a)



(b)

Figure 4.14: Time dependence of bond lengths for the interlayer dumbbell diffusion mechanism shown in Fig. 4.13a and Movie 4.5†. (a) The separations between the diffusing lithium atom, Li(2), and the three Li(1) lithium atoms. (b) The bond lengths between the three Li(1) lithium atoms that form a triangle of nearest-neighbours, which the diffusing Li(2) cation passes through.

4.5.5 Energy Profiles of Diffusion

The horizontal dumbbell was observed to have a Li-Li bond length of ~ 2.01 Å, which is similar to the Li(2)-Li(2) separation in the ideal crystal structure (2.11 Å). In order show the stability of the dumbbell in both DFT and FF an energy profile was generated using both FF and DFT for different fixed lengths of a horizontal dumbbell in a 4x4x4 Li_3N supercell. In order to maintain overall charge neutrality a lithium was removed from a regular Li(2) site and then place into the dumbbell. The horizontal lithium dumbbell was aligned 30° from the hexagons of the Li_2N layers and the separation varied and then the energy minimized. The energy profile for varying dumbbell length is shown in Fig. 4.15 for both DFT and FF. The separation was varied from 0.5 to 6 Å for the force-field and a smaller range for DFT. Both were fitted with a polynomial curve. Both curves yield a minimum value at ~ 2.01 Å .

The stability of both the horizontal and vertical dumbbells was tested by taking MD snapshots where either a horizontal or vertical dumbbell is present and using these coordinates as the input for geometry optimisations. The dumbbells remained in the final structure as they represent local minima.

In order to show that the forces calculated by FF and DFT for Li_3N are somewhat similar. The atomic forces were calculated for the same time step, i.e. the same coordinates, using both the force-field and DFT methods. Fig. 4.16 is a scatter plot of a series of timesteps where a dumbbell is present. The correlation is rather good between the DFT and FF forces and for the forces involved in the dumbbell the correlation is maintained. This suggests that the formation of dumbbells is not an artifact due to a poorly fitted force-field.

The FF-NEMD data shows the the horizontal dumbbells orient themselves onto the opposite vertices of a hexagon that is offset by 30° from the hexagons of the Li_2N layers in order to minimize repulsive interactions. An energy profile has been generated to show the rotational dynamics of the horizontal dumbbell. A 4x4x4 Li_3N supercell was setup with a horizontal dumbbell about a Li(1) site and a vacancy on a Li(2) site in order to maintain charge neutrality. This was used as the input and final coordinates for a NEB calculation and the intermediate coordinates were set as sequential 60° rotation about the Li(1) site of the horizontal dumbbell. The resulting energy profiles is shown in Fig. 4.17. The bond length of the dumbbell was not constrained but the resulting configurations maintained the ~ 2.0 Å Li-Li separation. The energy profile showed energy barriers between the

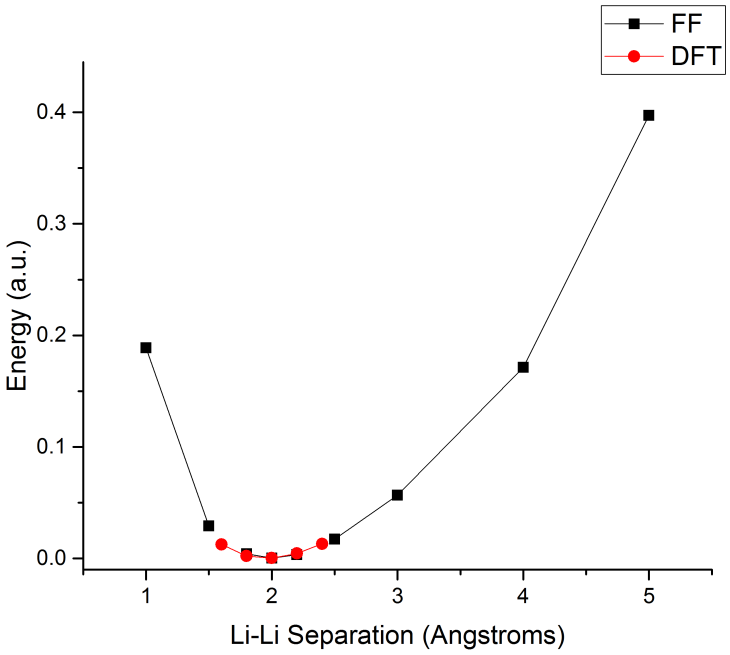
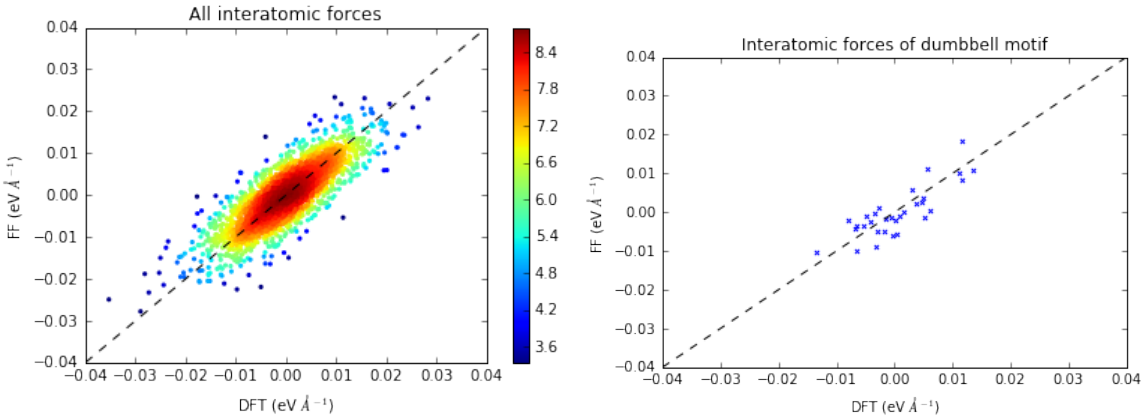


Figure 4.15: The relative energy of Li_3N containing a horizontal dumbbell for varying dumbbell separations calculated using both FF and DFT methods, black squares and red circles, respectively.



(a) (b)

Figure 4.16: The Cartesian forces acting on each atom in a series of configurations calculated by both FF and DFT. (a) Shows all atoms present in the supercell and the colour of points represents the log of the number density. (b) Only shows atoms present in the dumbbell motifs. The dashed lines represents ideal correlation.

local minima. The local minima correspond to configurations where the Li-Li dumbbell is aligned 30° off from the Li_2N hexagonal layer in order to minimize the interactions. This is in agreement with the NEMD data that showed increased density about the hexagonal sites corresponding to these local minima. However, the energy barriers between local minima are very small and explains why the Li-Li dumbbell rotates easily. The energy barriers and local minima are not equivalent possibly due to the anisotropic environment present due to the distortion due to the presence of a single Li(2) vacancy.

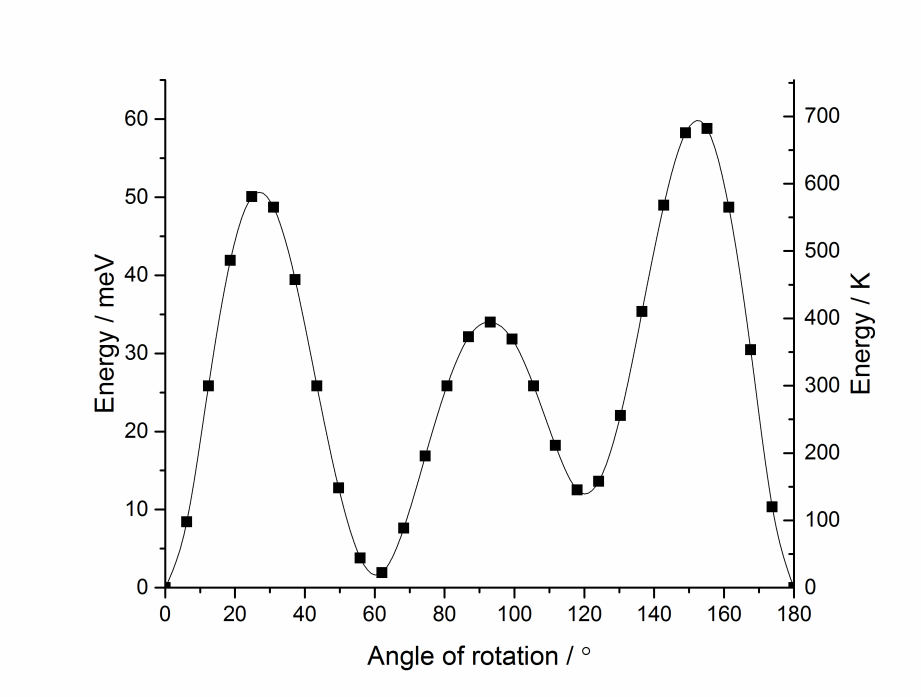


Figure 4.17: The energy profile of the rotation of the horizontal dumbbell through a 180° rotation starting from a minimized structure.

Configurations generated by FF-NEMD simulations containing dumbbells were used as inputs for geometry optimizations. The resulting configurations maintained the dumbbells and displacement of the adjacent nitrogen atoms towards the dumbbell as seen in the FF-NEMD data. The vacancies on the regular Li(2) sites were stabilized by the movement of the three coordinating Li(2) atoms towards the vacancy.

4.5.6 Macroscopic Diffusion

It has been shown that lithium diffusion in the xy plane is much faster than lithium diffusion perpendicular to the xy plane. The trajectory of a single Li(2) atom is shown in Fig. 4.18 and Movie 4.6†. The lithium atom moves approximately 32.94 Å parallel to [100] the direction of the colour field over the 100 ps of the simulation. The trace shows many Li(2) - Li(2) nearest-neighbour hops with little movement out of the Li_2N plane. There are only three hops that involve movement by $\pm c/4$ from the Li_2N plane. The first out of plane hop is the formation of a vertical dumbbell about a Li(2) site and has been described in Section 4.5.2.

The lithium diffusion parallel to the z direction is much slower than in the xy plane. The trajectory of a single lithium atom, which starts on a Li(1) site and finishes on a Li(2) site, is shown in Fig. 4.19 and Movie 4.7†. The trace show a series of a short-lived dumbbell-mediated interlayer hops. The lithium atom moves approximately 13.5 Å parallel to the direction of the colour field, [001].

The trajectories of all the lithium and nitrogen atoms in the supercell during a 10 ps time period are shown in Fig. 4.20a and 4.20b. The view along [001] (Fig. 4.20a) shows hexagons formed with Li(2) sites at the vertices. This suggests a high degree of diffusion along the Li(2) - Li(2) nearest-neighbour pathways in the Li_2N plane. The points around the Li(1) sites inside the hexagons are due to the formation of horizontal dumbbells around the Li(1) site. The [010] projection (Fig. 4.20b) shows the paths of lithium atoms exchanging back and forth between Li(1) and Li(2) sites. The lithium atom traces also show movement into and occupation of $\pm c/4$ of the Li_2N layer. Figs. 4.20a and 4.20b also show that the nitrogen atoms remain on their regular lattice sites; there is no nitrogen diffusion.

The trajectories of all lithium atoms for an entire 100 ps NEMD simulation were used to create density plots, Fig. 4.21a and 4.21b. Fig. 4.21a shows the logarithm of the lithium number density for a thin slab normal to [001] and containing the Li(1) sites at $c/2$. The vast majority of the density is located centrally on the regular Li(1) sites. The areas of lower, but non-zero, density around the Li(1) sites are due to dumbbell formation. Upon closer inspection, the density due to dumbbell formation approximates to a hexagon. There is greater density located at the vertices, compared to the midpoint of the edges of the hexagons. The hexagon is offset by 30° from the hexagons formed by Li(2) sites. As mentioned earlier, the midpoint of the vector between the two lithium atoms forming

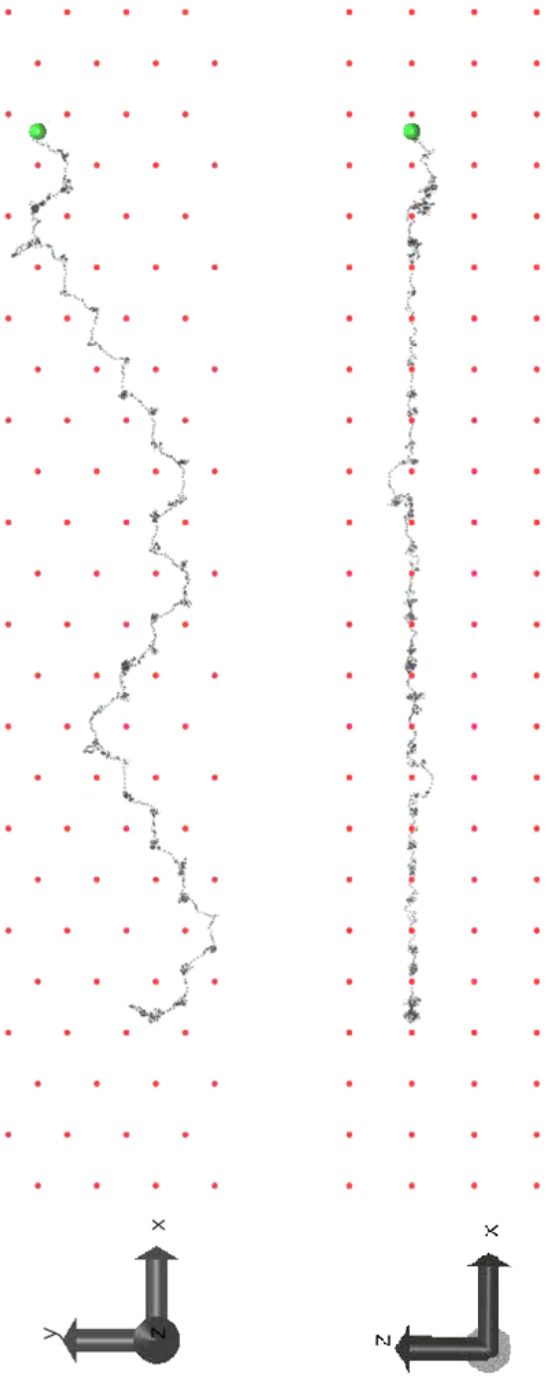


Figure 4.18: The diffusion trace of a single Li^+ cation (green) through the nitride sublattice (red) over a period of 100 ps corresponding to Movie 4.6† viewed (a) along [001] and (b) along [010]. The colour field is aligned along [100] .

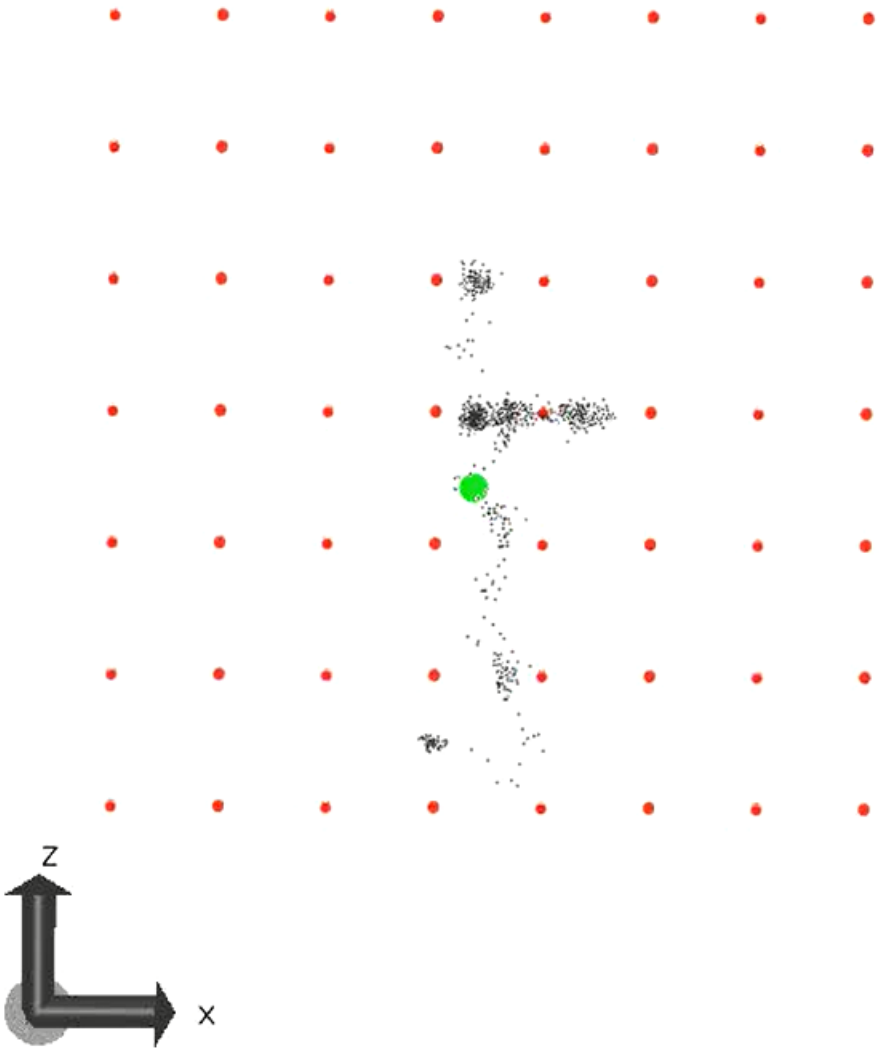
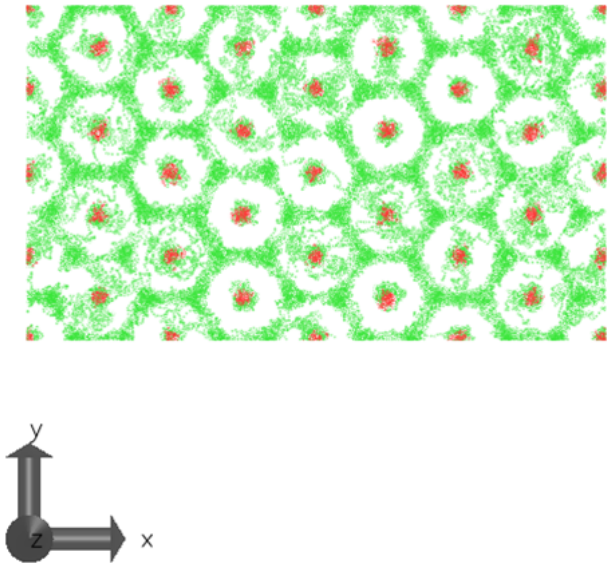
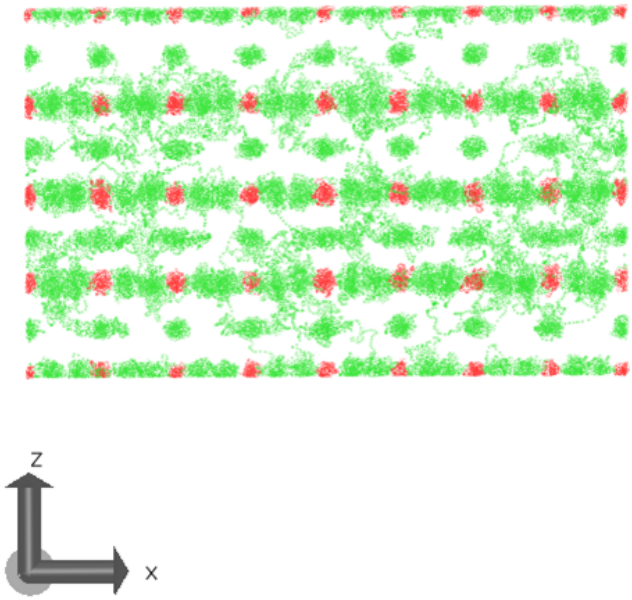


Figure 4.19: The diffusion trace of a single Li^+ cation (green) through the nitride sublattice (red) over a period of 100 ps corresponding to Movie 4.7† viewed along [010]. Each black point represents 100 fs of the Li^+ cation. The colour field is aligned along [001] .



(a)

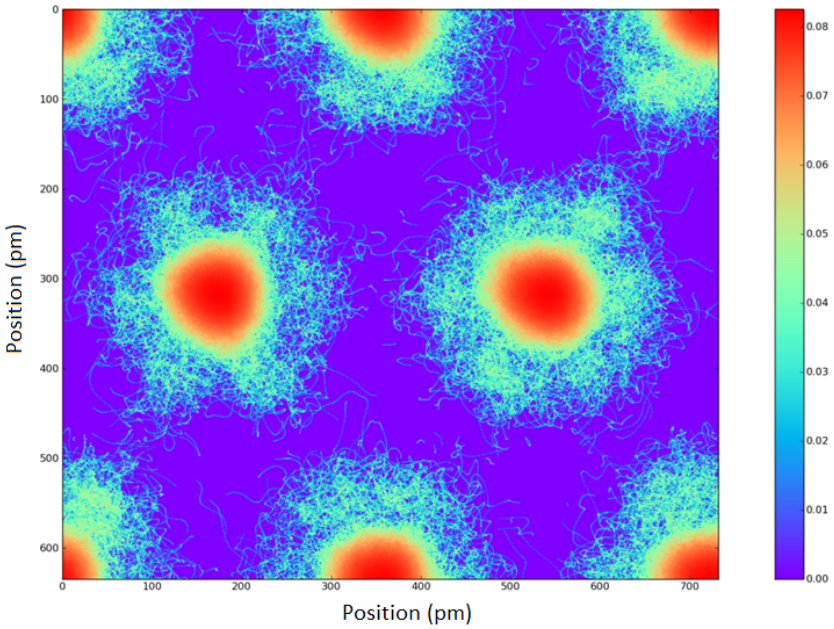


(b)

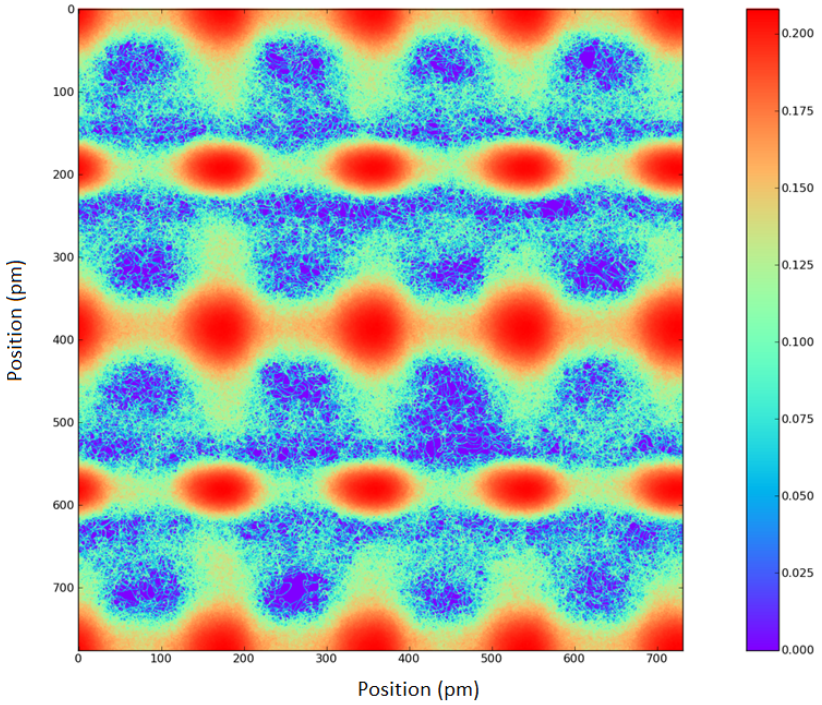
Figure 4.20: (a) [001] and (b) [010] projections of the Li (green) and N (red) distribution during the course of a 10 ps NEMD simulation. The colour field was aligned along [100] and the simulation temperatures was 200 K.

the dumbbell lies on, or close to, the Li(1) site. Therefore the lithium atoms occupy opposite vertices of the hexagon. This offset of the two hexagons allows the Li_2 dumbbell to minimize repulsive Li - Li interactions with the adjacent Li_2N layers. Fig. 4.21b shows the logarithm of lithium number density view along the [100] direction with Li_2N layers at the top, bottom, and middle of the colour map; the layers inbetween correspond to Li(1) layers. As before, the highest density relates to the regular Li(2) and Li(1) lattice sites. The Li(1) sites show a non-spherical distribution with density either side, which corresponds to formation of dumbbells. The Li(2) sites show an approximately spherical distribution. There is significant density directly between the Li(2) sites due to the frequent hopping between nearest-neighbour Li(2) sites. Density above and below the Li(2) sites is due to the formation of vertical dumbbells. The density also shows hopping $\pm c/4$ above or below the Li_2N layer.

The Li_3N crystal structure consists of alternating layers of Li_2N and Li(1). The relative lithium concentration of the Li_2N and Li(1) layers is 2:1 in the ideal crystal structure. The rapid diffusion in the Li_2N layer can explained by the presence of vacancies on the regular Li(2) lattice sites, which allows for the rapid diffusion due to the very low energy barrier for movement of a lithium ion from a Li(2) site towards an adjacent vacant Li(2) site. The existence of the vacancies has often been explained by the deliberate or non-deliberate doping with aliovalent ions. However, in this work the system was fully occupied with no vacancies or dopants used. The occupancy of the Li_2N and Li(1) layers was determined from the NEMD simulations at a range of temperatures. The unit cell was divided along the [001] direction into three equal regions about the Li(1), Li(2) and $c/4$ layers. These ranges cover the entirety of the supercell. The former contains the regular Li(1) sites and any horizontal dumbbells formed. The $c/4$ layer contains cations involved in interlayer hopping and the formation of vertical dumbbells. The positions determined from the NEMD simulations were used to determine in which region each lithium cation was located. The resulting time-averaged lithium content of each layer is shown in Fig. 4.22. This shows an increase in occupation of the Li(1) layer and the $c/4$ layer as temperature increases and a corresponding decrease in occupation of the Li(2) layer. The increased number of vacant Li(2) sites explains why the diffusion in the xy plane increases with increasing temperature. The ideal lithium content of the Li(2) layer is two atoms per formula unit and the under-occupation at all temperatures explains the elevated diffusion in the xy plane. The displaced lithium atoms are accommodated $c/4$ above the Li_2N layer and in the Li(1) layer, which have lithium contents above ideal values of zero and one lithium ions per formula



(a)



(b)

Figure 4.21: Sections through the lithium density distribution shown in Fig. 4.20 projected into a single unit cell (a) along [001] showing only Li(1) sites and (b) along [100] showing both Li(1) and Li(2) sites. Note the logarithmic scale bar.

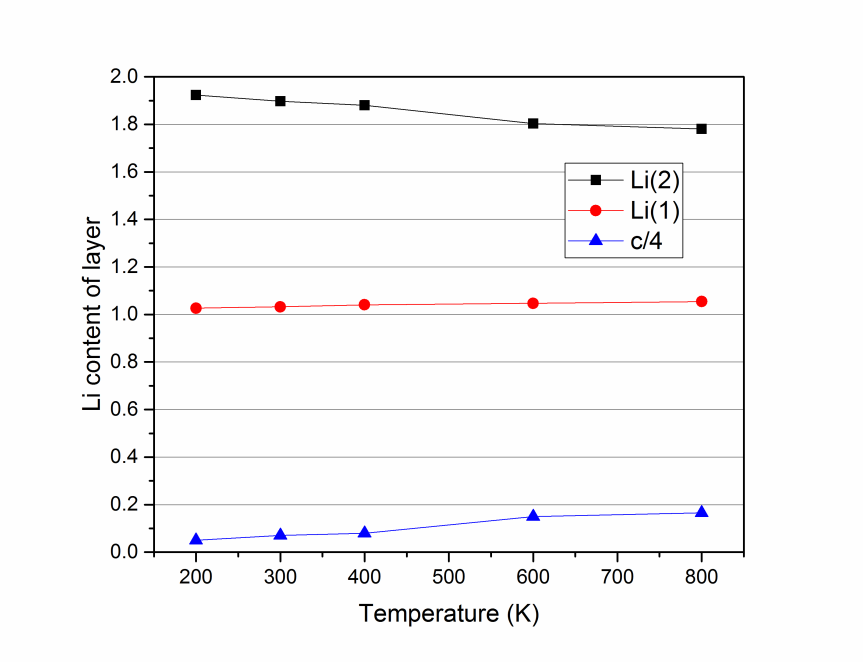
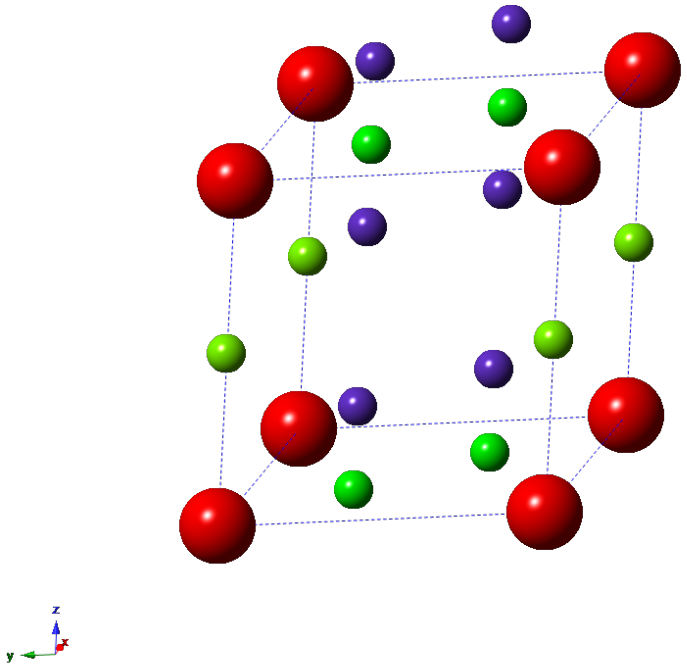
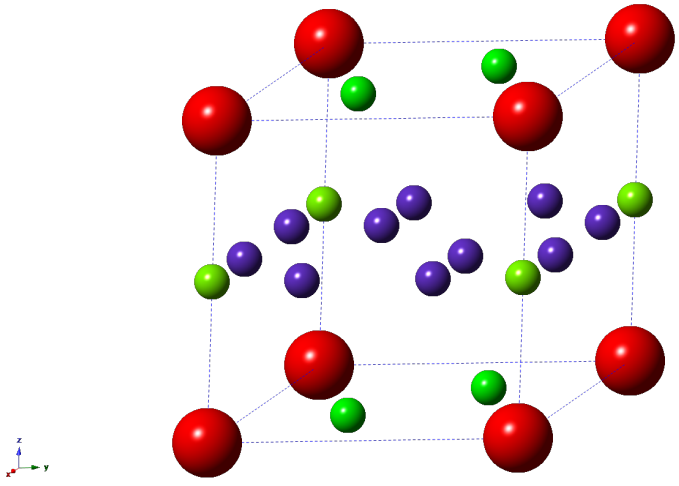


Figure 4.22: The temperature dependence of the time-averaged lithium content of each layer.

unit, respectively, for all temperatures simulated. We suggest the excess lithium atoms form vertical and horizontal dumbbells about the Li(2) and Li(1) sites, respectively. Therefore, we predict the presence of interstitial lithium atoms at the positions appropriate to dumbbell formation. The Li(2) sites lie at $(1/3, 2/3, 0)$ in the hexagonal unit cell. The presence of vertical dumbbell formation leads to occupation of sites at approximately $(1/3, 2/3, 0.24)$, which are shown in Fig. 4.23a. The regular Li(1) sites are at $(0, 0, 1/2)$ and the interstitial sites due to horizontal dumbbell formation are at approximately $(0.29, 0, 1/2)$ and symmetry-related sites. There are six such sites forming a hexagon about the Li(1) site. These are shown in Fig. 4.23b. As the thermal energy increases, the formation of dumbbells on both the Li(1) and Li(2) sites becomes more probable. The definitions of the layers used to determine these occupancy values could be considered to be arbitrary. Thinner slabs were tested to describe the Li_2N and Li(1) planes, but the results were similar. The exact definition of the planes may affect the absolute value of the occupancy ratio, and therefore the lithium content of each plane, but their temperature dependence should not change significantly with a change in the plane definition.



(a)



(b)

Figure 4.23: The hexagonal unit cell of Li_3N showing the interstitial sites for (a) the vertical dumbbell formation about Li(2) sites and (b) horizontal dumbbell formation about Li(1) sites; green spheres represent lithium atoms on regular sites, blue spheres represent lithium interstitial sites and the red spheres represent nitrogen atoms.

4.6 Conclusion

Previous investigations, both experimental and computational, have tried to measure and model the diffusion of Li_3N with limited success. Discrepancies between the computed and experimental results have often been explained by suggesting that the samples were impure. The diffusion in the xy plane has been explained by invoking the direct low-energy pathway between nearest-neighbour Li(2) sites, but to account for the very fast diffusivity, there must be vacancies on the Li(2) sites. The existence of these has often been explained by assuming the presence of aliovalent dopants. However, when efforts have been made to ensure the purity of samples (Wang et al., 2012), high diffusivity has still been observed in the xy plane. This is not to discount the importance of stoichiometric defects on the diffusion, but these alone do not explain diffusion in Li_3N. The comparison of computational and experimental data is limited by the temperature range of measured diffusion coefficient data available. This makes the level of agreement reported in Section 3.5.3 unobtainable in the case of Li_3N. Past computational studies have struggled to agree with experimental data, but have begun to elucidate the microscopic pathways involved. The early computational studies by Taylor et al. (1981); Wolf et al. (1984); Wolf and Catlow (1984); Ihara and Suzuki (1985) analysed the individual lithium atom trajectories, and despite the limited computational resources available at the time, showed the direct Li(2) - Li(2) hopping and, to a degree, the movement between Li(1) - Li(2) sites, which have been observed in the simulations presented in this thesis. The operation of ring-like motion in the Li_2N layer predicted by Ihara and Suzuki (1985) has not been seen. The MD study performed by Sarnthein et al. (1996) on a lithium-deficient Li_3N supercell managed to extend the understanding about the underlying diffusion processes. The identification of site sharing around the Li(1) site, i.e. horizontal-dumbbell formation, was observed using static calculations, but not as an emergent mechanism from MD. The work did not elucidate the orientation and the relevant dynamics of the dumbbell. By starting with a non-stoichiometric system the need for vacancy formation was removed, and merely the movement of the artificial vacancy throughout the supercell was observed.

The simulations presented in this thesis manage to go beyond any previous computational studies. The temperature range spanned by the calculated diffusion coefficients is much greater than that considered in earlier studies. The agreement with the best available experimental data is better than previously achieved. This has been achieved without invoking non-stoichiometry. The microscopic diffusion processes have been identified and characterized to a greater extent than in previous studies.

The simulations presented in this thesis are the first to use the NEMD method to model the diffusion in Li_3N. The use of colour fields, as implemented in NEMD, increases the frequency of the diffusion events in a predictable manner allowing for the modelling of slower diffusion than has been previously possible. The direction of the applied colour field determines the direction of the measured diffusion. This allows studying the diffusion of an anisotropic system, such as Li_3N, much easier.

The mechanistic detail determined from the simulations presented in this thesis goes beyond what has previously been achieved. The formation of both the horizontal dumbbell and the previously-unobserved vertical dumbbell, which forms about the Li(2) site, have been characterized in detail. The formation of these dumbbells allows for the presence of vacancies on the Li(2) sites, and thus explains the elevated diffusion in the xy plane. The horizontal dumbbell forming about the Li(1) site has been observed in MD simulations and subsequently the dynamics and symmetry have been studied. The dumbbell was optimised using both force-field and DFT methods. The results showed the stability and geometry of the dumbbell. The optimised separations present in the dumbbell were very similar to the separations present between nearest-neighbours in the equilibrium structure. The energy profile was calculated for the rotation of the horizontal dumbbell and agreed with the dynamics and symmetry observed in the NEMD data. We have predicted the occupation by lithium of the sites corresponding to the two types of dumbbell formed, with an accompanying lithium deficiency on the Li(2) sites. Currently, there is no mention in the experimental literature of the presence of lithium on the dumbbell sites, but the under-occupation of the Li(2) sites has been observed (Schulz and Schwarz, 1978). The lithium content of both the $c/4$ and the Li(1) layer increases as the temperature increases and there is an accompanying decrease in the lithium content of the Li(2) layer. This increase in vacancy concentration on the Li(2) layer accounts for the increase in diffusivity in the xy plane, but also accounts for the significant increase in diffusion parallel to the z axis. The diffusion parallel to the z axis is dominated by the Li(1) - Li(2) pathway and with the increased occupation of the $c/4$ and Li(1) layers. It can be concluded that the Li(1) - Li(2) interchange is much more frequent. Bechtold-Schweickert et al. (1984) measured the hopping rate between the Li(1) and Li(2) sites and showed the increase in the rate of exchange as temperature increases. Li(2) - Li(2) diffusion between Li_2N layers has also been identified, but it is a minor contribution to the overall diffusion parallel to the z axis. The movement between layers is mediated by the Li(1) site either by the formation of horizontal dumbbells or by the very short-lived dumbbell formation.

The work described in this chapter is the basis for the published article:

A. D. Mulliner, P. D. Battle, W. I. F. David and K. Refson

Dimer-mediated cation diffusion in the stoichiometric ionic conductor Li_3N

Physical Chemistry Chemical Physics, 2016, **18**, 5605.

CHAPTER 5

Conclusion and Outlook

Despite much research, both computational and experimental, our understanding of solid-state diffusion is still limited. Molecular dynamics, using just the interatomic forces and the classical equations of motion, allows the modelling of diffusion as an emergent property on an atom-by-atom level. The MD method can give direct access to the structure and dynamics of a system that cannot be obtained with direct experimental observations. The MD simulations also allow for the calculation of macroscopic diffusion coefficients, and other transport coefficients, which can be compared to experimental results to give validity to the computational model.

In Chapter 3, conventional MD was shown to be limited to very high temperatures and correspondingly high diffusion coefficients. The use and implementation of FF-NEMD, for the first time, allowed the diffusion of Li_2O to be modelled to much lower temperatures than previously achieved. The FF-NEMD technique not only extends the operational range of MD, but also retains the ability to elucidate the underlying diffusion processes. In the case of Li_2O, the temperature dependence of the diffusion coefficient has been modelled and the results are in excellent agreement with experimental data over a very wide temperature range, including the change from the non-superionic to the superionic regime. This level of agreement surpasses that achieved in previous studies, and by using FF-NEMD the mechanistic details underpinning the diffusion have been elucidated. The change from diffusion dominated by a concerted mechanism to diffusion driven by an interstitial mechanism has been identified. This study shows how viable the FF-NEMD method is for modelling diffusion. The success in the case of Li_2O over a wide range of temperatures is due to the ability to model multiple diffusion mechanisms simultaneously; especially their relative contributions to the macroscopic diffusion. The work presented in Chapter 4 again showed the efficacy of FF-NEMD and the ability to go beyond what has previously been attainable. The results of the simulations performed on Li_3N show better agreement with experimental work than has been previously achieved in conventional MD studies. The understanding of the mechanism of the diffusion processes is revealed in more

detail than previously. The diffusion coefficients measured in both the xy plane and perpendicular to the xy plane have been calculated to much lower temperatures than was previously achieved with MD. NEMD extends the lower limit of diffusivity that can be modelled compared to equilibrium MD, whilst maintaining diffusion as an emergent property.

It is worth making an explicit comparison of the two systems studied. Li_2O adopts the well-known and common anti-fluorite structure and exhibits similar properties to many other fluorite systems (Section 3.1). Li_3N adopts a unique structure of layered hexagonal structure that is not adopted by any other system. There are many more known compounds with the stoichiometry MX_2 than with MX_3. The underlying processes involved in Li-ion diffusion in Li_2O are similar to those found in other anti-fluorite and fluorite-structured compounds as noted in Section 3.1. The layered structure of Li_3N gives rise to anisotropic diffusion coefficients with very high rates of diffusion in the ab plane, more specifically in the Li_2N plane itself by direct movement between Li(2) sites, whereas the diffusion perpendicular to the ab plane is much slower. The diffusion perpendicular to the ab plane is dependent on the interchange between Li(2) and Li(1) sites, which is much slower as measured in NMR studies (Bechtold-Schweickert et al., 1984; Wang et al., 2012). The bonding present in α-Li_3N is considered to be highly ionic and this material, along with the high pressure phases of Li_3N, is the best example of a compound containing an N^{3-} ion, which is not a stable free-ion. The unique structure of Li_3N is driven by the need to stabilize the N^{3-} ion. This leads to an N^{3-} ion 8-coordinated by Li^+ ions and hence to the uniqueness of the structure. The difference between the interatomic interaction potentials is responsible for the adoption of markedly different crystal structures and hence the different diffusion properties. Both systems exhibit very fast rates of Li-ion diffusion, but this is achieved in Li_2O only at elevated temperatures, whereas in Li_3N a rapid rate of diffusion is observed at significantly lower temperatures. Li_2O and Li_3N are both fully stoichiometric systems and diffusion is dominated in both cases by the rapid movement of a vacancy between regular sites. The high energy-barrier process of creating an octahedral-interstitial in Li_2O allows for vacancy diffusion with a relatively low energy barrier between adjacent regular lithium sites. Similarly, in Li_3N the high energy-barrier process of creating a dumbbell creates a vacancy on a Li(2) site, which can diffuse very quickly within the Li_2N layer. However, the high energy Li(1)-Li(2) interchange is not accompanied by the creation of a facile diffusion process along [001], thus explaining why diffusion perpendicular to the plane is much slower. The Li_2O system creates the vacancy through the well-known method of a Frenkel defect, which is observed in fluorite structures,

where as in Li_3N the dominant N-N repulsion gives rise to the formation of Li–Li dumbbells in order to effectively screen the N-N interactions. The O^{2-} anion in Li_2O does not require such stabilization as an N^{3-} anion and the formation of dumbbells, which would significantly distort the structure, does not occur.

5.1 Future Work

Aeberhard et al. (2012) showed how DFT-NEMD could be used to model diffusion in a solid-state ionic conductor. The work in this thesis expands upon this to include FF-NEMD as a method for modelling diffusion, but it has also explored the temperature dependence of diffusivity over very wide temperature ranges compared to most previous computational investigations. The expanded range of diffusivity accessible with NEMD allows for the study of the diffusion properties of many solid-state materials, which have previously been considered to be out of reach using traditional MD-based methods and only sometimes accessible using TST based methods. This is clearly an area where NEMD can be used to investigate not only the technological efficacy of such materials, but also the underlying fundamental scientific processes involved.

As mentioned in the discussion of NEMD (Section 2.12), the synthetic algorithms are similar for all transport properties. Given the successful use of the diffusion algorithms, an analogous implementation for heat transport, or thermal conductivity, should be relatively straightforward. The understanding of thermal conductivity is of significant importance for many materials regarding their implementation in technological applications. These include heat dissipation in hydrogen-storage materials and batteries during the charge-discharge cycle.

The systems studied in this thesis are fully stoichiometric and start initially with an ideal crystal structure. However, the role of defects on the diffusion properties is a well-established principle. Simulating systems with defects, whether structural, stoichiometric, or dopant-based can be performed using NEMD. In the specific cases of materials used for technological applications, especially battery materials, one major concern is structural degradation; for example, channel blocking in the one-dimensional lithium-ion conductor $LiFePO_4$. In order to model the defect formation, random structure searching techniques such as AIRSS (Pickard and Needs, 2009) could be used to determine possible low energy structures of defects, whether it is a foreign ion blocking a channel or aliovalent doping creating vacancies throughout the structure. These low-energy defect structures could then be input into NEMD simulations. Using the direction of the colour field and the ability to assign

colour charges to particular atoms, the effect such defects have on the diffusion could be probed in a direct manner. The direction of the colour field could be reversed, or changed, to simulate charge-discharge cycles of such materials. Such a combination of AIRSS and NEMD would give real insight into the effect of diffusion, both locally around the defect and throughout the rest of the structure. It would consequently facilitate the development of technologically important materials.

References

A. D. MacKerell, J., Bashford, D., Bellott, M., R. L. Dunbrack, J., Evanseck, J. D., Field, M. J., Fischer, S., Gao, J., Guo, H., Ha, S., Joseph-McCarthy, D., Kuchnir, L., Kuczera, K., Lau, F. T. K., Mattos, C., Michnick, S., Ngo, T., Nguyen, D. T., Prodhom, B., Reiher, W. E., Roux, B., Schlenkrich, M., Smith, J. C., Stote, R., Straub, J., Watanabe, M., Wiorkiewicz-Kuczera, J., Yin, D., Karplus, M., 1998. All-atom empirical potential for molecular modeling and dynamics studies of proteins. The Journal of Physical Chemistry B 102 (18), 3586–3616.

Aeberhard, P., Williams, S., Evans, D., Refson, K., David, W. I. F., 2012. *Ab initio* Nonequilibrium Molecular Dynamics in the Solid Superionic Conductor $LiBH_4$. Physical Review Letters 108 (9), 1–5.

Akiyama, M., Ando, K., Oishi, Y., 1981. The self-diffusion coefficient of the oxygen ion in antifluorite-cubic lithium oxide has been determined by means of. Solid State Ionics 4, 3–6.

Alpen, U. v., 1979. Li_3N: A promising Li ionic conductor. Journal of Solid State Chemistry 29 (3), 379–392.

Alpen, U. v., Rabenau, A., Talat, G. H., 1977. Ionic conductivity in Li_3N single crystals. Applied Physics Letters 30 (12).

Armand, M. B., Chabagno, J. M., Duclot, M. J., 1979. Fast Ion Transport in Solids - Electrodes and Electrolytes. North-Holland.

Bardeen, J., Herring, C., 1951. Atom Movements. A. S. M. Cleveland.

Bardeen, J., Herring, C., 1952. Imperfections in Nearly Perfect Solids. Wiley, New York.

Battle, P. D., Grey, C. P., Hervieu, M., Martin, C., Moore, C. A., Paik, Y., 2003. Structural chemistry and magnetic properties of La_2LiRuO_6. Journal of Solid State Chemistry 175 (1), 20–26.

Bechtold-Schweickert, E., Mali, M., Roos, J., Brinkmann, D., 1984. ^{7}Li diffusion constant in the superionic conductor Li_3N measured by NMR. Physical Review B 30 (5), 2891–2893.

Beister, H. J., Haag, S., Kniep, R., Strössner, K., Syassen, K., 1988. Phase Transformations of Lithium Nitride under Pressure. Angewandte Chemie International Edition in English 27 (8), 1101–1103.

Bell, M. F., Breitschwerdt, A., Alpen, U. v., 1981. The effect of hydrogen on the ionic conductivity in lithium nitride. Materials Research Bulletin 16 (3), 267–272.

Blöchl, P. E., 1990. Generalized separable potentials for electronic-structure calculations. Physical Review B 41 (8), 5414–5416.

Blomqvist, A., Moysés Araújo, C., Scheicher, R. H., Srepusharawoot, P., Li, W., Chen, P., Ahuja, R., 2010. Hydrogen as promoter and inhibitor of superionicity: A case study on Li-N-H systems. Physical Review B 82 (2), 24304.

Borg, R. J., Dienes, G. J., 2012. An Introduction to Solid State Diffusion. Elsevier.

Born, M., Lande, A., 1918. Verhandlungen der Deutschen Physik Gesellschaf 21/24, 210.

Born, M., Mayer, J. E., 1932. Zeitschrift für Physik 75, 1.

Boukamp, B. A., Huggins, R. A., 1976. Lithium ion conductivity in lithium nitride. Physics Letters A 58 (4), 231–233.

Boulfelfel, S. E., Seifert, G., Leoni, S., 2011. Atomistic investigation of Li^+ diffusion pathways in the olivine $LiFePO_4$ cathode material. Journal of Materials Chemistry 21 (41), 16365–16372.

Boyce, J. B., Huberman, B. A., 1979. Superionic conductors: Transitions, structures, dynamics. Physics Reports 51 (4), 189–265.

Brinkmann, D., Mali, M., Roos, J., Messer, R., Birli, H., 1982. Diffusion processes in the superionic conductor Li_3N: An NMR study. Physical Review B 26 (9), 4810–4825.

Brophy, J. H., Rose, R. M., Wulff, J., 1964. The Structure and Properties of Materials, Vol. 2: Thermodynamics of Structure. John Wiley and Sons, Inc., New York.

Buckingham, R. A., 1938. The Classical Equation of State of Gaseous Helium, Neon and Argon. Proceedings of the Royal Society of London A: Mathematical, Physical and Engineering Sciences 168 (933), 264–283.

Burbano, M., Norberg, S. T., Hull, S., Eriksson, S. G., Marrocchelli, D., Madden, P. A., Watson, G. W., 2012. Oxygen Vacancy Ordering and the Conductivity Maximum in Y_2O_3-Doped CeO_2. Chemistry of Materials 24 (1), 222–229.

Castleton, C. W. M., Mirbt, S., 2004. Finite-size scaling as a cure for supercell approximation errors in calculations of neutral native defects in InP. Physical Review B 70, 195202.

Catlow, C. R. A., Comins, J. D., Germano, F. A., Harley, R. T., Hayes, W., 1978. Brillouin scattering and theoretical studies of high-temperature disorder in fluorite crystals. Journal of Physics C: Solid State Physics 11 (15), 3197.

Ceperley, D. M., Alder, B. J., 1980. Ground State of the Electron Gas by a Stochastic Method. Physical Review Letters 45 (7), 566–569.

Chandrasekhar, H. R., Bhattacharya, G., Migoni, R., Bilz, H., Jan 1978. Infrared and raman spectra and lattice dynamics of the superionic conductor li_3n. Phys. Rev. B 17, 884–893.

Ciccotti, G., Tenenbaum, A., 1980. Canonical ensemble and nonequilibrium states by molecular dynamics. Journal of Statistical Physics 23 (6), 767–772.

Clark, S. J., Segall, M. D., Pickard, C. J., Hasnip, P. J., Probert, M. I. J., Refson, K., Payne, M. C., 2005. First principles methods using CASTEP. Zeitschrift für Kristallographie - Crystalline Materials 220, 567–570.

Cui, S., Feng, W., Hu, H., Feng, Z., Wang, Y., 2009. Structural transition of Li_3N under high pressure: A first-principles study. Solid State Communications 149 (15-16), 612–615.

Davidson, E., Chakravorty, S., 1992. A test of the Hirshfeld definition of atomic charges and moments. Theoretica Chimica Acta 83 (5-6), 319–330.

De Vita, A., Gillan, M. J., Lin, J. S., Payne, M. C., Stich, I., Clarke, L. J., 1992a. Defect energetics in oxide materials from first principles. Physical Review Letters 68 (22), 3319–3322.

De Vita, A., Manassidis, I., Lin, J. S., Gillan, M. J., 1992b. The Energetics of Frenkel Defects in Li_2O from First Principles. EPL (Europhysics Letters) 19 (7), 605.

Dickens, M. H., Hayes, W., Hutchings, M. T., Kleppmann, W. G., 1979. Neutron scattering studies of acoustic phonon modes in PbF_2 up to high temperatures. Journal of Physics C: Solid State Physics 12 (1), 17.

Dickens, M. H., Hayes, W., Schnabel, P., Hutchings, M. T., Lechner, R. E., Renker, B., 1983. Incoherent quasielastic neutron scattering investigation of chlorine ion hopping in the fast-ion phase of strontium chloride. Journal of Physics C: Solid State Physics 16 (1), L1.

Dovesi, R., Roetti, C., Prencipe, M., Saunders, V. R., 1991. On the elastic properties of lithium , sodium and potassium oxide . An *ab initio* study. Science 156, 11–19.

Duan, Y., Sorescu, D., 2009. Density functional theory studies of the structural, electronic, and phonon properties of Li_2O and Li_2CO_3: Application to CO_2 capture reaction. Physical Review B 79 (1), 1–18.

Elcombe, M. M., Pryor, A. W., 1970. The lattice dynamics of calcium fluoride. Journal of Physics C: Solid State Physics 3 (3), 492.

Evans, D. J., 1979. The frequency dependent shear viscosity of methane. Molecular Physics 37 (6), 1745–1754.

Evans, D. J., 1982. Homogeneous NEMD algorithm for thermal conductivity - Application of non-canonical linear response theory. Physics Letters A 91 (9), 457–460.

Evans, D. J., Hoover, G., Failor, B. H., Moran, B., Ladd, A. J. C., 1983. Nonequilibrium molecular dynamics via Guass's principle of least constraint. Physical Review A 28 (2).

Evans, D. J., Morriss, G., 2008. Statistical Mechanics Of Nonequilibrium Liquids. Cambridge University Press.

Evans, D. J., Morriss, G. P., 1984. Nonlinear-response theory for steady planar Couette flow. Physical Review A 30 (3), 1528–1530.

Faraday, M., 1939. Experimental Researches in Electricity. R. and J. E. Taylor, London.

Farley, T. W. D., Hayes, W., Hull, S., Hutchings, M. T., Vrtis, M., 1991. Investigation of thermally induced Li^+ ion disorder in Li_2O using neutron diffraction. Journal of Physics: Condensed Matter 3 (26), 4761–4781.

Farrell, D. E., Shin, D., Wolverton, C., 2009. First-principles molecular dynamics study of the structure and dynamic behavior of liquid $Li_4BN_3H_{10}$. Physical Review B 80 (22), 224201.

Fenton, D. E., Parker, J. M., Wright, P. V., 1973. Complexes of alkali metal ions with poly(ethylene oxide). Polymer 14 (11), 589.

Fick, A., 1855. Ueber Diffusion. Annalen der Physik 170 (1), 59–86.

Fick, A., 1995. On liquid diffusion. Journal of Membrane Science 100 (1), 33–38.

Fister, T. T., Seidler, G. T., Shirley, E. L., Vila, F. D., Rehr, J. J., Nagle, K. P., Linehan, J. C., Cross, J. O., 2008. The local electronic structure of α-Li_3N. The Journal of Chemical Physics 129 (4), 044702.

Fourier, J. B. J., 1807. On the Propagation of Heat in Solid Bodies. Paris Institute.

Fracchia, R., Barrera, G., Allan, N., Barron, T., Mackrodt, W., 1998. Lithium oxide and superionic behaviour: A study using potentials from periodic ab initio calculations. Journal of Physics and Chemistry of Solids 59 (3), 435–445.

Frenkel, J. I., 1926. Thermal movement in solid and liquid bodies. Zeitschrift für Physik 35, 652.

Gjostein, N. A., 1973. Diffusion. American Society for Metals.

Goedecker, S., Teter, M., Hutter, J., 1996. Separable dual space Gaussian pseudopotentials. Physical Review B 54 (3).

Goel, P., Choudhury, N., Chaplot, S., 2004. Superionic behavior of lithium oxide Li_2O: A lattice dynamics and molecular dynamics study. Physical Review B 70 (17), 174307.

Gordienko, A. B., 2009. Electronic structure of γ-Li_3N. Russian Physics Journal 52 (9), 978–983.

Graham, T., 1829. A short Account of Experimental Researches on the Diffusion of Gases through each other, and their Separation by Mechanical Means. Quaterly Journal of Science, Literature and Art 27, 74.

Graham, T., 1833. On the law of the diffusion of gases. Philosophical Magazine 2, 269–276.

Graham, T., 1850. The Bakerian Lecture: On the Diffusion of Liquids. Philosophical Transactions of the Royal Society of London 140, 1–46.

Gregory, D. H., 2001. Nitride chemistry of the s-block elements. Coordination Chemistry Reviews 215 (1), 301 – 345.

Gregory, D. H., O'Meara, P. M., Gordon, A. G., Hodges, J. P., Short, S., Jorgensen, J. D., 2002. Structure of Lithium Nitride and Transition-Metal-Doped Derivatives, $Li_{3-x-y}M_xN$ (M = Ni, Cu): A Powder Neutron Diffraction Study. Chemistry of Materials 14 (5), 2063–2070.

Gupta, M. K., Goel, P., Mittal, R., Choudhury, N., Chaplot, S. L., 2012. Phonon instability and mechanism of superionic conduction in Li_2O. Physical Review B 85 (18), 184304.

Haas, P., Tran, F., Blaha, P., 2009. Calculation of the lattice constant of solids with semilocal functionals. Physical Review B 79 (8), 85104.

Haile, J. M., 1997. Molecular Dynamics Simulation. Wiley-Interscience.

Harries, D. R., Dupouy, J.-M., Wu, C. H., 1985. Materials research and development for NET. Journal of Nuclear Materials 133-134, 25–31.

Hayoun, M., Meyer, M., 2008. Migration and correlation in highly defective systems: Fast-diffusion in lithium oxide. Acta Materialia 56 (6), 1366–1373.

Hayoun, M., Meyer, M., 2013. Surface effects on atomic diffusion in a superionic conductor: A molecular dynamics study of lithium oxide. Surface Science 607, 118–123.

Hayoun, M., Meyer, M., Denieport, A., 2005. Complex atomic-diffusion mechanism in ionic superconductors: The case of the lithium-oxide antifluorite. Acta Materialia 53 (10), 2867–2874.

Heffelfinger, G. S., van Swol, F., 1994. Diffusion in Lennard-Jones fluids using dual control volume grand canonical molecular dynamics simulation (DCV-GCMD). The Journal of Chemical Physics 100 (10).

Heitjans, M. W., Gebauer, D., Paul, 2008. Diffusion parameters in single-crystalline Li_3N as probed by ^6Li and ^7Li spin-alignment echo NMR spectroscopy in comparison with results from ^8Li β-radiation detected NMR. Journal of Physics: Condensed Matter 20 (2), 22201.

Henkelman, G., Jonsson, H., 2000. Improved tangent estimate in the nudged elastic band method for finding minimum energy paths and saddle points. The Journal of Chemical Physics 113 (22), 9978–9985.

Henkelman, G., Uberuaga, B. P., Jonsson, H., 2000. A climbing image nudged elastic band method for finding saddle points and minimum energy paths. The Journal of Chemical Physics 113 (22), 9901–9904.

Herman, F., Van Dyke, J. P., Ortenburger, I. B., 1969. Improved statistical exchange approximation for inhomogeneous many-electron systems. Phys. Rev. Lett. 22, 807–811.

Hill, T. L., 1986. An Introduction to Statistical Thermodynamics. Dover Publications Inc., New York.

Ho, A. C., Granger, M. K., Ruoff, A. L., Van Camp, P. E., Van Doren, V. E., 1999. Experimental and theoretical study of Li_3N at high pressure. Physical Review B 59 (9), 6083–6086.

Hofmann, M., Hull, S., McIntyre, G. J., Wilson, C. C., 1997. A neutron diffraction study of the superionic transition in $Ca_{1-x}Y_xF_{2+x}$ with x = 0.06. Journal of Physics: Condensed Matter 9 (4), 845.

Hohenberg, P., Kohn, W., 1964. Inhomogeneous electron gas. Physical Review 136, B864–B871.

Hull, S., 2004. Superionics: crystal structures and conduction processes. Reports on Progress in Physics 67 (7), 1233.

Hull, S., Farley, T. W. D., Hayes, W., Hutchings, M. T., 1988. The elastic properties of lithium oxide and their variation with temperature. Journal of Nuclear Materials 160 (2), 125–134.

Huq, A., Richardson, J. W., Maxey, E. R., Chandra, D., Chien, W. M., 2007. Structural studies of Li_3N using neutron powder diffraction. Journal of Alloys and Compounds 436 (1-2), 256–260.

Ihara, S., Suzuki, K., 1985. Molecular Duynamics Study of Li_3N. Physics Letters A 110 (5), 265–268.

Islam, M. S., Driscoll, D. J., Fisher, C. A. J., Slater, P. R., 2005. Atomic-Scale Investigation of Defects, Dopants, and Lithium Transport in the $LiFePO_4$ Olivine-Type Battery Material. Chemistry of Materials 17 (20), 5085–5092.

Ivanov-Shitz, A. K., 2007. Computer simulation of superionic conductors: I. anionic conductors: Review. Crystallography Reports 52 (1), 129–140.

Julien, C., 1990. Technological applications of solid state ionics. Materials Science and Engineering: B 6 (1), 9–28.

Kamaya, N., Homma, K., Yamakawa, Y., Hirayama, M., Kanno, R., Yonemura, M., Kamiyama, T., Kato, Y., Hama, S., Kawamoto, K., Mitsui, A., 2011. A lithium superionic conductor. Nature Materials 10 (9), 682–686.

Keen, D. A., 2002. Disordering phenomena in superionic conductors. Journal of Physics: Condensed Matter 14 (32), R819.

Kingery, W. D., Pappis, J., Doty, M. E., Hill, D. C., 1959. Oxygen ion mobility in cubic $Zr_{0.85}Ca_{0.15}O_{1.85}$. Journal of the American Ceramic Society 42, 393.

Kleppmann, W. G., 1978. High-temperature disorder and the elastic constants in fluorite crystals. Journal of Physics C: Solid State Physics 11 (3), L91.

Koch, W., Holthausen, M. C., 2001. A Chemist's Guide to Density Functional Theory. Wiley-VCH.

Kohn, W., Sham, L. J., 1965. Self-Consistent Equations Including Exchange and Correlation Effects. Physical Review 140 (4A), 1133.

Kress, W., Grimm, H., Press, W., Lefebvre, J., 1980. Lattice vibrations in lithium nitride, li_3n. Phys. Rev. B 22, 4620–4625.

Kulcinski, G. L., Dupouy, J. M., Ishino, E., 1986. Key materials issues for near term fusion reactors. Journal of Nuclear Materials 141, 3–9.

Kumar, B., Kumar, J., Leese, R., Fellner, J. P., Rodrigues, S. J., Abraham, K. M., 2010a. A Solid-State, Rechargeable, Long Cycle Life Lithium-Air Battery. Journal of The Electrochemical Society 157 (1), A50.

Kumar, B., Thomas, D., Kumar, J., 2009. Space-Charge-Mediated Superionic Transport in Lithium Ion Conducting Glass-Ceramics. Journal of The Electrochemical Society 156 (7), A506.

Kumar, J., Rodrigues, S. J., Kumar, B., 2010b. Interface-mediated electrochemical effects in lithium/polymer-ceramic cells. Journal of Power Sources 195 (1), 327–334.

Kumar, P. P., Yashonath, S., 2006. Ionic conduction in the solid state. Journal of Chemical Sciences 118 (1), 135–154.

Kummer, J. T., 1972. β-Alumina electrolytes. Progress in Solid State Chemistry 7, 141–175.

Laio, A., Gervasio, F. L., 2008. Metadynamics: a method to simulate rare events and reconstruct the free energy in biophysics, chemistry and material science. Reports on Progress in Physics 71 (12), 126601.

Laio, A., Parrinello, M., 2002. Escaping free-energy minima. Proceedings of the National Academy of Sciences 99 (20), 12562–12566.

Lapp, T., Skaarup, S., Hooper, A., 1983. Ionic conductivity of pure and doped Li_3N. Solid State Ionics 11 (2), 97–103.

Laskar, A. L., 1990. Diffusion in Materials. Kluwer Academic Publishers.

Lazicki, A., Maddox, B., Evans, W. J., Yoo, C.-S., McMahan, A. K., Pickett, W. E., Scalettar, R. T., Hu, M. Y., Chow, P., 2005. New Cubic Phase of Li_3N: Stability of the N^{3-} Ion to 200 GPa. Physical Review Letters 95 (16), 165503.

Lennard-Jones, J. E., 1924. On the Determination of Molecular Fields. Proceedings of the Royal Society London A 106, 463.

Levy, M., 1979. Universal variational functionals of electron densities, first-order density matrices, and natural spin-orbitals and solution of the v-representability problem. Proceedings of the National Academy of Sciences 76 (12), 6062–6065.

Levy, M., 1982. Electron densities in search of Hamiltonians. Physical Review A 26 (3), 1200–1208.

Lieb, E., 2002. Density Functionals for Coulomb Systems. In: Loss, M., Ruskai, M. (Eds.), Inequalities. Springer Berlin Heidelberg, pp. 269–303.

Maginn, E. J., Bell, A. T., Theodorou, D. N., 1993. Transport diffusivity of methane in silicalite from equilibrium and nonequilibrium simulations. The Journal of Physical Chemistry 97 (16), 4173–4181.

Makepeace, J. W., Jones, M. O., Callear, S. K., Edwards, P. P., David, W. I. F., 2014. In situ X-ray powder diffraction studies of hydrogen storage and release in the Li-N-H system. Physical Chemistry Chemical Physics 16 (9), 4061–4070.

Marrocchelli, D., Madden, P. A., Norberg, S. T., Hull, S., 2011. Structural Disorder in Doped Zirconias, Part II: Vacancy Ordering Effects and the Conductivity Maximum. Chemistry of Materials 23 (6), 1365–1373.

Martin, G., Perraillon, B., 1975. Journal de Physique Colloques 36, 135.

Martin, R. M., 2008. Electronic Structure: Basic Theory and Methods. Cambridge University Press.

Mattsson, A. E., Schultz, P. A., Desjarlais, M. P., Mattsson, T. R., Leung, K., 2005. Designing meaningful density functional theory calculations in materials science - a primer. Modelling and Simulation in Materials Science and Engineering 13 (1), R1.

Matzke, H., 1970. Fluorine self-diffusion in CaF_2 and BaF_2. Journals of Materials Science 5 (10), 831.

Mehrer, H., 1978. Atomic jump processes in self-diffusion. Journal of Nuclear Materials 69-70, 38–60.

Mehrer, H., 2007. Diffusion in Solids: Fundamentals, Methods, Materials, Diffusion-Controlled Processes. Springer.

Messer, R., Birli, H., Differt, K., 1981. NMR study of diffusion in Li_3N. Journal of Physics C: Solid State Physics 14 (20), 2731.

Morrison, F. D., Coats, A. M., Sinclair, D. C., West, A. R., 2001. Charge compensation mechanisms in la-doped batio3. Journal of Electroceramics 6 (3), 219–232.

Morriss, G. P., Evans, D. J., 1985. Isothermal response theory. Molecular Physics 54 (3), 629–636.

Mulliken, R. S., 1955. Electronic Population Analysis on LCAO-MO Molecular Wave Functions. The Journal of Chemical Physics 23 (10).

Murch, G. E., 2001. Diffusion Kinetics in Solids. In: Kostorz, G. (Ed.), Phase Transformations in Materials. WILEY-VCH Verlag, Weinheim, Ch. 3.

Ning, H., Lan, Z., Bai, J., Guo, J., 2014. Density function theory investigation on the thermodynamic properties of the Li-N-H system. Materials Chemistry and Physics 144 (3), 484–490.

Nishida, K., Asai, T., Kawai, S., 1983. Ionic conductivity and NMR relaxation study on Li_3N single crystal. Solid State Communications 48 (8), 701–704.

Noda, K., Shluger, A., Nakazawa, T., Ishii, Y., Itoh, N., 1994. Migration behavior of lithium ions and tritium in Li_2O. Nuclear Instruments and Methods in Physics Research 91, 307–311.

Nye, J. F., 1957. Physical Properrties of Crystals: their Representation by Tensors and Matrices. Clarendon, Oxford.

Oishi, Y., Kamei, Y., 1979. Self-diffusion coefficient of lithium in lithium oxide. Journal of Nuclear Materials 87, 341–344.

Panchmatia, P. M., Orera, A., Rees, G. J., Smith, M. E., Hanna, J. V., Slater, P. R., Islam, M. S., 2011. Oxygen Defects and Novel Transport Mechanisms in Apatite Ionic Conductors: Combined ^{17}O NMR and Modeling Studies. Angewandte Chemie International Edition 50 (40), 9328–9333.

Parr, R. G., Yang, W., 1989. Density-Functional Theory of Atoms and Molecules . Oxford University Press USA.

Pattison, P., Hansen, N. K., Schneider, J. R., 1984. An investigation of the electron density in Li_3N using Compton scattering. II. Acta Crystallographica Section B 40 (1), 38–44.

Pattison, P., Schneider, J. R., 1980. An investigation of the electron density in Li_3N using Compton scattering. Acta Crystallographica Section A 36 (3), 390–398.

Payne, M. C., Teter, M. P., Allan, D. C., Arias, T. A., Joannopoulos, J. D., 1992. Iterative minimization techniques for *ab initio* total-energy calculations - molecular-dynamics and conjugate gradients. Review of Modern Physics 64, 1045–1097.

Perdew, J. P., Burke, K., Ernzerhof, M., 1996. Generalized Gradient Approximation Made Simple. Physical Review Letters 77 (18), 3865–3868.

Perdew, J. P., Wang, Y., 1992. Accurate and simple analytic representation of the electron-gas correlation energy. Physical Review B 45, 13244–13249.

Peterson, N. L., 1978. Self-diffusion in pure metals. Journal of Nuclear Materials 69-70, 3–37.

Peterson, N. L., 1980. Grain Boundary Structure and Kinetics. Ohio, p. 209.

Peterson, N. L., 1983. Grain-Boundary Diffusion. International Materials Reviews 28, 65.

Pfeiffer, H., Jorge, S., Alvarez, L. J., 2000. Lithium and tritium diffusion. Journal of Nuclear Materials 280.

Pickard, C. J., Needs, R. J., 2009. Structures at high pressure from random searching. physica status solidi (b) 246 (3), 536–540.

Pickett, W. E., 1989. Pseudopotential methods in condensed matter applications. Computer Physics Reports 9 (3), 115–197.

Press, W. H., Flannery, B. P., Teukolsky, S. A., Vetterling, W. T., 1992. Numerical Recipes in Fortran 77: The Art of Scientific Computing. Cambridge University Press.

Probert, M. I. J., Payne, M. C., 2003. Improving the convergence of defect calculations in supercells: An *ab initio* study of the neutral silicon vacancy. Physical Review B 67, 075204.

Rabenau, A., 1982. Lithium nitride and related materials case study of the use of modern solid state research techniques. Solid State Ionics 6 (4), 277–293.

Roberts, R. B., White, G. K., 1986. Thermal expansion of fluorites at high temperatures. Journal of Physics C: Solid State Physics 19 (36), 7167.

Roberts-Austen, W. C., 1896. Philosophical Transactions of the Royal Society A 187, 383.

Rotenberg, B., Salanne, M., Simon, C., Vuilleumier, R., 2010. From localized orbitals to material properties: Building classical force fields for nonmetallic condensed matter systems. Physical Review Letters 104, 138301.

Sanchez-Portal, D., Artacho, E., Soler, J. M., 1995. Projection of plane-wave calculations into atomic orbitals. Solid State Communications 95 (10), 685–690.

Sarnthein, J., Schwarz, K., Blochl, P., 1996. *Ab initio* molecular-dynamics study of diffusion and defects in solid Li_3N. Physical review. B, Condensed matter 53 (14), 9084–9091.

Schirmer, B. B., Heitjans, P., Stockmann, H. J., Ackermann, H., Buttler, W., Freilander, P., Kiese, G., van der Marel, C., A, 1992. Li^+ diffusion in the fast ionic conductor Li_3N investigated by beta -radiation detected NMR. Journal of Physics: Condensed Matter 4 (20), 4779.

Schulz, H., Schwarz, K., 1978. Is there an N^{3-} ion in the crystal structure of the ionic conductor lithium nitride (Li_3N). Acta Crystallographica Section A 34 (6), 999–1005.

Schulz, H., Thiemann, K. H., 1979. Defect structure of the ionic conductor lithium nitride (Li_3N). Acta Crystallographica Section A 35 (2), 309–314.

Segall, M. D., Pickard, C. J., Shah, R., Payne, M. C., 1996a. Population analysis in plane wave electronic structure calculations. Molecular Physics 89 (2), 571–577.

Segall, M. D., Shah, R., Pickard, C. J., Payne, M. C., 1996b. Population analysis of plane-wave electronic structure calculations of bulk materials. Physical Review B 54 (23), 16317–16320.

Sholl, D., Steckel, J. A., 2009. Density Functional Theory: A Practical Introduction. Wiley-Interscience.

Simpson, L. A., Carter, R. E., 1966. Oxygen Exchange and Diffusion in Calcia-Stabilized Zirconia. J. Am. Ceram. Soc. 49, 139.

Singh, D. J., Nordstram, L., 2006. Planewaves, Pseudopotentials, and the LAPW Method. Springer US.

Slater, J. C., 1951. A simplification of the hartree-fock method. Physical Review 81, 385–390.

Smith, D. L., Baker, C. C., Sze, D. K., Morgan, G. D., Abdou, M. A., Piet, S. J., Schultz, K. R., Moir, R. W., Gordon, J. D., 1985. Overview of the Blanket Comparison and Selection Study. Fusion Science and Technology 8, 10–44.

Steele, B. C. H., 1992. Oxygen ion conductors and their technological applications. Materials Science and Engineering: B 13 (2), 79–87.

Tanifuji, T., Shiozawa, K., Nasu, S., 1978. Heat capacity of lithium oxide from 306 to 1073 K. Journal of Nuclear Materials 78 (2), 422–424.

Tarascon, J. M., Armand, M., 2001. Issues and challenges facing rechargeable lithium batteries. Nature 414 (6861), 359–67.

Taylor, P., Walker, J. R., Catlow, C. R. A., 1981. Defect structure and ionic conductivity in lithium nitride. Philisophical Magazine A 43 (2), 265.

Telfert, G. B., Wilde, P. J., Jackson, R. A., Meenan, P., Roberts, K. J., 1996. Potential fitting to molecular ionic materials. Philosophical Magazine Part B 73 (1), 147–152.

Tolman, R. C., 1938. The Principles of Statistical Mechanics. Oxford University Press, London.

Trygubenko, S. A., Wales, D. J., 2004. A doubly nudged elastic band method for finding transition states. The Journal of Chemical Physics 120 (5), 2082–2094.

Tsuchida, E., 2011. *Ab initio* mass tensor molecular dynamics. The Journal of Chemical Physics 134 (4), 44112.

Tubandt, C., Lorenz, E., 1914. Molekularzustand und elektrisches Leitvermögen kristallisierter Salze. Zeitschrift für Physikalische Chemie B 87, 513–543.

Vanderbilt, D., 1990. Soft self-consistent pseudopotentials in a generalized eigenvalue formalism. Physical Review B 41 (11), 7892–7895.

VandeVondele, J., Hutter, J., 2007. Gaussian basis sets for accurate calculations on molecular systems in gas and condensed phases. The Journal of Chemical Physics 127 (11), 114105.

VandeVondele, J., Krack, M., Mohamed, F., Parrinello, M., Chassaing, T., Hutter, J., 2005. Quickstep: Fast and accurate density functional calculations using a mixed Gaussian and plane waves approach. Computer Physics Communications 167 (2), 103–128.

Verlet, L., 1967. Computer "Experiments" on Classical Fluids. I. Thermodynamical Properties of Lennard-Jones Molecules. Physical Review 159 (1), 98–103.

Verlet, L., 1968. Computer "Experiments" on Classical Fluids. II. Equilibrium Correlation Functions. Physical Review 165 (1), 201–214.

Voter, A. F., 1997. Hyperdynamics: Accelerated Molecular Dynamics of Infrequent Events. Physical Review Letters 78 (20), 3908–3911.

Wachsman, E. D., Lee, K. T., 2011. Lowering the temperature of solid oxide fuel cells. Science (New York, N.Y.) 334 (6058), 935–9.

Wagner, C., Schottky, W., 1930. Theory of controlled mixed phases. Zeitschrift für Physikalische Chemie B 11, 163.

Wahl, J., 1979. Ionic conductivity of lithium nitride doped with hydrogen. Solid State Communications 29 (6), 485–490.

Wang, Z., Gobet, M., Sarou-Kanian, V., Massiot, D., Bessada, C., Deschamps, M., 2012. Lithium diffusion in lithium nitride by pulsed-field gradient NMR. Physical Chemistry Chemical Physics 14 (39), 13535–13538.

Wilkening, M., Heitjans, P., 2012. From Micro to Macro: Access to Long-Range Li^+ Diffusion Parameters in Solids via Microscopic $^{6,7}Li$ Spin-Alignment Echo NMR Spectroscopy. ChemPhysChem 13 (1), 53–65.

Wolf, M. L., Catlow, C. R. A., 1984. A molecular dynamics simulation study of the superionic conductor lithium nitride. II. Journal of Physics C: Solid State Physics 17 (36), 6635.

Wolf, M. L., Walker, J. R., Catlow, C. R. A., 1984. A molecular dynamics simulation study of the superionic conductor lithium nitride. I. Journal of Physics C: Solid State Physics 17 (36), 6623.

Wright, P. V., 2002. Developments in Polymer Electrolytes for Lithium Batteries. MRS Bulletin 27 (08), 597–602.

Wu, S., Dong, Z., Boey, F., Wu, P., 2009. Electronic structure and vacancy formation of Li_3N. Applied Physics Letters 94 (17), 172104.

Yu Yao, Y. F., Kummer, J. T., 1967. Ion exchange properties of and rates of ionic diffusion in beta-alumina. Journal of Inorganic and Nuclear Chemistry 29 (9), 2453–2475.

Yugami, H., Ishigame, M., 1993. Fundamental Physics and Promising Applications of Superionic Conductors. Japanese Journal of Applied Physics 32 (2R), 853.

Zintl, E., Brauer, G., 1935. Zeitschrift für Elektrochemie und angewandte physikalische Chemie 41, 102.

Appendix I

Attached in the back cover is a CD that contains the movies of diffusion referred to in this thesis. The movies of diffusion events have been extracted from NEMD simulations performed on Li_2O and Li_3N, as described in Chapters 3 and 4, respectively. The captions for these movies are listed below.

Movie 3.1 The 490 ps trace of one Li^+ cation (green) diffusing through the oxide sublattice (red) of Li_2O at 973 K. Here and in Movie 3.2 the lower part of the movie shows a projection down [010], the upper part is projected down [100] and each black point on the trace represents a time window of 200 fs.

Movie 3.2 The 490 ps trace of one Li^+ cation (green) diffusing through the oxide sublattice (red) of Li_2O at 1373 K.

Movie 3.3 A 2 ps section of Movie 3.1 showing the concerted nearest-neighbour mechanism in Li_2O. Here and in Movie 3.4 the green sphere is the Li^+ cation seen in Movie 3.1, blue spheres represent neighbouring Li^+ cations and each black point on the trace represents 2 fs.

Movie 3.4 A 1.6 ps section of Movie 3.1 showing the octahedral-interstitial mechanism operating in Li_2O in the low-temperature regime.

Movie 3.5 A 5 ps section of Movie 3.2 showing the octahedral-interstitial mechanism operating in the high-temperature regime of Li_2O. The movie also includes a $\langle 110 \rangle$ hop by a Li^+cation. The purple traces represent Li^+ cations that do not hop during the movie, but are shown for completeness. Each point on the traces represent 2 fs.

Movie 4.1 2.5 ps of a vertical dumbbell mechanism about a Li(2) site in Li_3N viewed along [010]. The green and blue spheres represent the two Li^+cations that form the dumbbell. The blue and green points are their traces with each point representing 1 fs. The red spheres represent the N^{3-} anions.

Movie 4.2 7 ps of a horizontal dumbbell mechanism about a Li(1) site in Li_3N. Traces showing the diffusion of Li^+ cations. The green and blue spheres are Li^+ cations. The red spheres represent the N^{3-} anions. Each point in the trace represents a time window of 1 fs.

Movie 4.3 The same diffusion event shown in Movie 4.2, but viewed along [001], a top-down view.

Movie 4.4 2 ps of an interlayer diffusion mechanism in Li_3N via a Li(1) site at 600 K. The red and blue spheres represent nitrogen and lithium atoms, respectively. The green sphere is the diffusing lithium atom. The coloured points represent a 1 fs time window.

Movie 4.5 2.5 ps of an interlayer diffusion through a Li(1) - Li(1) edge in Li_3N at 600 K. The red and blue spheres represent nitrogen and lithium atoms respectively. The green sphere is the diffusing lithium atom. The coloured points represent a 1 fs time window.

Movie 4.6 The diffusion trace of a single Li^+ cation (green) through the nitride sublattice (red) of Li_3N over a period of 100 ps viewed (a) along [001] and (b) along [010]. Each black point represents 100 fs of the Li^+ cation trajectory.

Movie 4.7 The diffusion trace of a single Li^+ cation (green) through a nitride sublattice (red) of Li_3N over a period of 100 ps viewed along [010]. Each black point represents 100 fs of the Li^+ cation trajectory.